

OPTICAL AND INFRARED STUDIES

OF

COMETARY DUST

Being a thesis submitted to the University
of Leicester by,

C.M.Birkett

in candidature for the degree of

DOCTOR OF PHILOSOPHY 1987.

Department of Astronomy
University of Leicester.

UMI Number: U004226

All rights reserved

INFORMATION TO ALL USERS

The quality of this reproduction is dependent upon the quality of the copy submitted.

In the unlikely event that the author did not send a complete manuscript and there are missing pages, these will be noted. Also, if material had to be removed, a note will indicate the deletion.



UMI U004226

Published by ProQuest LLC 2015. Copyright in the Dissertation held by the Author.
Microform Edition © ProQuest LLC.

All rights reserved. This work is protected against
unauthorized copying under Title 17, United States Code.



ProQuest LLC
789 East Eisenhower Parkway
P.O. Box 1346
Ann Arbor, MI 48106-1346



DECLARATION

This work has been carried out under the supervision of Professor A.J.Meadows. I certify that the work has not been accepted in substance for any degree, and is not being concurrently submitted in candidature for any degree.

Acknowledgements

I am grateful to Professor A.J.Meadows for accepting me as a postgraduate student and for providing helpful advice and guidance throughout the past three years. I also wish to thank the members of the Astronomy Department especially Alan Fitzsimmons and Dr. Dave Adams for many arm-waving discussions and Dr. Philippa Berry and John Brooker for being my personal program advisory service.

I am indebted to Dr. Nick Eaton for the use of his computer programs and to Dr. Simon Green for many theoretical discussions.

Appreciation is due to Mr. Ken Russell for his work at the UK Schmidt Telescope, to Dr. Harvey MacGillivray and the COSMOS team for digitising all the Schmidt plates and to the Starlink software crew for much advice during my visits to the Royal Observatory Edinburgh.

Finally, special thanks go to Comet Halley, for having returned to the Solar System at such a perfect time.

Some of the data and analysis in this thesis has appeared in five papers:

1. Observations of Comet Crommelin - I. Morphology and C_2 production rate.

K.S.Russell, J.A.Dawe, C.M.Birkett, D.J.Adams and A.J. Meadows, Mon. Not. R. Astr. Soc (1985), 217, p651.

2. Infrared and Optical Observations of Low Activity Comets, P/Arend-Rigaux (1984k) and P/Neujmin 1 (1984c).

C.M.Birkett, S.F.Green, J.C.Zarnecki and K.S.Russell, Mon. Not. R. astr. Soc (1987), 225, p285.

3. UK Schmidt Analysis of Comet Halley.

C.M.Birkett, A.Fitzsimmons and K.S.Russell, In "The Exploration of Comet Halley" Proc. 20th ESLAB Symposium, Heidelberg (1986), ESA SP-250, 57.

4. CCD and UK Schmidt Observations of P/Giacobini-Zinner.

A. Fitzsimmons and C.M.Birkett, (In prep.).

5. UK Schmidt Analysis of Comet Halley. The Application of Finson-Probst Theory to Large-Scale Images.

C.M.Birkett (In prep.).

Contents

	Pg.
1. Introduction	1.1
1.1 Cometary Orbits and Origins	1.2
1.2 Chemical Composition, Physical Structure and Emission Processes	1.7
1.3 Interrelations	1.12
1.4 The Importance of Cometary Research	1.15
1.5 The Main Aims of this Thesis	1.17
2. Large Scale Dust Structure	2.2
2.1 Finson-Probstein Theory	2.3
2.2 Comet Halley - Past and Present	2.21
2.3 Application of Finson-Probstein Theory to the Dust Tail of Comet Halley	2.24
2.4 Conclusion	2.46
3. Dust Features in the Inner and Outer Coma	3.1
3.1 The UK Schmidt telescope and the COSMOS Measuring Machine	3.2
3.2 Description of CCD and UK Schmidt plates of Comets Crommelin, Giacobini-Zinner and Halley	3.5
3.3 Intensity Contours- Their shape and symmetry	3.9
3.4 Near Nuclear Features-Examination of the Fountain Model.	3.14
3.5 Application of Finson-Probstein Theory	3.18
3.6 Dust Distribution and Intensity Profiles and the Existence of Icy Dust Grains.	3.21
	3.26

	Pg.
4. Thermal Spectra- Mie Theory and Dust Temperatures	4.1
4.1 Properties of Dust Grains	4.2
4.2 Mie Theory	4.6
4.3 Application of Mie theory to Thermal Spectra	4.9
4.4 Application of Mie theory to Comet Halley	4.14
4.5. Conclusion	4.22.
5. Detectability of Faint Cometary Activity	5.1
5.1 Comet Halley - Early Preperihelion Images	5.2
5.2 Decaying Comets: Optical and Infrared Observations	5.5
5.3 Conclusion	5.21
6. Conclusions and Suggestions for Further Work	6.2
Appendices	
A.I Properties of Orbits	6.7
A.II Dust Particle Orbits	6.13
A.III Mass Loss Rates and Dust Albedos	6.18
References	6.20

CHAPTER 1

INTRODUCTION

Comets have always fascinated mankind. For many centuries they have been regarded as omens of war, famine and impending doom. Today they are of prime importance in solar system research. Their chemical and physical nature can not only be related to other solar system phenomena but may also hold clues to the early formation of the solar system.

The following chapter gives a review of modern cometary science. The physical, chemical and orbital properties of comets are discussed together with a brief look at the origins of comets.

Interrelations with solar system objects such as asteroids, meteors and the Zodiacal light are looked into particularly with regards to the "ageing comet". Finally, the main aims of this thesis are outlined.

1.1 Cometary Orbits and Origins

In the absence of non-gravitational effects and planetary perturbations, a cometary nucleus will orbit the sun on a path that is a conic section with the sun at one focus. The parameter that determines whether the path is an ellipse, a parabola, or a hyperbola is the total energy E , of the nucleus. The total energy, which is the sum of kinetic and gravitational potential energies, is given by,

$$E = v^2/2 - GM/r$$

where v is the velocity, r is the heliocentric distance, M is the mass of the sun, G is the gravitational constant and E is the total energy per unit mass. The orbital elements of a comet include its eccentricity e , orbital period P , semi-major axis a and inclination i of its orbital plane to the plane of the ecliptic. Fig.1 shows the distribution between inclination and eccentricity for various solar system bodies.

Each year 10-20 comets are discovered or recovered, and to date about 1000 comets are known. They can be divided into two groups, long period comets with, $P > 200$ years and short period comets $P < 200$ years. The majority of comets with known orbital elements have long periods and these can range from several hundred to a few thousand years. Long period comets, if they come into close proximity with the Earth, are the most spectacular. Their orbits have random inclinations and can be prograde or retrograde. A subset of these are known as the Sungrazing comets, as their perihelion distances are so small that they graze the outer atmosphere of the Sun. Short period comets tend to be less bright and fuzzy in appearance. Their orbital inclinations are restricted approximately to $i < 40^\circ$

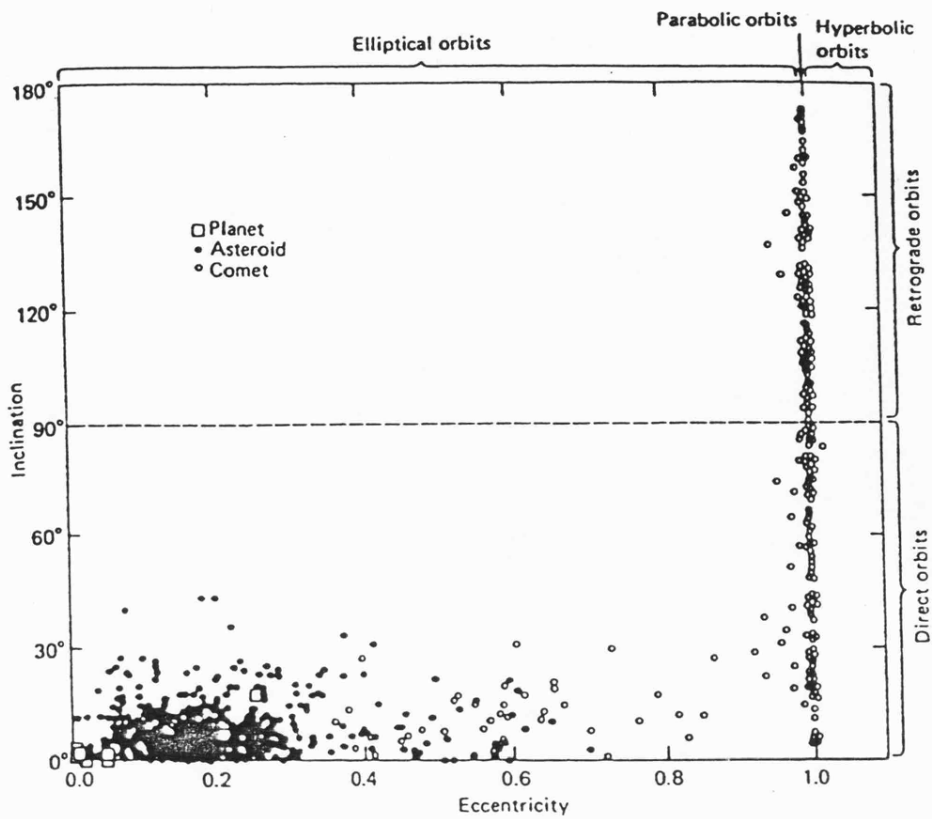


Fig.1. *Orbital eccentricities and inclinations of the planets, asteroids and comets. The belt asteroids appear as a dense cluster to the left and the near-parabolic comets as a column to the right. The space between contains Apollo and Amor asteroids, and periodic comets which have similar orbits. Taken from Wood, 1979.*

and their motions are mostly prograde. Both long and short period comets can have very eccentric orbits.

Where do comets come from? The idea of a large reservoir of comets surrounding the solar system was put forward by Peirce in the nineteenth century, by Opik in 1932 and by van Woerkom in 1948. In the 1950's Oort developed and modified this idea and his final theory has become widely accepted (Oort, 1950).

Oort considered the original values of $1/a$ (taken from the work of E. Stromgren) when the comets were outside the orbits of the major planets. He concluded that the majority of these comets originated in a region of space extending from 20,000 AU to 150,000 AU. This is almost half the distance to the nearest star. However most of the cometary orbits were near-parabolic i.e. their velocity at the remote distance was equal to zero, implying that they were in fact bound to the Sun. Oort estimated that this reservoir of comets (later termed the "Oort Cloud") contained roughly 10^{11} comets with a combined mass between $1/10$ and $1/100$ the mass of the Earth.

Oort further speculated that a fraction of these Oort Cloud comets could be perturbed into the solar system by passing stars and thus form the long period comets. The short period comets could then be accounted for by further perturbations by the major planets especially Jupiter. He also suggested that comets were formed at an early stage of the formation of our planetary system, in the vicinity of the asteroid belt and then perturbed into the large stable Oort cloud orbits by the perturbing actions of Jupiter. It has since been suggested that comets originally accreted in the outer regions of the solar system where ices are stable and

silicate dust was available.

Everhart (1972) has approached the subject of perturbations by Jupiter by calculating the orbits of comets for thousands of passages into the solar system. He found that Jupiter could be responsible for the orbital properties of the short period comets providing the original long period comets had perihelia near to Jupiter and small orbital inclinations.

There have been other "origin of comets theories" put forward. For example the Flying Sandbank model (Lyttleton, 1953) suggests that the Sun passes through a cloud of dust and gas every 225×10^6 years. In doing so, small compact clouds containing many comets become perturbed into the solar system. From early speculation by Ovenden (1975), van Flandern (1978) suggested that an exploding planet created both the asteroids and the comets. One theory (Vsekhsvyatskij, 1977) even suggests that the Jovian planets/satellites spewed volcanic material into the outer solar system.

If comets were interstellar wanderers, the idea that the Sun could sweep them up in its travels around the centre of the galaxy has to be rejected. On capture the comets would have hyperbolic orbits with finite velocities, $v > 0$ and they would appear to come from the general direction of Hercules (the point to which our solar system is moving). Both facts disagree with known observations, comets come from all directions and have near-parabolic orbits ($v=0$) i.e. they are at great distances but attached to the solar system. One problem does remain however. How is the Oort Cloud replenished? Comets are lost to the planetary system and therefore the source must be replenished by perturbations from passing stars or by the movement of the Sun through regions of

molecular clouds. The Sun lies on the edge of the Orion star spiral, but a few million years ago the Sun passed through a region of molecular clouds and new stars, called Gould's belt. Bailey et al., (1985) concluded that molecular clouds were indeed an effective way of replenishment. Due to the distribution of these clouds (concentrated in the spiral arms and the galactic centre), the replenishment is episodic rather than continuous.

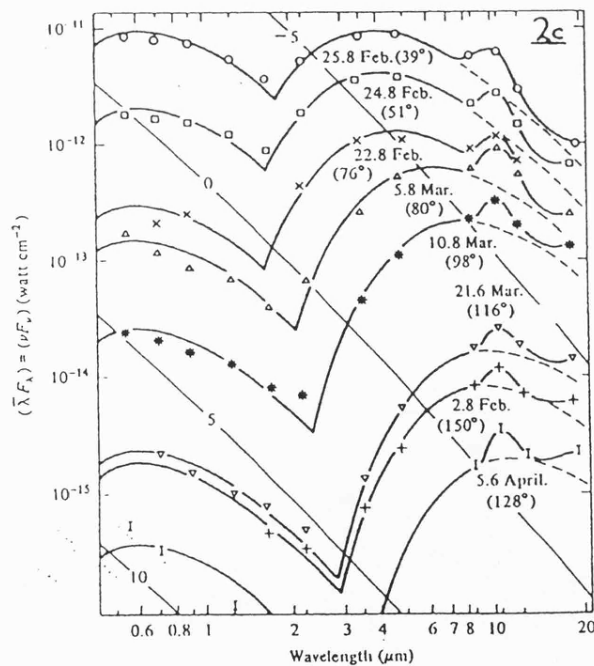
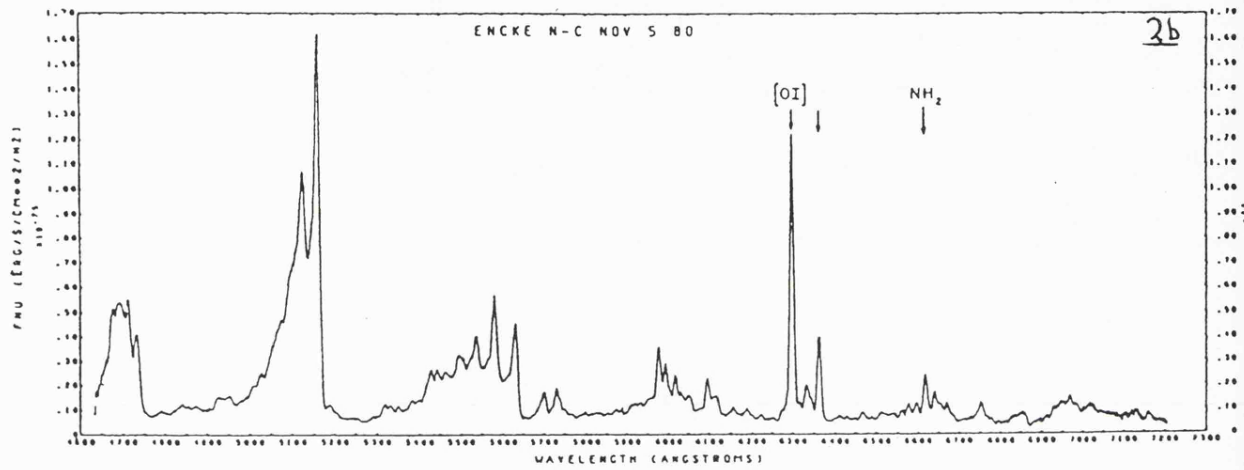
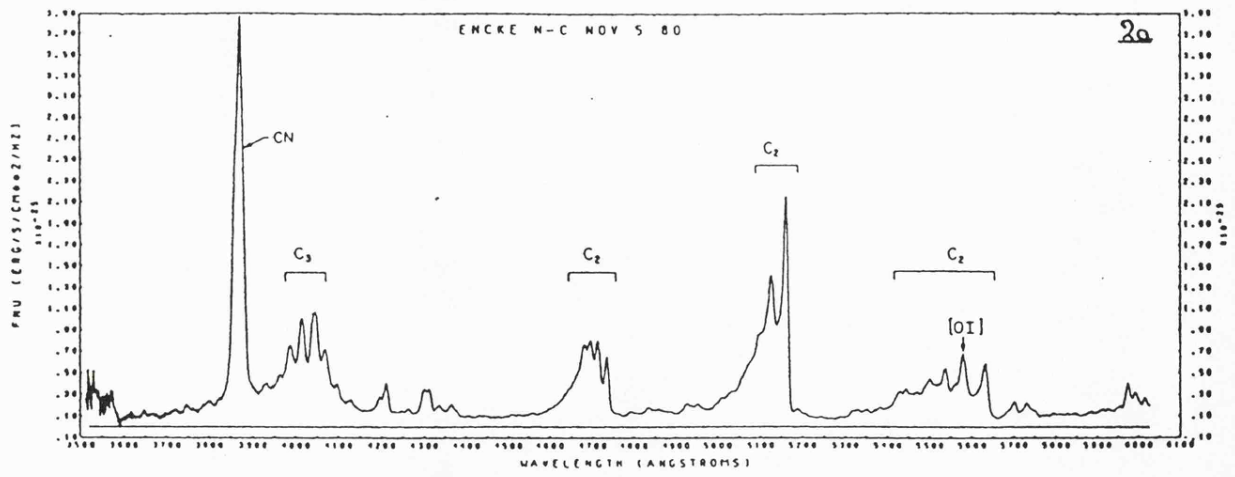


Fig.2a+b. Spectrum of P/Encke obtained by H.Spinrad with scattered solar spectrum removed (Wyckoff, 1982).

Fig.2c. Energy distribution of P/West obtained by E.P.Ney and K.M.Merrill. The silicate feature can be seen at 10 μ m (Brandt & Chapman, 1982).

1.2 Chemical Composition and Physical Structure

What is a comet? A comet can be thought of as being composed of five main structures, nucleus, coma, dust tail, gas tail and a hydrogen-hydroxyl cloud. A cometary nucleus is thought to be an aggregate of water ice and dust (originally suggested by Whipple, 1950). From ultraviolet observations the ice is believed to be predominantly water ice, with frozen carbon monoxide, carbon dioxide and other clathrates as minor constituents (Delsemme and Swings, 1952). Evidence for the domination of water ice comes from the observations of the huge hydrogen clouds surrounding comets and also the presence of OH and H₂O⁺. Pure water ice, ^{of high albedo, is} not expected to sublime for heliocentric distances greater than 3AU. However some comets have shown activity up to distances of ~6AU, suggesting the presence of minor constituents trapped in the matrix of the clathrate snows and which are more volatile than water. For example, Comet Humason (1961e) showed activity and the presence of CO⁺ in its spectrum at a distance of r=5AU (Brandt & Chapman, 1982). The dust is thought to be silicate material, similar to the composition of carbonaceous chondrites (meteorites). As the nucleus approaches the Sun, its temperature increases and the ices begin to evaporate. This has two effects, firstly it releases the dust embedded in the ice and secondly it produces a quantity of gas. For the dust grains, solar radiation pressure reduces the apparent gravitational attraction of the Sun and so are forced back into forming a dust tail. Gaseous molecules are photodissociated into their daughter molecules/atoms, which in turn may be ionised by the solar ultraviolet radiation. The cometary gas forms the "coma". The interplanetary magnetic field associated

with the solar wind (a stream of electrons and protons) wraps itself around the head of the comet and pulls the cometary ions back into a plasma tail. Not all comets display two distinguishable tails. The brightness and extent of the comet depends on the size of the nucleus and its proximity to the Sun and the Earth.

Comets can be observed in the ultraviolet, optical, near and far infrared, and radio wave parts of the electromagnetic spectrum. A typical spectrum is shown in Fig.2. As can be seen a cometary spectrum can be divided roughly into two: 1) A reflected solar spectrum, formed by the scattering of solar radiation by the dust particles in the dust tail and the coma. Superimposed on this are the emission spectra from the various gaseous species. 2) A thermal spectrum, formed by the absorption and subsequent emission of solar radiation by the dust grains. Superimposed on this we can have water ice absorption features (at $\approx 2\mu\text{m}$), silicate emission features (at ≈ 10 and $20\mu\text{m}$) and perhaps hydrocarbon absorption features due to other cometary ices.

Parent species released directly from the subliming ice tend to have short lifetimes against photodissociation. Their resonance transitions are also outside the ultraviolet and optical windows (0.12 to $1\mu\text{m}$). It is only their daughter products which can therefore be observed directly via optical spectra. Table 1 indicates the known cometary species (taken from Brandt and Chapman, 1982).

Table 1

Atoms, ions, molecules and molecular ions
observed in comets

H, OH, H ₂ O, O, S	CO ⁺ , CO ₂ ⁺ , H ₂ O ⁺ , OH ⁺
C, C ₂ , C ₃ , CH, CN, CO, CS	CH ⁺ , N ₂ ⁺ , Ca ⁺ , C ⁺ , CN ⁺
HCN, CH ₃ CN, NH	
NH ₂ , Na, Fe, K	
Ca, V, Cr, Mn, Co, Ni, Cu	

The plasma tail is dominated by the emission spectra of CO⁺ and H₂O⁺, while the coma is dominated by H, C, N, O and S (i.e. cosmically abundant elements). Metals have also been detected but usually only in sungrazing comets when radiation temperatures $T > 1000\text{K}$ can vaporize the refractory components of dust. One exception to this rule is the presence of Na⁺ in Comet Halley. It was detected by a gas spectrometer experiment on-board the Giotto spacecraft (Krankowsky et al., 1986) during March 1986. The mean dust temperature of Halley followed the relationship $T = 329r^{-0.53}$ giving a dust temperature of $\approx 350\text{K}$, well below that expected to produce such metal ions. Have previous spectra been insensitive to such metal detections?

The three most abundant substances are H, OH and O, although compared with cosmic abundances the amount of H and C in comets is depleted. The total amount of carbon could, however, be raised if the chemical composition of the dust grains is taken into consideration.

1.3 Interrelations

In the past, astronomers have been eager to classify solar system objects into discrete categories e.g. planets, satellites, comets, asteroids, meteors etc. Over the past decade these clearcut divisions have diminished.

How do we differentiate between a comet and an asteroid? Marsden (1970, 1971, 1972) has considered this problem with respect to their orbital properties. The Main Belt of asteroids lies between Mars and Jupiter and their orbits have eccentricities $e < 0.4$. Short period comets have random, eccentric ($0.3 < e < 0.8$) orbits and approach Jupiter to within 0.9AU. However several asteroids e.g. 944 Hidalgo and 2060 Chiron are known to have irregular orbits which bring them closer to Jupiter (to within 1.1AU) than any of the Main Belt asteroids.

It appears that most of the cometary nuclear surfaces are covered with dust (Sekanina, 1981) of similar composition to the dust which coats asteroidal surfaces. The distinction is made, however, between an asteroid which is a rocky mass and a comet which undergoes gaseous activity. A comet having negligible non-gravitational effects (i.e. forces due to the action of a jet caused by sublimation of surface volatiles) may be considered to be inactive. Marsden noticed P/Neujmin and P/Arend-Rigaux avoided close approaches with Jupiter, displayed very low activity and had no detectable non-gravitational forces.

Repeated returns of a comet to the inner solar system ensure that a cometary nucleus loses a certain fraction of its mass each time. Eventually all the ice will sublimate, possibly leaving a small non-volatile core. Such non-volatile

cores could exist if the cometary nucleus formed close to the Sun or was subjected to radiogenic heating (from short lived radionuclides e.g. ^{26}Al) (Wilkening, 1979). The Earth approaching asteroids (Apollo, Amor, Aten objects) have different orbits and are also smaller ($R < 6\text{km}$) in size than the Main Belt asteroids (Shoemaker et al., 1979). However their radii are comparable with the recent measurements of Halley's elongated nucleus ($7 \times 4\text{km}$) by the Vega and Giotto probes (Sagdeev et al., 1986, Keller et al., 1986). These Earth approaching asteroids are in orbits of short dynamical lifetimes ($< 3 \times 10^7$ years) and hence require a replenishing source. The idea of main belt asteroids being such a source is not yet confirmed. The known mechanisms were not believed to be efficient enough to produce the required numbers. However recent work by Wisdom (1985) shows that there is a strong perturbation effect for motion near the 3/1 commensurability with Jupiter. Calculations of the long term trajectories show that asteroids which originally approach this zone, are later seen to cross planetary orbits. Do comets therefore evolve into Earth approaching asteroids? (Shoemaker et al. 1979, Wasson and Wetherill, 1979).

A comet may not eventually decay to one small rocky core. Instead a mass of dust grains may remain which spread out along the comet's orbit via perturbations, to form meteor streams. Meteor streams may also form from the dust emitted by the gradual decay of the nucleus. Some well known examples include the Orionid and η Aquarid streams associated with comet Halley, and the Draconids associated with comet Giacobini-Zinner. The study of meteors is therefore the study of the solid material in the cometary nucleus. Both meteor and cometary grains have similar chemical properties. There is no firm evidence however to indicate that a large piece of a

cometary meteoroid has ever reached the Earth's surface. Material found on the Earth's surface - meteorites, are usually associated with asteroids.

Comets are also regarded as a possible source of dust grains for the Zodiacal light (Whipple, 1955). This light is seen after sunset and is associated with scattering of sunlight by dust grains which are located in the plane of the ecliptic. The dust grains emitted by comets are distributed throughout the solar system via planetary perturbations and the Poynting-Robertson effect (due to the action of relative velocities, the dust grains are decelerated and eventually spiral into the Sun). The Zodiacal Cloud is itself destroyed by the Poynting-Robertson effect, plus the effects of erosion, sublimation and collision (Burns et al., 1979). It therefore needs a source of influx to maintain a steady-state condition. Theoretical studies indicate that short period comets cannot supply the required material unless in the form of large boulders which can easily escape detection.

Extraterrestrial particles have been collected in the upper atmosphere (20km) by aircraft. Most of these particles have elementary abundances that closely match those of carbonaceous chondrite materials i.e. they have unequilibrated collections of minerals and high porosities. This suggests a cometary origin, if one considers that a porous material may have been originally filled with ice. However a small proportion of these extraterrestrial particles are compact layer lattice silicates suggesting an origin in a small, compact, parent body, such as an asteroid (Sandford, 1986).

1.4 The Importance of Cometary Research

If we assume that comets were formed at the outer edge of the original solar nebula (at the same time as the Sun and the planets) then we can say that due to their small masses and long orbital periods they have been less affected by internal and external evolution than other members of the solar system. They therefore provide information on the nature, composition and formation of the ancient solar nebula.

Up to March 1986 a cometary nucleus had never been definitely observed. To have observed a single mass at the centre of the comet would have supported Whipple's "dirty snowball" model and disproved the belief that the centre of the comet contained a swarm of large icy grains. Previous attempts to observe a nucleus had involved observing the comet at very large heliocentric distances, when cometary activity was at a minimum. However, the nucleus had never been unambiguously resolved.

The previous section has already discussed the importance of determining the links between comets and other solar system phenomena. The solar wind is responsible for the development of the plasma tail, but plasma tail observations over a time span can serve as a means of studying the variability of the solar wind.

The return of P/Comet Halley in 1986 created excitement for the astronomers and public alike. It was known that Comet Halley was one of the largest and most active of all the periodic comets and had been an inspiring visitor over many centuries. An "International Halley Watch" (or IHW) team was created to co-ordinate and archive Halley observations from observers all around the world.

Similar committees were set up elsewhere. The IHW consisted of many sections, each devoted to a particular method of observing, such as spectroscopy or photometry. Other sections devoted their time to observing, particularly cometary structures. The ground-based observations also served as back-up information for the five successful spacecraft missions to Comet Halley.

As comets had never been so intensely studied before with modern day techniques, two trial runs were performed on lesser known comets, Comets Crommelin and Giacobini-Zinner. As part of the IHW campaign, the Leicester team became involved with infrared and optical observations of all three comets using a variety of instruments. Some of these observations are discussed in this thesis.

1.5 The Main Aims of the Thesis

This thesis attempts to obtain a better understanding of the structure of a cometary dust tail and the nature of the cometary dust grains. The main aims of this thesis are therefore,

- a) To apply Finson and Probst's dust tail analysis to several comets, Comets Crommelin, Arend-Rigaux, Giacobini-Zinner and in particular to Comet Halley.
- b) To determine dust grain size distributions, ejection velocities and emission times from the cometary nucleus.
- c) Knowing the rotation period of Comet Halley, to determine whether the "multiple dust tails" seen after perihelion can reveal information concerning the activity of the nucleus.
- d) To apply Mie scattering theory to far infrared data and determine dust composition, temperature and size distribution.
- e) To consider the appearance of cometary "nuclei" at great distances from the Sun and when the nuclei are considered inactive.

CHAPTER 2

LARGE SCALE DUST STRUCTURE

2.1 Finson and Probststein Theory

In 1968 Finson and Probststein published a paper outlining a theory which calculated the orbits of dust grains which made up a type II or dust tail. Their theory was based on previous work by Bessel (1830) and Bredichin (1900), who tried mathematically to explain the various forms and structures associated with dust tails of various comets.

Assumptions

1. The cometary nucleus is heated symmetrically, with equal gas and dust temperatures.
2. The dust grains are accelerated radially outward from the nucleus by drag forces due to the expanding gas in the comet head. The gas expansion is spherically symmetric.
3. Near the nucleus the gas density (n_g) is high and there are a large number of molecular collisions. At $\approx 10^4$ km there is a transition zone, beyond which the gas density decreases and the flow becomes free molecular.
4. At a certain distance from the nucleus (20-100km) the dust-gas interaction diminishes and the dust grains reach a terminal velocity.
5. As the above distance is small one can assume that, essentially, the grains are leaving the nucleus in a continuous spherically symmetric manner, with velocity $\approx 1\text{kms}^{-1}$.
6. The only significant forces to act on the particles are solar gravity and the force due to solar radiation pressure. Gravitational forces exerted by planets and the cometary nucleus are ignored.
7. There is a wide size distribution of grains.
8. The motion of these particles in a tail is hypersonic and

collision free.

9. The theory applies to comets which exhibit type II tails only, i.e. no interaction between plasma and dust tails is taken into consideration.

Considering assumption 6, the force of radiation pressure is directed radially outward and varies as r^{-2} (r =heliocentric distance). The force due to solar gravity follows the same fall-off law, hence the net force or "effective gravitational field" is defined by $F_{\text{grav}} - F_{\text{rad}}$.

The strength of the radiation pressure is usually denoted by,

$$1-\mu = \frac{F_{\text{rad}}}{F_{\text{grav}}} = \beta$$

and

$$F_{\text{rad}} = \left(\frac{Q_{\text{pr}}}{c} \right) \left(\frac{E_{\text{s}}}{4\pi r^2} \right) \left(\frac{\pi d^2}{4} \right) \quad F_{\text{grav}} = \left(\frac{GM_{\odot}(\rho)}{r^2} \right) \left(\frac{\pi d^3}{6} \right)$$

where $\pi d^2/4$ = X-sectional area of the particle, assumed spherical

E_{s} = mean total solar radiation (3.93×10^{26} W)

c = speed of light

G = Universal gravitational constant

M_{\odot} = solar mass

ρ_d = mass density

Q_{pr} is the scattering efficiency for radiation pressure and depends upon the nature of the scattering medium. For a dielectric medium (e.g. silicate) $1/4 < Q_{\text{pr}} < 1/2$ and for an absorbing medium (e.g. magnetite) $1 < Q_{\text{pr}} < 2$. Fig 3a shows how Q_{pr} varies with grain radius, and Fig.3b shows how β ($=1-\mu$) varies with radius (taken from Hanner, 1980).

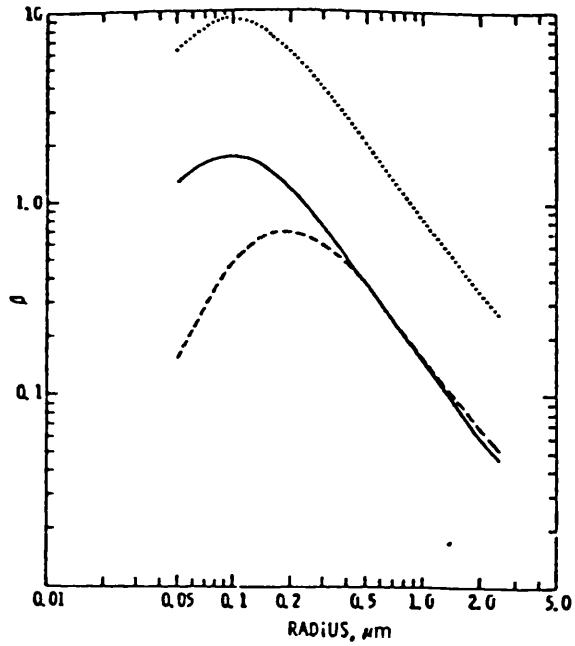
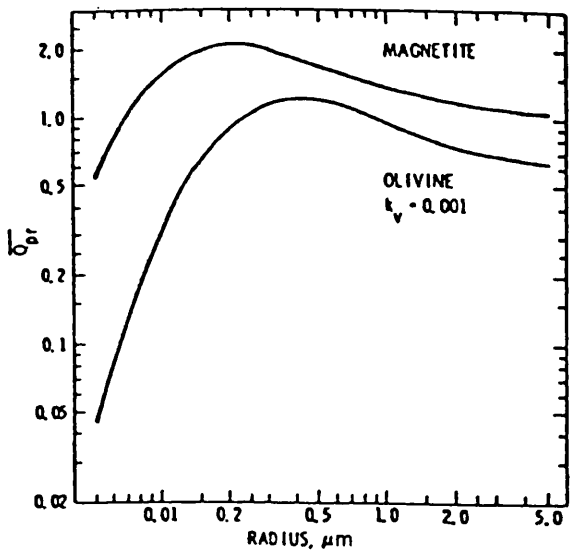


Fig.3a $\langle Q_{pr} \rangle = \int Q_{pr} S_{\lambda} d\lambda / S_{\lambda} d\lambda$ versus particle radius.

Fig.3b $\beta = F_{rad}/F_{grav}$ versus particle radius.

———— magnetite - - - - - olivine
 magnetite for which $\rho = 1 \text{ g cm}^{-3}$

In general $1 - \mu = C(\rho d)^{-1}$ indicates that the net force $\propto (1 - \mu)$ is greater for smaller particles. However larger particles which are porous or fluffy can still have large surface areas ($\propto F_{rad}$) but small masses ($\propto F_{grav}$) and therefore suffer the same net force.

From $1 - \mu$, the effective force is independent of "r" for a given distance. The force on a particle may be repulsive, attractive or equal to zero.

i.e. $1 - \mu = 0 \quad 1 \quad \infty$

$$\mu = 1 \quad \underbrace{\quad 0 \quad}_{\text{attraction}} \quad \underbrace{\quad \infty \quad}_{\text{repulsion}}$$

↓
net force = 0

Using Keplerian orbit mechanics (see Appendix I for full description of orbital types) the motions of the dust particles can be computed.

Motion of the dust particles according to Finson and Probst

For a constant grain density particles of the same size (i.e. same value of $1-\mu$) are subject to the same net force and are emitted at different earlier times τ along the comet orbit. Due to the repulsive nature of the radiation pressure, these orbits will generally be hyperbolic.

We define a cometocentric co-ordinate system (ξ, η, ζ) where ξ is directed radially away from the Sun, η is in the opposite direction to the orbital motion such that ξ and η are in the comet's orbital plane and ζ completes the right hand set. The locus in the (ξ, η) plane of the position of the dust grains at the time of the observation t_c is termed a "syndyne" i.e. particles emitted at different earlier times subjected to the same net force. A syndyne is therefore the locus of particles emitted with zero velocity relative to the nucleus. The time τ is zero at the nucleus ($\xi=\eta=0$) and increases with increasing distance from the nucleus along the locus. The curvature in the $+\eta$ direction results from Coriolis effects. Early observers matched tail curvatures with computed syndynes and found $1-\mu$ values in the range 0.1 to 1.0 (for $\rho_d=1\text{gcm}^{-3}$ diameters are $\approx 1\mu\text{m}$). Information on the emission velocities of the particles can be found from the tail widths (see Fig.4).

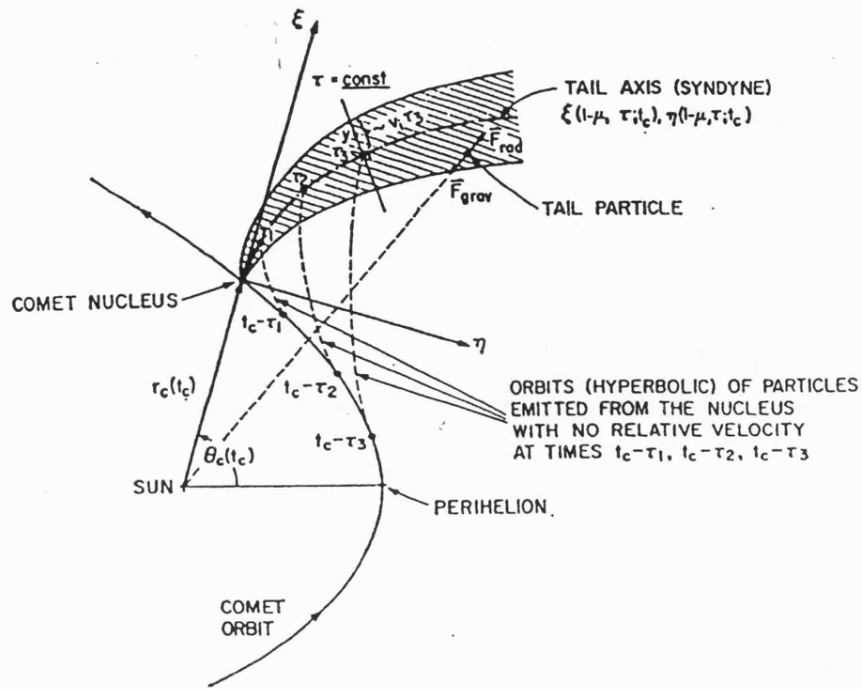


Fig.4 Comet tail and particle orbits.

(taken from Finson & Probst, 1968)

If the nucleus ejects dust particles uniformly in all directions with speed v_i , the resulting tail will be centred about the syndynes for zero relative emission velocity and the tail width at any cross-section will be $2v_i\tau$. At a given point along a syndyne τ can be determined from the orbital mechanics if $1-\mu$ is known, and thus v_i estimated. Typical values were found to be $v_i \approx 1 \text{ km s}^{-1}$.

A "synchrone" is defined to be a locus, in the (ξ, η) plane, along which all the particles have been emitted from the nucleus at the same time ($\tau = \text{constant}$) but they have a wide range of $1-\mu$ values. Along such a locus there is a range of grains suffering different $F_{\text{rad}}/F_{\text{grav}}$ forces. This means that the grains are "sorted out" according to the product (ρd) . If the density of the grains is constant, then the larger grains will remain at the end of the synchrone nearest to the nucleus, and the lightest grains will be at a further distance

from the nucleus. Finson and Probststein stated that a cometary dust tail resulted from the superposition of a large number of synchrones and syndynes.

Orbits of Dust Grains (See also Appendix 2)

The type of cometary orbit determines the orbit of the emitted dust grains. Those dust grains (with initial zero relative velocity), which are emitted from comets in parabolic orbits go into hyperbolic orbits. Dust grains emitted by comets in elliptical orbits will go into elliptical or hyperbolic orbits depending on the orbital energy and particle size. Because most observed comets have $e < 1$, only the formulae for elliptical comets will be presented here.

The total energy of a dust particle is given by E , where $E = \text{Kinetic energy} + \text{Potential energy}$, or the energy per unit mass E' is given by,

$$E' = \frac{1}{2} v_d^2 - \frac{\mu GM}{d}$$

where v_d is the instantaneous orbital speed of the particle and d is the distance from the nucleus. The term " $\mu GM/d$ " represents the reduced gravitational force.

If the particle has the same speed as the comet (i.e. 0 initial relative velocity) then at the point of release,

$$v_d^2 = \frac{GM}{d} - \frac{1}{a_c} \quad (\text{Proof App.I})$$

where a_c is the semi-major axis of the comet orbit. If release is at the perihelion position of the comet orbit then,

$$d = a_c (1 - e_c)$$

Hence
$$H_d = \frac{GM}{a_c} \frac{1 - \mu}{1 - e_c} - \frac{1}{2}$$

By definition an elliptical orbit has an energy $H_d < 0$.

i.e. $1-\mu < \frac{1-e_c}{2}$

or $1-\mu < \frac{1+e_c}{2}$ for a dust particle released
at aphelion,

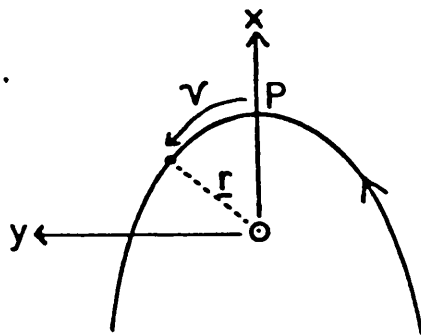
and hence intermediate values for other release points. If the above condition holds, dust grains remain in the solar system. All periodic comets have elliptical orbits and they may therefore provide the material that constitutes interplanetary dust (see chapter 2.4).

Co-ordinate Systems

These systems are based on those defined by D.R.L.Jones (1976).

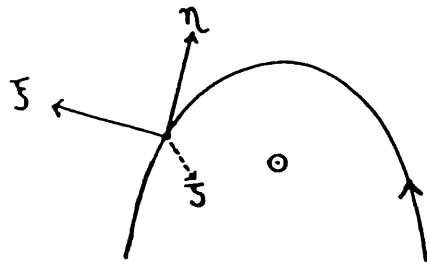
1) Orbital

(x,y,z) are a right handed set of axes in the plane of the comet, such that x points to perihelion, y to $v = 90^\circ$, and z points to the pole of the orbit.



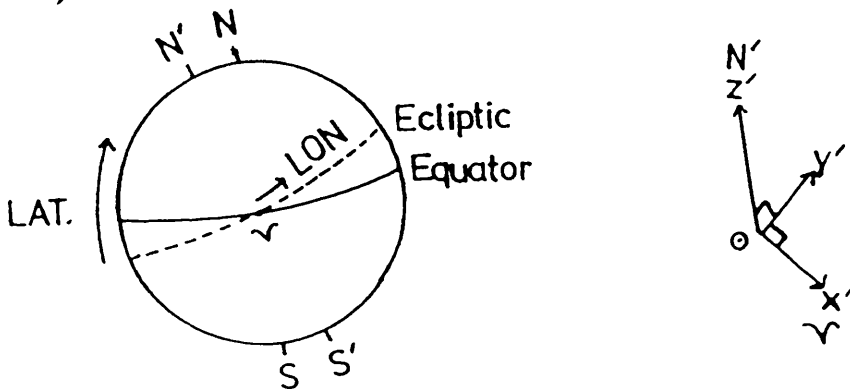
2) Cometocentric

(ξ,η,ζ) a right handed set in the plane of the comet, such that ξ points directly away from the Sun, η points in the opposite direction to the comet's motion and along its orbit, and ζ makes a right handed set in the opposite sense to z above.

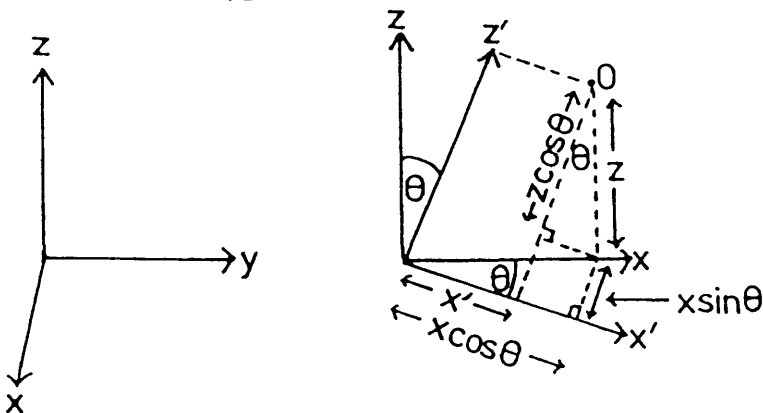


3) Heliocentric ecliptic

(x', y', z') a right handed set in the ecliptic plane where the Sun is at the origin and x' points to the vernal equinox v , y' to longitude 90° , and z' points to the pole of the ecliptic plane, N' .



To move from one co-ordinate system to another, rotation matrices are used. Consider a right handed frame of mutually perpendicular axes (x, y, z) .



This system is to be rotated clockwise about the y axis to the new frame (x', y', z') .

Consider a point $(x, 0, z)$ which becomes $(x', 0, z')$ after the rotation. The new co-ordinates are given by

$$x' = x \cos \theta - z \sin \theta$$

$$y' = y$$

$$z' = x \sin \theta + z \cos \theta$$

i.e. the rotation matrix is given by,

$$Q(\theta) = \begin{pmatrix} \cos \theta & 0 & -\sin \theta \\ 0 & 1 & 0 \\ \sin \theta & 0 & \cos \theta \end{pmatrix} \text{ rotation about the y axis}$$

As these equations are cyclic we have,

$$P(\theta) = \begin{pmatrix} 1 & 0 & 0 \\ 0 & \cos \theta & \sin \theta \\ 0 & -\sin \theta & \cos \theta \end{pmatrix} \text{ rotation about the x axis}$$

$$R(\theta) = \begin{pmatrix} \cos \theta & \sin \theta & 0 \\ -\sin \theta & \cos \theta & 0 \\ 0 & 0 & 1 \end{pmatrix} \text{ rotation about the z axis}$$

Examples

For a combination of two or more rotations, the matrix describing the net result can be found by matrix multiplication.

e.g. Orbital to ecliptic co-ordinates

The new co-ordinates are given by,

$$\begin{pmatrix} x' \\ y' \\ z' \end{pmatrix} = R(-\Omega) P(-i) R(-w) \begin{pmatrix} x \\ y \\ z \end{pmatrix}$$

e.g. Orbital to cometocentric co-ordinates

$$\begin{pmatrix} \xi \\ \eta \\ \zeta \end{pmatrix} = P(\pi) R(v) \begin{pmatrix} x \\ y \\ z \end{pmatrix} - \begin{pmatrix} r \\ 0 \\ 0 \end{pmatrix}$$

where $P(\tau) = \begin{pmatrix} 1 & 0 & 0 \\ 0 & -1 & 0 \\ 0 & 0 & -1 \end{pmatrix}$

and $\begin{pmatrix} r \\ 0 \\ 0 \end{pmatrix}$ denotes a translation corresponding to a shift of origin from the Sun.

Procedure

A dust tail is composed of many different size particles released at different times along the comet's orbit. How we view the tail from Earth depends on the projection effect - i.e. the projection of the dust tail from the comet's orbital plane to the sky plane. To analyse the structure of the tail we need to determine the position of a dust particle, relative to the comet nucleus, at a time t_c (observation time), when the particle has been previously released from the nucleus at a time τ .

A computer program, written by Dr. N. Eaton, calculates and maps syndyne orbits for a certain size distribution of grains, emitted at various times along the comet orbit. This program was updated and modified by the author to calculate both syndyne and synchrone dust orbits. The program also determines the position of the nucleus (in (ξ, η) co-ordinates) for various times τ prior to the observation date (see for example the direction of motion of the nucleus in Fig.7b). Table 2 shows the steps involved in such calculations.

TABLE 2

Summary of Steps involved in Calculating Dust Orbits

1. Input → comet orbital elements
→ observation date
→ Earth orbital elements
→ values of μ required
→ various release dates
2. Calculate the comet's orbital period and its orbital radius and true anomaly for a given date
3. Calculate heliocentric latitude and longitude for the comet
4. Repeat 2+3 for the Earth
5. Calculate the Earth-Comet distance
6. Calculate the Earth centred latitude and longitude for the comet
7. Determine the cometocentric co-ordinates of the Earth
8. For each release date calculate the comet's orbital radius and true anomaly
9. For each release date and particle size determine the orbital eccentricity of the released dust particle. Test to see if the particle goes into an elliptical or hyperbolic orbit.
10. Calculate the orbital elements of the grain's orbit, semimajor axis a_d , eccentricity e_d , time of perihelion passage t_{0d} , and period P_d . Calculate the angular velocity of the particle under reduced gravity. Hence find the particle's orbital radius r_d , and true anomaly with respect to its own orbit and that of the comet's.
11. Calculate the cometocentric co-ords. of the dust particle in terms of (ξ, η) ($\zeta = 0$)
12. Transform $(\xi, \eta, 0)$ to sky plane co-ords. (L, M, N)
13. Plot synchrone or syndyne orbits

Calculating Dust Grain Trajectories

Step 2.

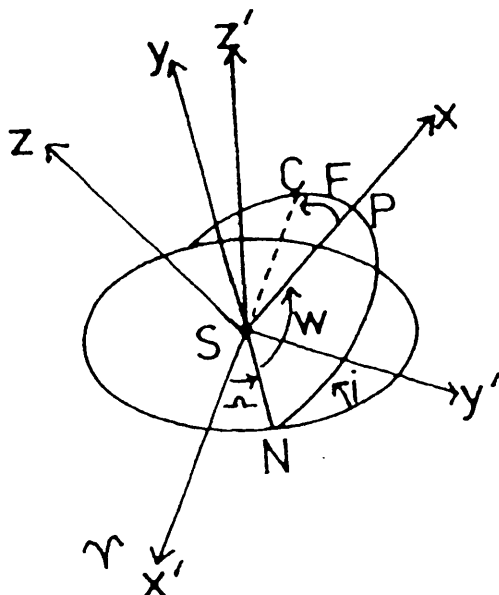
The orbital period of the comet is given by

$$P = 2\pi \sqrt{\frac{A^3}{GM}}$$

where GM is in units of (AU)³(day)⁻² and A is the semi-major axis in AU.

For orbital radius r, and true anomaly F, see App.I

Step 3.



Let (x', y', z') be the heliocentric ecliptic co-ordinates with α and β' the longitude and latitude, based on the ascending node (i.e. ignoring R(-Ω)), and (x, y, z) the orbital co-ordinates.

Then,

$$\begin{pmatrix} x' \\ y' \\ z' \end{pmatrix} = P(-i) R(-w) \begin{pmatrix} x \\ y \\ z \end{pmatrix}$$

The rotations are negative for anti-clockwise rotations.

Using the definitions of P(θ) and R(θ) above we have,

$$\begin{pmatrix} x' \\ y' \\ z' \end{pmatrix} = \begin{pmatrix} x \cos(w) - y \sin(w) \\ x \cos(i) \sin(w) + y \cos(i) \cos(w) - z \sin(i) \\ x \sin(i) \sin(w) + y \sin(i) \cos(w) + z \cos(i) \end{pmatrix}$$

Now $x = r \cos F$, $y = r \sin F$ and $z = 0$ so,

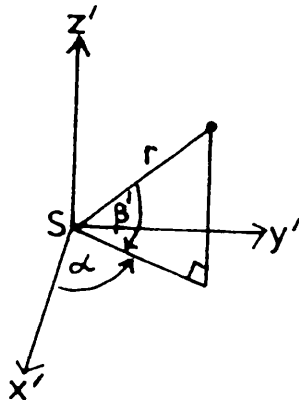
$$\begin{pmatrix} x' \\ y' \\ z' \end{pmatrix} = \begin{pmatrix} r \cos(F+w) \\ r \cos(i) \sin(F+w) \\ r \sin(i) \sin(F+w) \end{pmatrix}$$

From the diagram below $x' = r \cos(\beta') \cos(\alpha)$, $y' = r \cos(\beta') \sin(\alpha)$, and $z' = r \sin(\beta')$, therefore by equating x' , y' and z' ,

$$\sin(\beta') = \sin(i) \sin(F+w)$$

$$\tan(\alpha) = \cos(i) \tan(F+w)$$

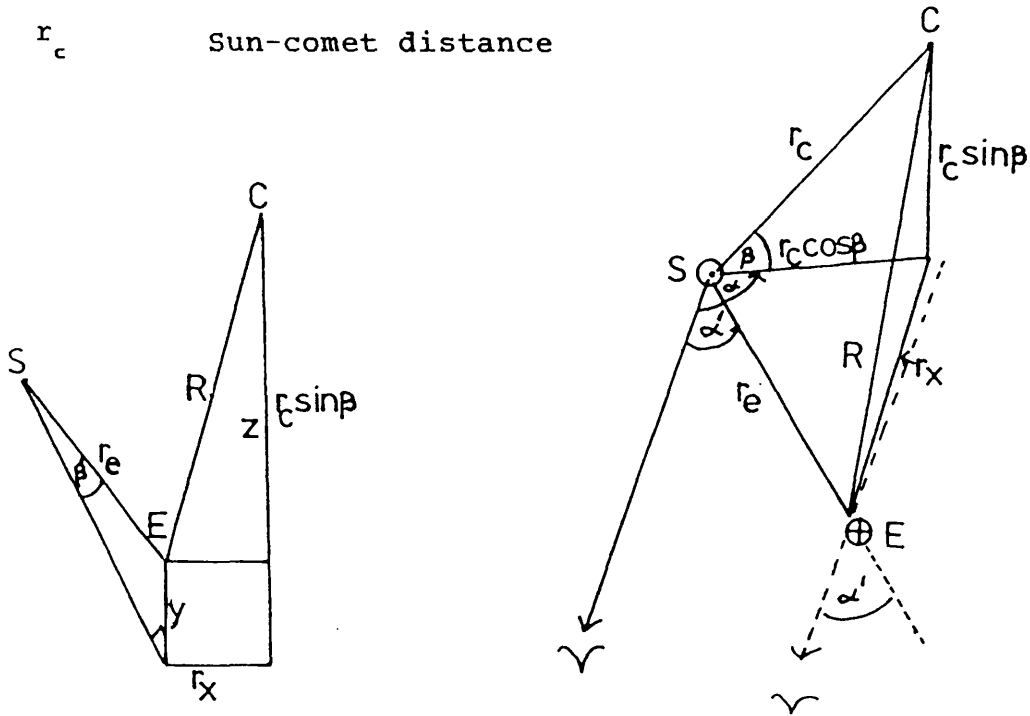
Hence the latitude and longitude can be expressed in terms of the true anomaly, the orbital inclination and the argument of perihelion. The true heliocentric longitude β , is then found from $\beta = \beta' + \Omega$, where Ω is the longitude of the ascending node.



Steps 5+6.

Let α be the longitude of the comet
 β be the latitude of the comet
 α' longitude of the Earth
 β' latitude of the Earth
 R comet-Earth distance
 r_e Sun-Earth distance
 r_c Sun-comet distance

in Sun centred
co-ordinates



From the diagram and using the cosine formula

$$r_x = [r_e^2 \cos^2 \beta' + r_c^2 \cos^2 \beta - 2r_e r_c \cos \beta' \cos \beta \cos(\alpha - \alpha')]^{1/2}$$

and

$$R^2 = r_x^2 + (r_c \sin \beta - r_e \sin \beta')^2$$

hence,

$$R = [r_c^2 + r_e^2 - 2r_e r_c \sin \beta \sin \beta' - 2r_e r_c \cos \beta' \cos \beta \cos(\alpha - \alpha')]^{1/2}$$

Step 7.

The cometocentric co-ordinates of the Earth (ξ, η, ζ) are given by,

$$\begin{pmatrix} \xi \\ \eta \\ \zeta \end{pmatrix} = P(\pi)R(\nu) \begin{pmatrix} x' \\ y' \\ z' \end{pmatrix} - \begin{pmatrix} r_c \\ 0 \\ 0 \end{pmatrix} \quad \text{+ve clockwise rotation}$$

where (x', y', z') are the orbital co-ordinates of the Earth and in turn are given by,

$$\begin{pmatrix} x' \\ y' \\ z' \end{pmatrix} = R(\omega)P(i)R(\Omega) \begin{pmatrix} x \\ y \\ z \end{pmatrix} \quad \text{+ve clockwise rotation}$$

which performs the transformation from ecliptic Earth co-ordinates to orbital Earth co-ordinates. The orbital co-ordinates are given by,

$$x = r_e \cos\alpha' \cos\beta'$$

$$y = r_e \sin\alpha' \cos\beta'$$

$$z = r_e \sin\beta'$$

The cometocentric co-ordinates of the Earth are thus found by substitution and matrix multiplication.

Steps 8-10.

See App.II.

Step 11.

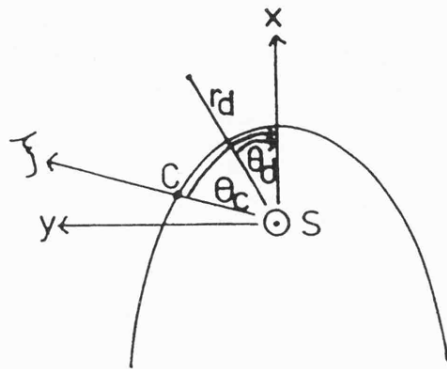
The cometocentric co-ordinates of the dust particle ($\xi, \eta, \zeta=0$) can be simply found using the following parameters,

r_d = distance from the cometary nucleus

r_c = Sun-comet distance

θ_c = The true anomaly of the comet

θ_d = The true anomaly of the dust particle

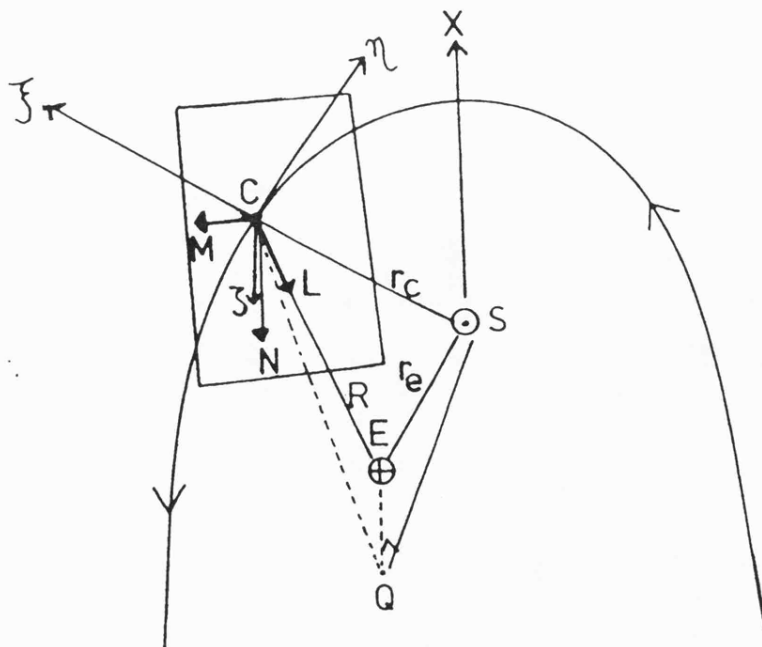


$$\xi = r_d \cos(\theta_c - \theta_d) - r_c$$

$$\eta = r_d \sin(\theta_c - \theta_d)$$

Step 12.

A point on the orbital plane needs to be projected onto the sky plane. Consider the following diagram.



Let r_e = Sun-Earth distance

r_c = Sun-comet distance

R = Earth-comet distance

Q = The projected Earth position
in the comet's plane

(ξ, η, ζ) are the right hand set of cometocentric axes

The photographic plane is shown as a square normal to the vector R . L, M, N represent a right hand system of sky plane axes such that the L axis points towards the Earth, the M axis is the projection of the positive ξ axis onto the sky plane and N forms the right hand set.

The Earth's cometocentric co-ordinates are (ξ_e, η_e, ζ_e) and

$R = \Delta = (\xi_e^2 + \eta_e^2 + \zeta_e^2)^{1/2}$. By use of directional cosines the transformation to the cometocentric system L, M, N is given by,

$$L = \frac{\xi_e}{\Delta} \xi + \frac{\eta_e}{\Delta} \eta + \frac{\zeta_e}{\Delta} \zeta$$

$$M = \frac{(\eta_e^2 + \zeta_e^2)^{1/2}}{\Delta} \xi - \frac{\xi_e \eta_e \eta}{\Delta(\eta_e^2 + \zeta_e^2)^{1/2}} - \frac{\xi_e \zeta_e \zeta}{\Delta(\eta_e^2 + \zeta_e^2)^{1/2}}$$

$$N = \frac{\zeta_e \eta}{(\eta_e^2 + \zeta_e^2)^{1/2}} - \frac{\eta_e \zeta}{(\eta_e^2 + \zeta_e^2)^{1/2}}$$

A specified point in the tail will have co-ordinates $(\xi_T, \eta_T, 0)$ in the cometocentric system, hence,

$$L_o = \frac{\xi_e \xi_T}{\Delta} + \frac{\eta_e \eta_T}{\Delta}$$

$$M_o = \frac{(\eta_e^2 + \zeta_e^2)^{1/2}}{\Delta} \xi_T - \frac{\xi_e \eta_e}{\Delta(\eta_e^2 + \zeta_e^2)^{1/2}} \eta_T$$

$$N_o = \frac{\zeta_e}{(\eta_e^2 + \zeta_e^2)^{1/2}} \eta_T$$

and for the Earth $L_e = \Delta$, $M_e = N_e = 0$.

The required projection of a given tail point onto the sky

plane is the intersection of the straight line joining $L_0 M_0 N_0$ and $L_e M_e N_e$ with the plane $L=0$. The M, N co-ordinates of the projected point are then found to be,

$$M_T = \frac{\Delta}{(\Delta^2 - \epsilon_e \epsilon_T - \eta_e \eta_T)} (\eta_e^2 + z_e^2)^{1/2} \epsilon_T - \frac{\epsilon_e \eta_e \eta_T}{(\eta_e^2 + z_e^2)^{1/2}}$$

$$N_T = \frac{\Delta^2 z_e}{(\eta_e^2 + z_e^2)^{1/2}} \frac{\eta_T}{(\Delta^2 - \epsilon_e \epsilon_T - \eta_e \eta_T)}$$

(see App. II)

2.2 Comet Halley

Like most comets in the past, Comet Halley was taken as a sign for superstitious terror. Observations can be traced back to 256BC. Comet Halley made an appearance in 1066 to mark the fall of King Harold at the Battle of Hastings. In 1303 the artist Giotto used Halley to represent the star of Bethlehem in his painting "The Adoration of the Magi". Comet Halley also came under the scrutiny of Edmond Halley who successfully predicted its return in 1759 (Halley, 1704). The first photographs of Halley were taken in 1910, when due to favourable positioning, the comet proved a spectacular object for astronomers. The Earth also passed through the outer tail in 1910, causing wild belief in some areas that cyanogen poisoning was at hand (Hughes, 1984).

P/Comet Halley was recovered (at V magnitude =24) on 16 October 1982 by Jewitt and Danielson, (1982), using a 480s CCD exposure on the 5m Mount Palomar telescope. This marked the beginning of intensive ground based observations.

CCD images of Halley during September 1984 showed a weak coma (Spinrad et al., 1984b). In December 1984 Halley was detected in the infrared for the first time (Birkett et al, 1985). It was not until 17 February 1985, that detection of a gaseous species (CN emission bands), was made by Wyckoff et al, (1985). Various estimates of the nuclear rotation period were made (Whipple, 1980, Lecacheux et al., 1984a, 1984b) by studies of 1910 images or via photometry. Estimates varied between 8-48 hrs. Sekanina and Larson(1985) performed a separate study of previous 1910 photographs and declared that the rotation period was 52 hrs. This value was later confirmed by

spacecraft results (Smith et al., 1987) and by the pre-perihelion photometry performed by Leibowitz and Brosch, (1986). However the photometric observations of Millis and Schleicher (1986) and Williams et al., (1987) have indicated a double-peaked lightcurve with $P=7.4$ days. To explain this lightcurve, Sekanina (1987) and Julian (1987) have put forward the idea that the nucleus is both rotating and precessing.

By August 1985 Halley possessed a well developed coma (McCarthy et al, 1985) and by October many typical cometary emissions had been discovered, such as C_2 , C_3 , CN, OH etc (Larson, Wyckoff and Wehinger, 1985). The detection of water was announced on 1985 October 29 by Brooke et al, (1985) and was later confirmed by Mumma et al, (1985) on 12 December 22.

From August 1985 onwards the presence of many jets were recorded (Hammel and Cruikshank, 1985, Koutchmy and Lecacheux, 1985, Landgraf, 1985). The first signs of a cometary tail was reported by Barbieri et al, (1985) in November. By 4 December 1985, the motion of knots, kinks, streamers and rays could be followed in a well developed plasma tail (Jewitt et al, 1985), while at the end of December a dust and a plasma tail could be well separated (Emerson, 1985).

During 1986 the comet gave spectacular displays of disconnection events (reported by many observers) and multi-structured dust tails. On 31 March 1986 Wickramasinghe and Allen recorded an infrared spectrum, showing, they believe, an emission band due to organic material (1986). It has been suggested that this organic substance could be the dark material seen covering the nucleus in the later Giotto images.

During 1986 five spacecraft encounters with Comet Halley

created a wealth of new scientific data. Vega's 1 and 2 encountered Comet Halley on 6 and 9 March respectively. Their experiments showed that the nucleus is an irregular, elongated body measuring 14x7.5km. The surface was discovered to be dark with an albedo of 0.04 ± 0.02 . In the inner coma region five jets were observed and some of these had multiple components (Vaisberg et al., 1986, Sagdeev et al., 1986). Spectra of the dust grains revealed three different types,

- a) those with elemental composition similar to type C1 carbonaceous chondrites (C, O, Na, Mg, Si, Ca, Fe),
- b) as above, but with the presence of considerable ^{additional} amounts of carbon and nitrogen,
- c) dust grains composed of H_2O or H_2O/CO_2 - clathrate ice.

The Giotto spacecraft encountered Comet Halley on 14th March 1986. The on-board camera showed that only minor parts of the nuclear surface are active, with dust jets restricted to the sunlit hemisphere (Keller et al., 1986).

2.3 The Application of Finson - Probst Theory
 to the Dust Tail of Comet Halley

Introduction

Chapter 1.3 has discussed some ideas concerning the possible relationships between comets, asteroids, meteors, meteorites, Brownlee particles and the Zodiacal Light. Chapter 5 takes a closer look in terms of their physical properties. How do these phenomena compare with respect to dust sizes and orbits?

Dust grains ejected from a cometary nucleus are in the submicron to submillimetre size range. Several authors (e.g. Sekanina + Schuster, 1978a+b) have increased the upper end of this range to centimetre sized grains for P/d'Arrest and P/Encke. The DIDSY experiment on board the Giotto spacecraft indicated the presence of larger grains at least up to 1000 μ m for P/Halley, (MacDonnell et al., 1986).

Giese et al. (1978) have stated that Zodiacal Cloud grains are in the range 0.1 to 1mm (100 to 1000 μ m). Fraundorf et al. (1982) found 2-50 μ m dust grains in the Earth's upper atmosphere, although 90% of these were found to be aggregates of other 0.1 μ m grains. Meteor streams have grains in the millimetre range. Cometary grains are therefore comparable in size.

Divine et al. (1980) summarise β_{max} (μ_{min}) values found for a range of comets. The β values range from \approx 0.5 to 2.7 depending on the comet and type of tail studied. Such large β values are attributed to very small particles or 'fluffy' particles which have very low densities. Like P/Halley, P/West (1976VI) showed a multi-structured dust tail. The analysis (Sekanina + Farrell, 1980) showed that the striations seen in the tail were not simple synchronic bands. These striations

were not at the predicted positions and they changed position with time in an unusual manner. The explanation given was that the dust grains were bursting or fragmenting as they moved away from the nucleus, thus giving rise to smaller fragments which resulted in two types of striations. The first type had parent and fragment β values of ≈ 0.6 while the second type had β values of ≈ 2.7 . The large differences in β values were assumed to be due to two types of grains; magnetite grains (absorbing material) for which $\beta_{\max} \approx 1.7$ and olivine grains (dielectrics) for which $\beta_{\max} \approx 0.6$ (see Fig.4).

There has been much speculation concerning the continual dust source required to supply the Zodiacal Cloud in an equilibrium state. Many authors (Whipple, 1955, Delsemme, 1976) favour short period comets as the suppliers with P/Encke being the main supplier. More up to date estimates, based on theoretical, observational and dynamical studies of dust tails (e.g. Sekanina, 1976b, Kresak, 1980b) show that although P/Encke is the main supplier, the contribution (<1%) of the present population of comets is too low to maintain a steady-state. Price et al. (1980) estimated that the total mass of the dust grains inside 2AU was $\approx 2 \times 10^7$ g. To maintain this quantity against decay (the lifetime of the cloud being $\approx 10^5$ years) required 5000 comets which each had a mass loss rate similar to P/Kohoutek of 2×10^3 g, or one comet emitting dust for 5000 years. The question still remains open as to whether dust via asteroid collisions could supply some or all of the required material (Dohnanyi, 1976, Kresak, 1980b, Ney, 1982).

Recently the IRAS satellite discovered interplanetary dust bands. These bands were found to be parallel to the

ecliptic and at ± 10 degrees ecliptic latitudes. After subtraction of the contribution from the Zodiacal Light, the 0 degree band still remained. Dermott et al.(1984) have suggested that these bands were due to the projections of the dust surrounding three asteroid families, Themis (0°), Koronis (0°) and Eos (-10° to $+10^\circ$). However it must be remembered that the amount of Zodiacal Light subtracted could well be in error. The amount of dust entering the Zodiacal Cloud depends on a number of factors including, with respect to comets,

i) The frequency with which the grains are ejected
i.e. activity and size of the nucleus.

ii) The size distribution of grains.

iii) The ability to eject into elliptical circumsolar orbits.

i) Although short period comets have many revolutions around the Sun, it is the longer period comets which are the greater sources of dust. However one needs to bear in mind the problems of "hidden" dust and condition iii).

ii) Mie theory (Chapter 5) is used to compute theoretical infrared spectra, given a grain composition and size distribution. The theoretical spectra are compared with the observed spectra and the parameters varied. Such a size distribution, considered between 1-20 μ m is, however, only relative. Finson-Probstein theory gives rough estimates of the sizes involved but not the absolute size distribution. Such a distribution may be found if the light intensity of each synchrone is modelled against a hypothetical distribution of grains of given albedo and composition. However such work is not covered in this thesis.

During the past few years, observations at far-infrared

wavelengths have revealed large dust grains which have been previously hidden from optical studies. Such "hidden" mass could easily alter the calculations of mass loss from comets and hence the amount of dust required to keep the Zodiacal Cloud in an equilibrium state, particularly if the grains are large or in large quantities. One discovery of the IRAS mission was the presence of an infrared dust tail, trailing the comet P/Tempel 2 (Davies et al., 1984). The tail, just detectable at $\lambda = 25\mu\text{m}$, was extremely narrow and existed for a short arc of the comet's orbit. Finson-Probstein analysis by Eaton et al. (1984) revealed that the grains were in the submillimetre range ($\beta < 0.01$), probably with low albedos (explaining the lack of detection at optical wavelengths) and were emitted at least 1,500 days prior to the observation date. Very small particles could also have such low β values although they would not emit efficiently at $25\mu\text{m}$.

Another IRAS discovery was the infrared dust tail of Comet IRAS-Araki-Alcock 1983d (Walker et al., 1984). Grain radii were found to be in the range 5 to $30\mu\text{m}$ along the tail, which was quite apparent at $60\mu\text{m}$ although a little noisier at $100\mu\text{m}$. Many other infrared tails were found (Sykes et al., 1986). Some were associated with known comets such as P/Encke and P/Gunn. The tails of P/Encke and P/Gunn existed both in front and behind the comet, but the tail of the former was not "attached" to the comet's head indicating non-continuous ejection. An analysis of the dust orbits revealed that the grains were large and had been ejected with low velocities. Although no "tails" could be matched with any known meteor streams, it could be that we are seeing the initial links between comets and meteor streams.

iii) Dust grains contributing to the Zodiacal Cloud are affected by the Poynting-Robertson effect. The outcome of such an effect is to cause the grain to lose ^{angular} momentum and eventually spiral into the Sun. For perfectly absorbing grains (e.g. magnetite) the solar radiation pressure is thought of as a momentum carried by the Solar photons. The grains re-radiate this radiation isotropically so there is no net force exerted on the grain. However, in the Solar reference frame, the grains are losing momentum, which is equivalent to a mass loss and thus suffer a "drag" force. For scattering grains (e.g. pure olivine) the momentum lost is in the scattering beam. The lifetime against total mass decay is of the order of several thousand years.

Section 2.1 has described in detail the physical and mathematical background to Finson-Probstein theory and how this theory is applied in programmable form. Many large scale images of Halley were obtained, using the 1.2m UK Schmidt Telescope during 1985/1986. A selection of plates, exposed mainly through an R filter/emulsion combination (collecting light which has been scattered by dust grains) was used to study the temporal variations of the dust tail. Finson-Probstein theory was applied to determine the ejection times of the dust grains, the grain size distribution and the type of orbit into which a particular grain is projected.

Testing the Computer Programs

Ozeki (1986) published a series of plots showing the expected synchrone and syndyne loci, for Comet Halley during 1985 and 1986. Adopting their values of μ and ejection times and noting their own scaling which differed for each image, the author produced similar plots (Fig.A). During February and early

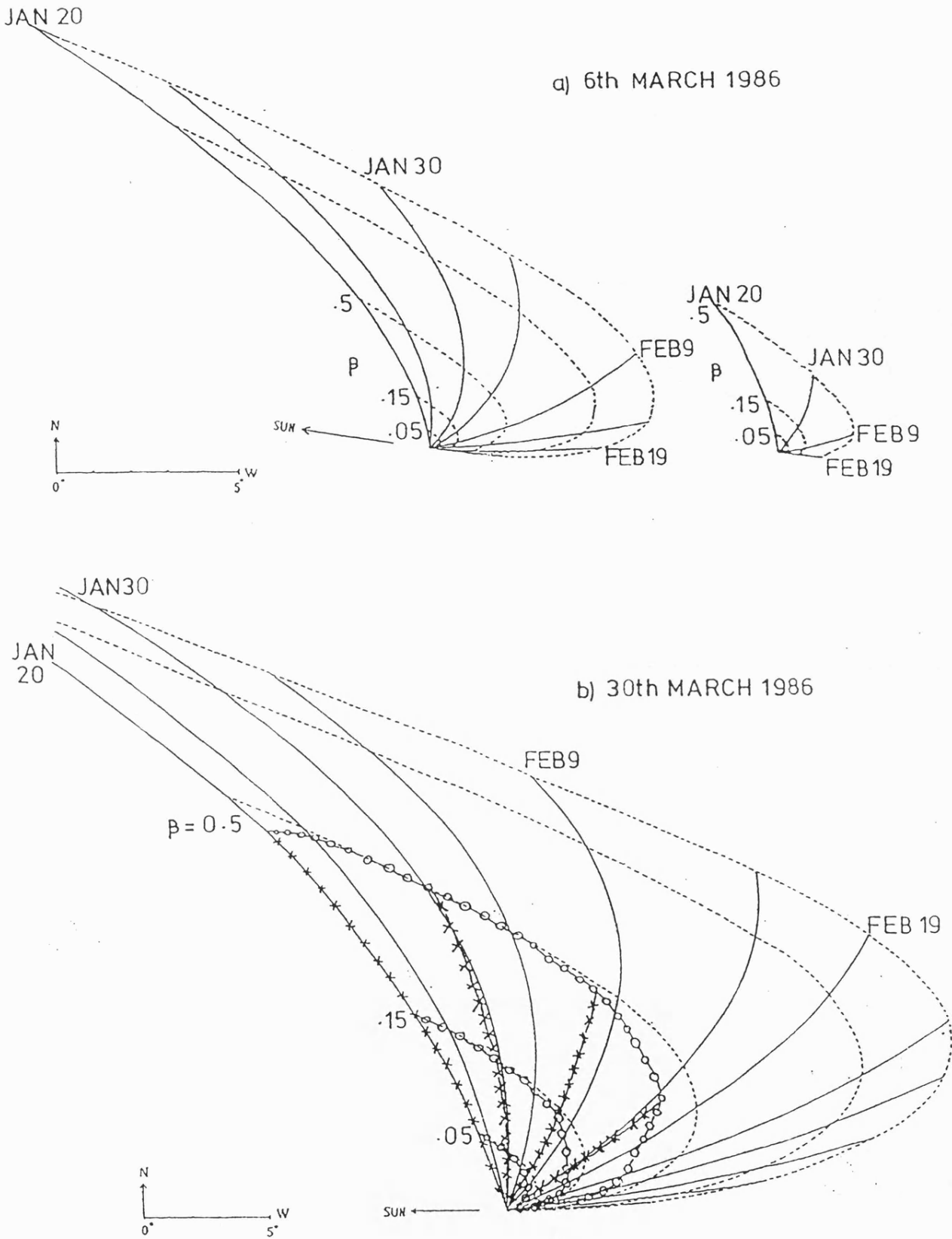


Fig. A A comparison between theoretical syndynes and synchrones. This author's synchrones (ejection times 20/1/86, 30/1/86, 6/2/86 and 19/2/86) and syndynes ($\beta=0.05, 0.15, 0.50$) are compared to those of Ozeki (1986) (who extends his range to $\beta>1$). Fig. a) depicts Ozeki's results on the left and this author's on the right. When overlaid these two are perfectly matched. At a later date (30/3/86) when the line of sight was rapidly changing differences become apparent (Fig. b)

-x-x-x-x-x-x- this author's synchrones
 -o-o-o-o-o-o- " " syndynes

March both the synchrones and syndynes matched well (Fig.a). During late March and April, when the line of sight from the comet to the Earth was rapidly changing, there were obvious differences (Fig.b). Either the synchrones or the syndynes or sometimes both, were not in the same expected positions. However the application of the program to Comet Halley was continued and the results compared favourably with other observer's results.

The Observations

The selected Schmidt plates were digitised using Cosmos, with the exception of UR10778 which was badly fogged. Analysis of this image was performed from a plate photograph (courtesy of ROE photolabs). Table 3a gives the plate details, while Table 3b and Figure 5 (images 1-12) describe or show the development of the dust tail during 1985/1986. The images in Fig.5 are in chronological order, dating from 15/11/85 (R10544) to 6/6/86 (R11215). The arrowed vector points to the Solar direction.

For each image:

1. The image was displayed on the Args screen and using Starlink software, enhanced in a variety of ways, to try and reveal details in the dust tail. Of the various methods used the simplest and most effective, was to vary the intensity range displayed on the screen. When an image is displayed the intensity range is automatically fitted to 256 different intensity bins of either a grey or a colour scale. A chosen smaller intensity range (i.e. a subset) will also be allocated to these 256 levels, and intensities outside of this range will be squeezed into the last few bins on either side of the new range. This method enhances faint features whilst saturating those features of higher intensities.
2. A Tektronix printer (Type No.4632) was used to obtain a copy of each image. the printer had been previously altered so that the image had the same linear scale on both x and y axes.
3. The scale in AU per mm, mid-exposure time in GMT, Sun direction, point of maximum intensity (in x,y units) and Julian date were determined. The comet's position for that date was determined from the Halley ephemeris.

TABLE 3a

UK Schmidt Plates of Comet Halley(for Finson and Probststein Analysis.)

<u>Date</u>	<u>Exposure</u> <u>(mins.)</u>	<u>GMT</u> <u>(h m)</u>	<u>Plate No.</u>	<u>CPS⁺</u> <u>("p.p.)</u>	<u>Δ</u> <u>(AU)</u>	<u>R</u> <u>(AU)</u>
15/11/85	63.2	16 19	R10544	4	0.74	1.72
4/12/85	40.0	11 26	R10568	20	0.66	1.44
9/12/85	25.0	12 00	V10580	14	0.72	1.36
14/12/85	60.0	10 31	R10597	35	0.80	1.28
22/2/86	2.0	18 26	UR10778*		1.40	0.65
4/3/86	2.0	18 35	B10800	35	1.20	0.76
9/3/86	8.0	19 12	J10822	35	1.09	0.83
13/3/86	15.0	18 18	R10858	35	0.99	0.89
17/3/86	15.0	17 58	R10878	35	0.89	0.95
23/3/86	15.0	19 29	R10922	24	0.73	1.04
28/3/86	10.0	17 56	R10939	24	0.61	1.12
4/4/86	15.0	15 55	R10983	28	0.48	1.22
10/4/86	40.0	15 04	R11016	28	0.42	1.32
11/4/86	5.0	15 56	R11022	12	0.42	1.33
14/4/86	40.0	17 11	R11034	32	0.43	1.38
19/4/86	21.0	18 30	R11060	17	0.50	1.45
11/5/86	75.0	9 15	R11106	9	1.11	1.78
27/5/86	60.0	8 37	JB11120	7	1.64	2.01
2/6/86	75.0	9 14	R11135	7	1.83	2.09
26/6/86	90.0	8 25	R11202	7	2.60	2.41
6/7/86	90.0	8 39	R11215	7	2.89	2.54

<u>Plate</u>	<u>Emulsion/Filter</u> <u>Combination</u>	<u>Effective</u> <u>Width (nm)</u>	<u>Gaseous</u> <u>Contamination</u>
R	IIIaf + RG630	630-690	[OI]
V	IIad + GG495	495-650	C ₂ , [OI]
UR	IIIaf	+ -690	C ₂ , C ₃ , [OI], CN, CO ⁺
B	IIao + GG385	385-500	C ₃ , C ₂ , CO ⁺ , CN
J	IIIaj + GG395	395-530	"
JB	IIao + GG395	395-500	"

+ CPS COSMOS Pixel Size in arcsec. per pixel

* UK Schmidt photograph

TABLE 3b

UK Schmidt Images - Temporal Variations of the Dust Tail

<u>Date</u>	<u>Plate No.</u>	<u>Description of P/Halley</u>
15/11/85	R10544	Halley is seen as a rounded nebulosity. No dust tail is present, but there is a hint of a jet feature.
4/12/85	R10568	This is the first Schmidt image to detect the dust tail.
9/12/85	V10580	Dust and plasma tails are just resolvable. Closely packed synchrotrons lie in the observed position of the dust tail (Fig.6)
14/12/85	R10597	The dust tail becomes extended but retains its narrow shape.
22/2/85	UR10778	The line of sight, from the Earth to the comet is such that we are seeing the dust tail "face on". The tail is now multi-structured (broad dust bands) and there is a strong antitail.
4/3/86	B10800	Multi-structured dust tail, antitail becoming less pronounced.
9/3/86	J10822	Multi-structured dust tail. Antitail is now absent.
13/3/86	R10858	Multi-structured dust tail.
17/3/86	R10878	Broad dust tail- no separate dust bands.
23/3/86	R10922	"
28/3/86	R10939	"
4/4/86	R10983	This image shows the transition between the tail appearing as a long extension and taking on a wide delta-shaped form.
10/4/86	R11016	Line of sight effects create a broad fan-shaped dust tail.
11/4/86	R11022	"
14/4/86	R11034	"
19/4/86	R11060	Broad fan shaped dust tail. Sunward spike starting to appear.
11/5/86	R11106	Dust tail is now viewed edge-on. The dust tail appears narrow ($\approx 2 \times 10^7$ km) and is accompanied by a sharp sunward spike ($\approx 5 \times 10^5$ km).
27/5/86	JB11120	Narrow dust tail with sunward spike.
2/6/86	R11135	"
26/6/86	R11202	"
6/7/86	R11215	Tail appears to shorten ($\approx 1 \times 10^7$ km). Sunward spike less prominent.

FIG 5 (1-6)

Figure 1

R10544

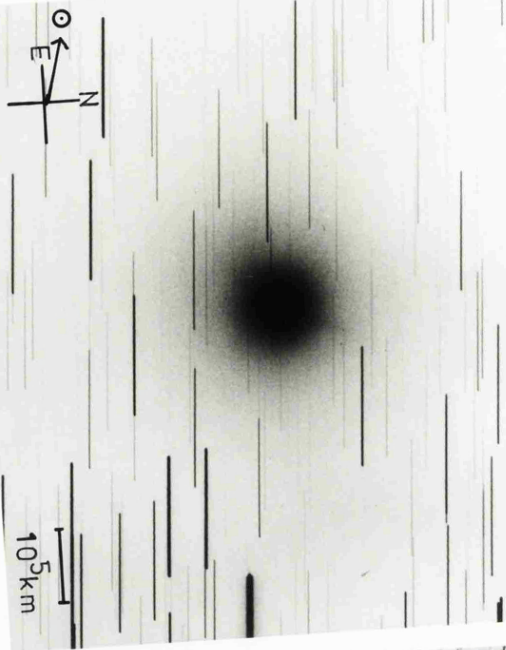


Figure 4

UR10778

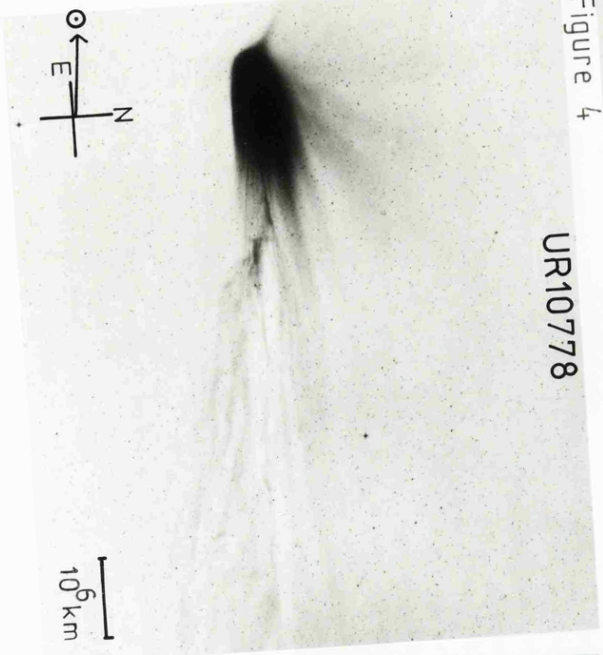


Figure 2

V10580

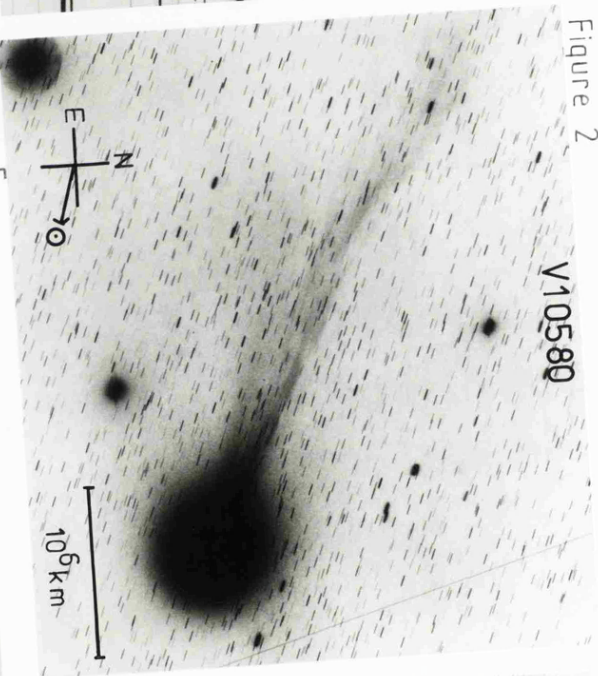


Figure 5

JB10829

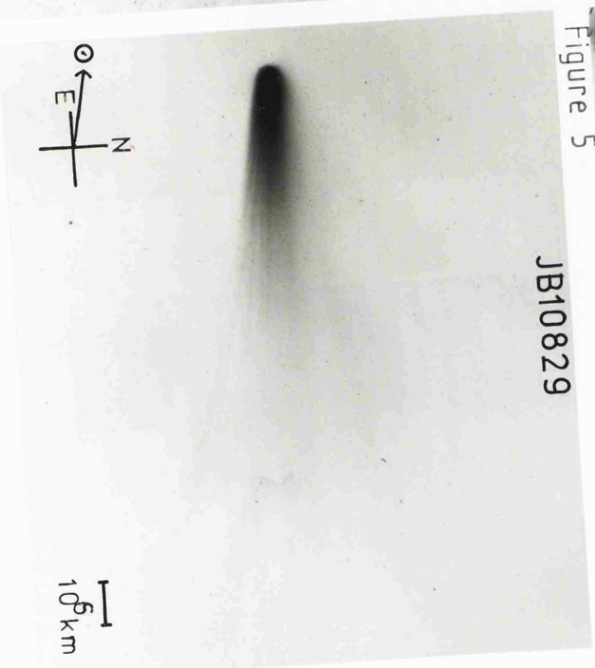


Figure 3

J10591

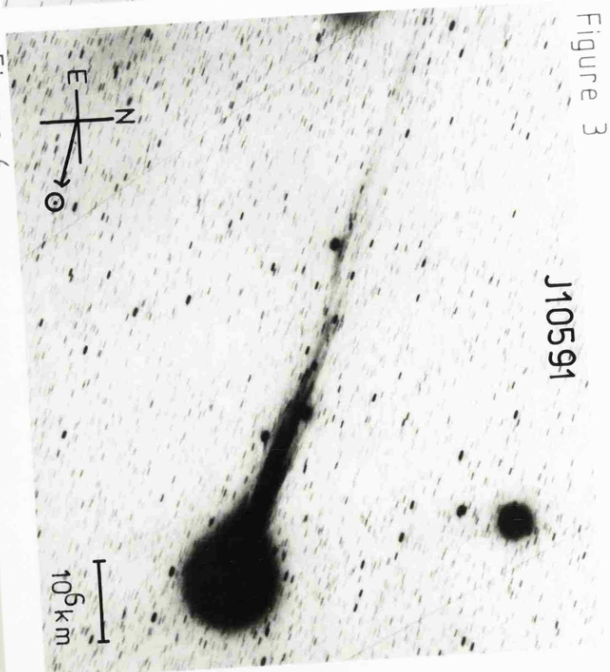


Figure 6

JB10879

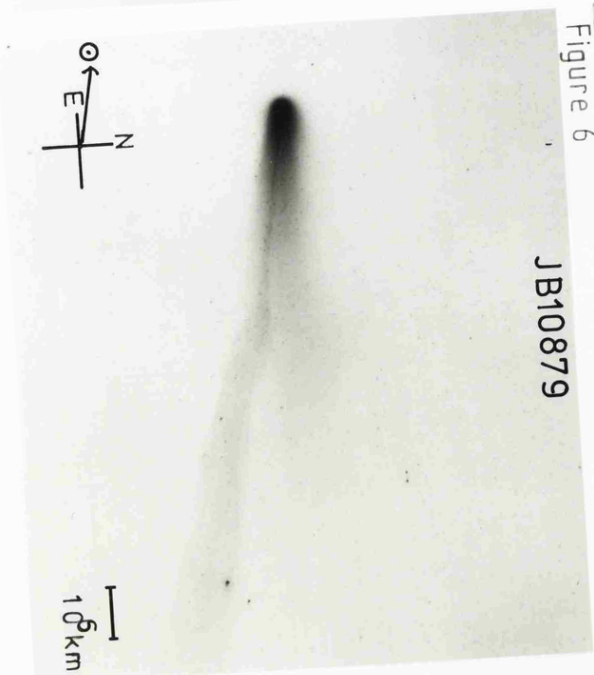


FIG 5 (7-12)

Figure 7

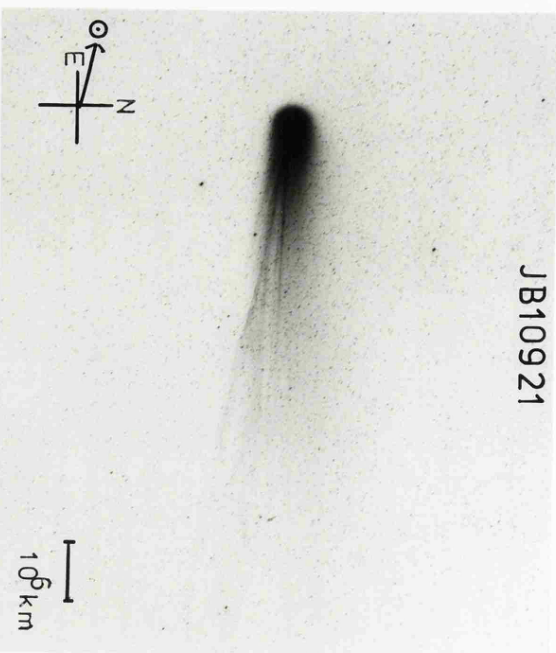


Figure 8

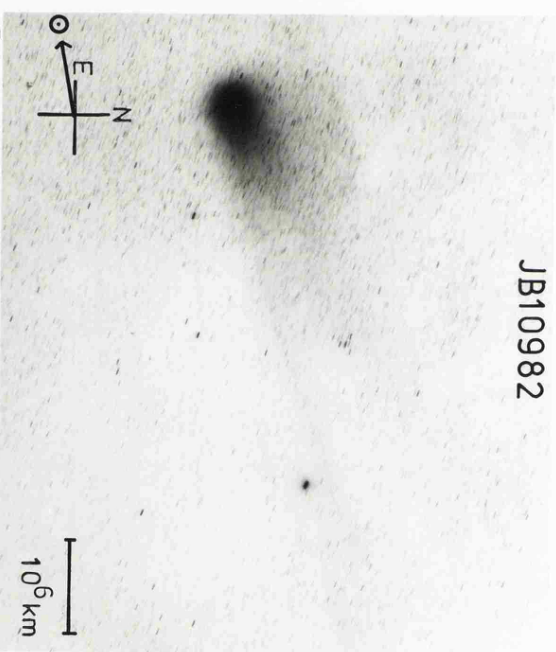


Figure 9

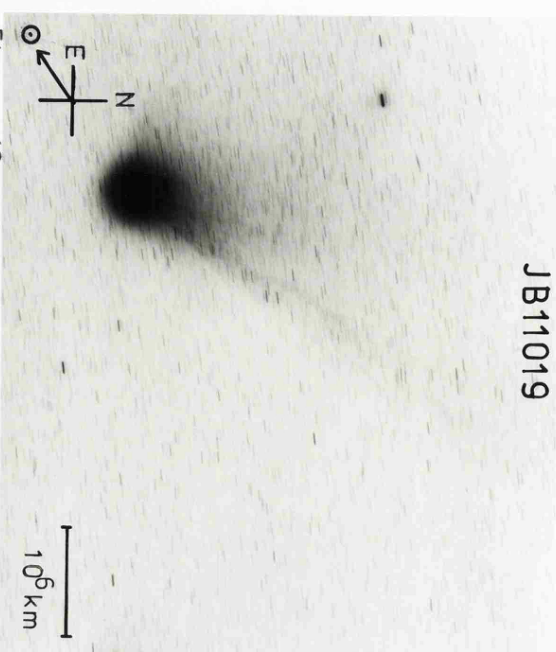


Figure 10

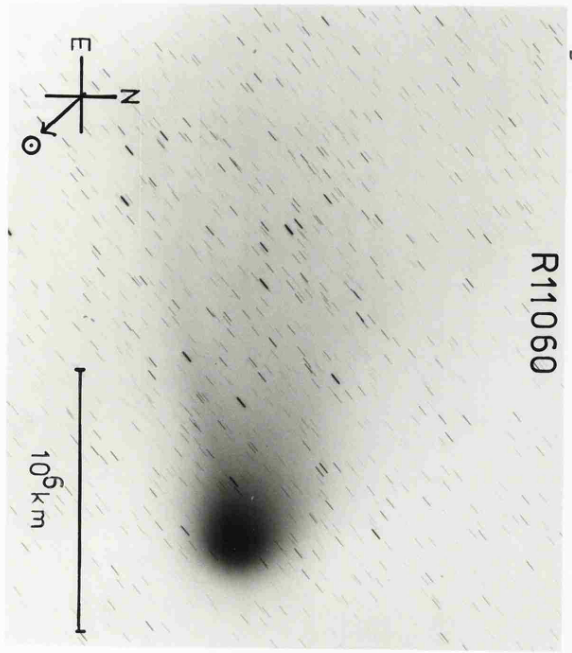


Figure 11

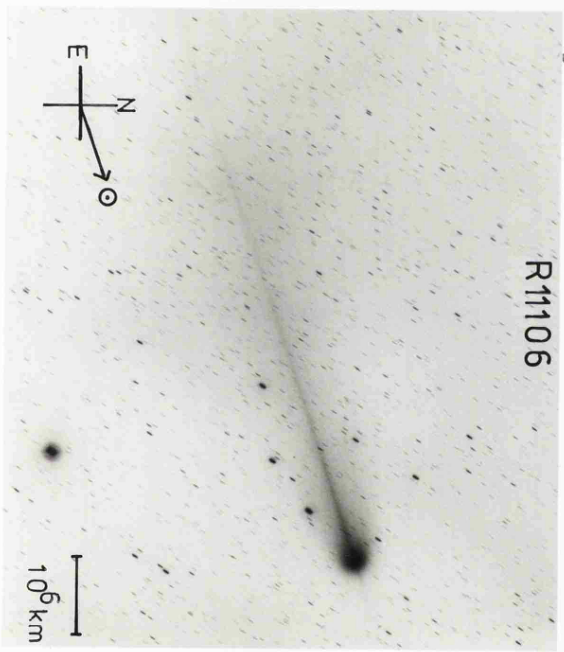
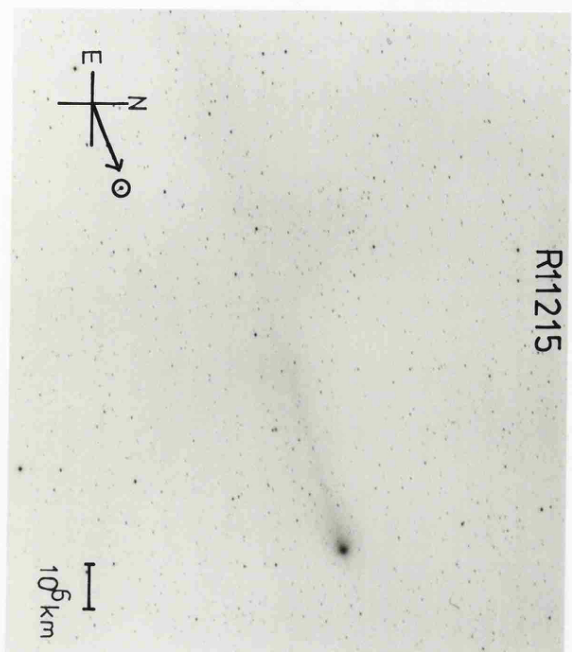


Figure 12



Dust Tail Analysis

How we view the dust tail of a comet depends on the extent of the tail and the line of sight conditions, from the Earth to the comet (see Fig.B). During early December the tail was viewed "edge-on" and only limited analysis could be performed. For example, Fig.6 shows the image V10580. Computed synchrones lie very close together and the precise dates of dust ejection are not clear. By February the comet was observed "face on" and the broad structures of the dust tail are clearly seen. These favourable observing conditions persisted until mid-March. Therefore the February/early March images provided the main data for the Finson-Probstein analysis.

Analysis of UR10778 - The Application of Synchrones

Table 3c shows an example of the standard computer output for UR10778. Various dust grain orbital elements are given for particular μ values and for a range of ejection times, τ . For a constant grain density, the larger the μ value the bigger the grain. Smaller grains have more eccentric orbits and smaller "a" values. Ejection dates are given in intervals of 10days prior to the observation date, $t_c = 22/2/86$. Perihelion passage is February 9th. Values of eccentricity, for all grain sizes, reach a maximum at perihelion. Dust orbital elements computed for t_c must be taken with caution as the grains have not theoretically left the nucleus at this point. As an example, a grain for which $\mu=0.90$, which is ejected from the nucleus at time $\tau=2446464.3$, moves into an orbit whose properties are given by the elements e to t_0 . At time t_c this grain will have cometocentric co-ordinates (0.014,0.010) and sky plane co-ordinates (0.002,0.003). The positions of those grains with equal values of μ will be linked to produce

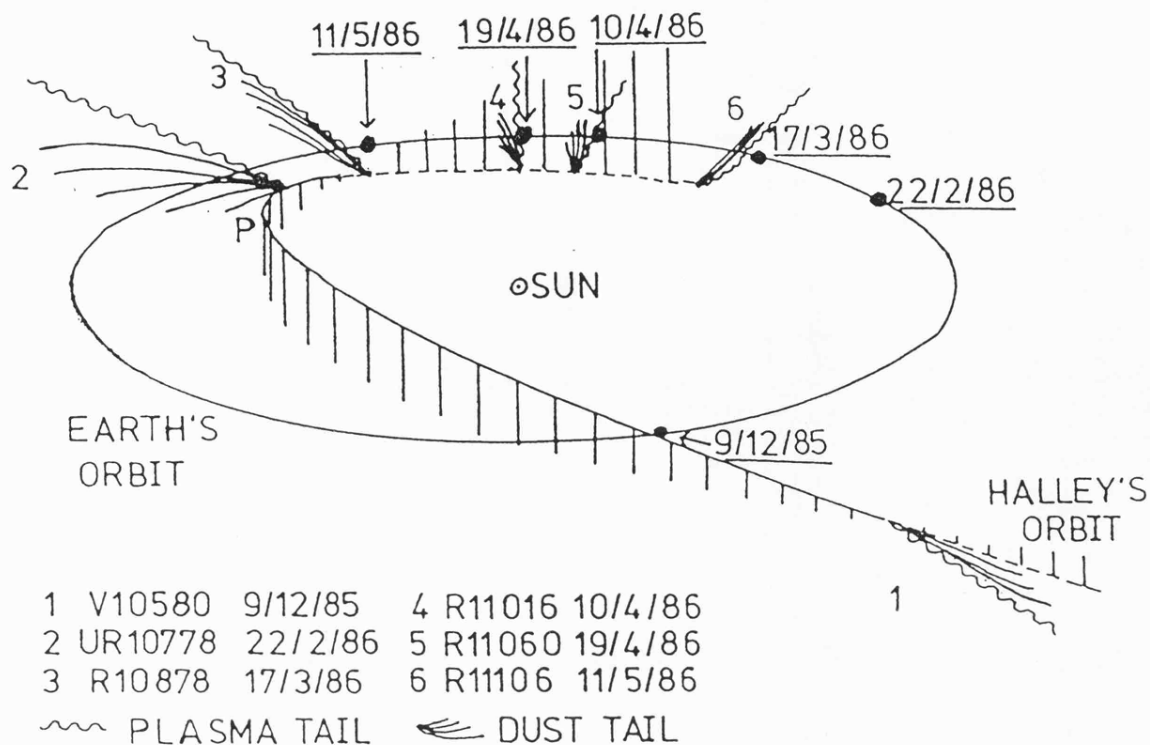


Fig. B This figure shows the relative positions of the Earth (solid circles) and P/Halley (numbers 1-6) during 1985/1986. The positions refer to dates on which UK Schmidt images were taken. The dotted line indicates when the comet's orbit is below the ecliptic. Straight line markers from the comet's orbit give some indication of how far the nucleus is, above or below the ecliptic plane. The plasma tail is approximately in the anti-solar direction.

- 1 Around this time (9/12/85) the comet crossed the ecliptic plane and the dust tail is viewed edge-on.
- 2 The comet is high above the ecliptic. Viewed from the Earth (22/2/86), the tail is seen face-on and reveals its multi-structured nature. Part of the tail appears to point in the Sunward direction (the antitail).
- 3 Again the comet crosses the ecliptic plane (17/3/86) and the various dust bands can no longer be seen.
- 4+5 The comet is now below the ecliptic plane but still within the Earth's orbit. The tail is viewed end-on producing the characteristic delta-shaped form seen in early April.
- 6 The same conditions apply as in 4+5, but from the Earth the tail is viewed edge-on, producing the long narrow dust tail seen in May.

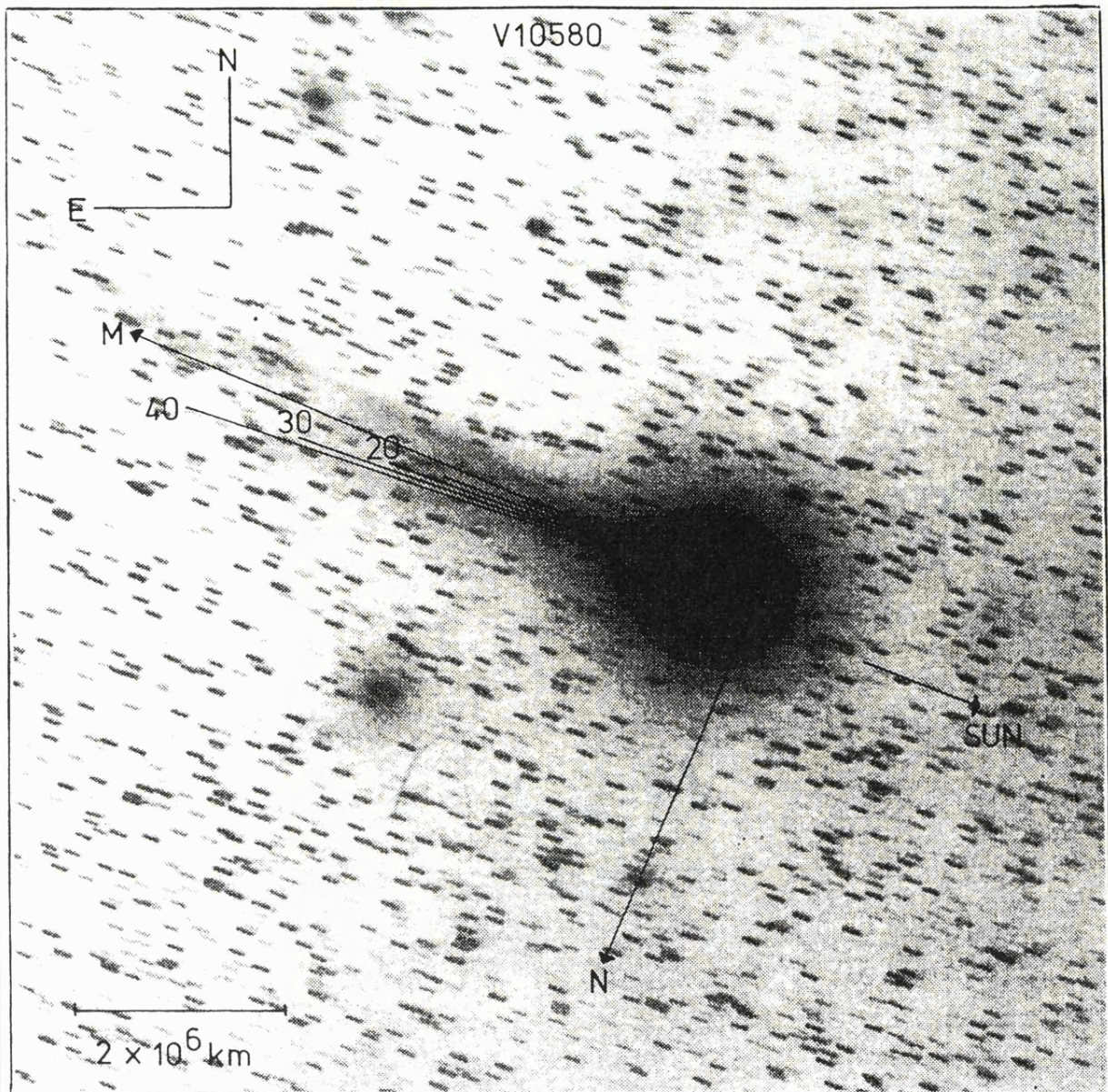


Fig.6. Schmidt image V10580. This early image of Comet Halley depicts both the dust and the plasma tail. The dust tail is just separated from the plasma tail. Line of sight conditions are such that the synchrones for ejection dates, up to 40 days previous, are lying very close together.

TABLE 2c

EXAMPLE OF A TYPICAL COMPUTER OUTPUT FOR EINSON-PROBSTEIN
ANALYSIS URI0778 1986 FEBRUARY 22

P/Halley Orbital Elements
a=17.9359AU e=0.9673 i=162.2378° q=58.1331°
w=111.8534° perihelion JD=2446471.161

tc JD=2446404.3 1986 February 22 GMT=18.7HRS.

I	DATE (+18.7hrs)	EA	AA (AU)	BA (degrees)	TA	EA (degrees)	EA	EA (degrees)	E (AU)	D (AU)	M (AU)	N (AU)
μ=0.95	22/2/86	1.060	9.765	1.73	2446471.7	0.653	37.48	0.000	0.000	0.000	0.000	0.000
2446474.3	12/2/86	1.070	8.376	0.47	2446471.3	0.655	37.42	0.002	0.001	0.001	0.000	0.000
2446464.3	2/2/86	1.068	8.702	-1.00	2446470.8	0.660	37.03	0.007	0.005	0.001	0.002	0.002
2446454.3	23/1/86	1.055	10.712	-2.07	2446470.6	0.665	36.26	0.012	0.014	-0.002	0.005	0.008
2446444.3	13/1/86	1.041	14.366	-2.63	2446470.5	0.668	35.36	0.014	0.025	-0.008	0.008	0.011
2446434.3	3/1/86	1.030	19.955	-2.87	2446470.6	0.669	34.51	0.014	0.035	-0.015	0.011	0.014
2446424.3	24/12/85	1.021	28.409	-2.95	2446470.6	0.668	33.74	0.014	0.044	-0.021	0.014	0.014
2446414.3	14/12/85	1.014	41.979	-2.96	2446471.0	0.668	33.04	0.012	0.052	-0.028	0.017	0.017
μ=0.90	22/2/86	1.165	3.595	3.33	2446472.2	0.653	37.48	0.000	0.000	0.000	0.000	0.000
2446474.3	12/2/86	1.164	3.185	0.89	2446471.5	0.657	37.37	0.004	0.001	0.002	0.000	0.000
2446464.3	2/2/86	1.179	3.264	-1.91	2446470.6	0.667	36.59	0.014	0.010	0.002	0.003	0.003
2446454.3	23/1/86	1.154	3.861	-3.99	2446470.0	0.677	35.09	0.023	0.025	-0.005	0.009	0.009
2446444.3	13/1/86	1.126	4.787	-5.13	2446469.9	0.682	33.35	0.027	0.049	-0.017	0.016	0.016
2446434.3	3/1/86	1.102	5.962	-5.67	2446470.1	0.684	31.70	0.027	0.069	-0.030	0.022	0.022
2446424.3	24/12/85	1.084	7.339	-5.88	2446470.4	0.684	30.21	0.025	0.087	-0.043	0.027	0.027
2446414.3	14/12/85	1.070	8.910	-5.93	2446470.8	0.683	28.88	0.022	0.102	-0.055	0.032	0.032
μ=0.10	22/2/86	17.684	0.037	18.04	2446477.0	0.653	37.48	0.000	0.000	0.000	0.000	0.000
2446474.3	12/2/86	18.608	0.033	4.60	2446472.7	0.688	36.53	0.034	0.011	0.014	0.004	0.004
2446464.3	2/2/86	18.369	0.034	-9.97	2446467.9	0.774	30.74	0.115	0.091	0.010	0.027	0.027
2446454.3	23/1/86	17.171	0.039	-22.27	2446464.0	0.856	21.01	0.167	0.242	-0.052	0.067	0.067
2446444.3	13/1/86	15.746	0.047	-31.22	2446461.4	0.910	10.85	0.160	0.408	-0.146	0.106	0.106
2446434.3	3/1/86	14.472	0.055	-35.54	2446460.0	0.945	1.66	0.113	0.553	-0.244	0.140	0.140
2446424.3	24/12/85	13.416	0.065	-42.11	2446459.6	0.971	-6.40	0.047	0.673	-0.338	0.168	0.168
2446414.3	14/12/85	12.551	0.007	-45.53	2446459.9	0.992	-13.48	0.028	0.771	-0.427	0.191	0.191
μ=0.05	22/2/86	36.313	0.018	18.56	2446477.2	0.653	37.48	0.000	0.000	0.000	0.000	0.000
2446474.3	12/2/86	38.213	0.016	4.73	2446472.7	0.690	36.48	0.036	0.012	0.015	0.004	0.004
2446464.3	2/2/86	37.722	0.016	-10.25	2446467.8	0.780	30.43	0.121	0.096	0.010	0.029	0.029
2446454.3	23/1/86	35.257	0.019	-22.93	2446463.8	0.866	20.35	0.174	0.255	-0.055	0.070	0.070
2446444.3	13/1/86	32.328	0.022	-32.21	2446461.0	0.924	9.86	0.165	0.428	-0.153	0.110	0.110
2446434.3	3/1/86	29.707	0.026	-38.80	2446459.5	0.962	0.41	0.114	0.580	-0.256	0.145	0.145
2446424.3	24/12/85	27.535	0.031	-43.61	2446458.9	0.990	-7.85	0.042	0.704	-0.354	0.174	0.174
2446414.3	14/12/85	25.754	0.035	-47.24	2446459.1	1.013	-15.09	0.038	0.804	-0.446	0.198	0.198

KEY
 1 dust grain ejection time
 EA eccentricity of dust grain orbit
 AA distance between Focus (Sun) and Perihelion
 BA orientation of grain's perihelion with respect to comet's orbit
 TA time of perihelion passage
 EA true anomaly of dust grain
 EA true anomaly of the dust grain
 EA cometocentric co-ordinates relative to the nucleus at time tc
 EA sky plane co-ordinates relative to the nucleus at time tc
 EA Sun-grain distance
 EA true anomaly of the dust grain
 EA cometocentric co-ordinates relative to the nucleus at time tc
 EA sky plane co-ordinates relative to the nucleus at time tc

syndynes. The positions of those grains which have been ejected at the same instant in time will be linked to produce synchrones.

As a rough test, by choosing values of μ and a range of release dates, a series of syndynes were plotted to overlay the UR10778 image. No variation of syndyne values could match the curvature of the dust bands. The process was repeated for various synchrones (Fig.7a). The shape of these loci matched well. The synchrone dates on all figures are shown as integers, but are actually (Date + GMT), where GMT is the mid-exposure time of the observation date photograph.

Apart from the sharp antitail (pointing almost in the Solar direction), which is discussed in a later section, there are four "clear" synchrone bands on the image. Between the antitail and the February 1-3 synchrone band there is a general haziness where there are two vague synchrone bands. It was therefore assumed that the large dust bands seen during February and March were due to a series of major outbursts occurring at specific times or over specific intervals of time.

To date there have only been two sets of published synchrone dates. The first, published by Sekanina (1986a) concerns images taken between February 20-24. Below are his calculated outburst dates, compared with the author's results from the UR10778 image. The other set of results was published by van de Weg (1986) and concerns synchrone dates calculated from a photograph taken on February 22. Van de Weg's dates correspond to certain points on the synchrones and not to the width of the bands themselves.

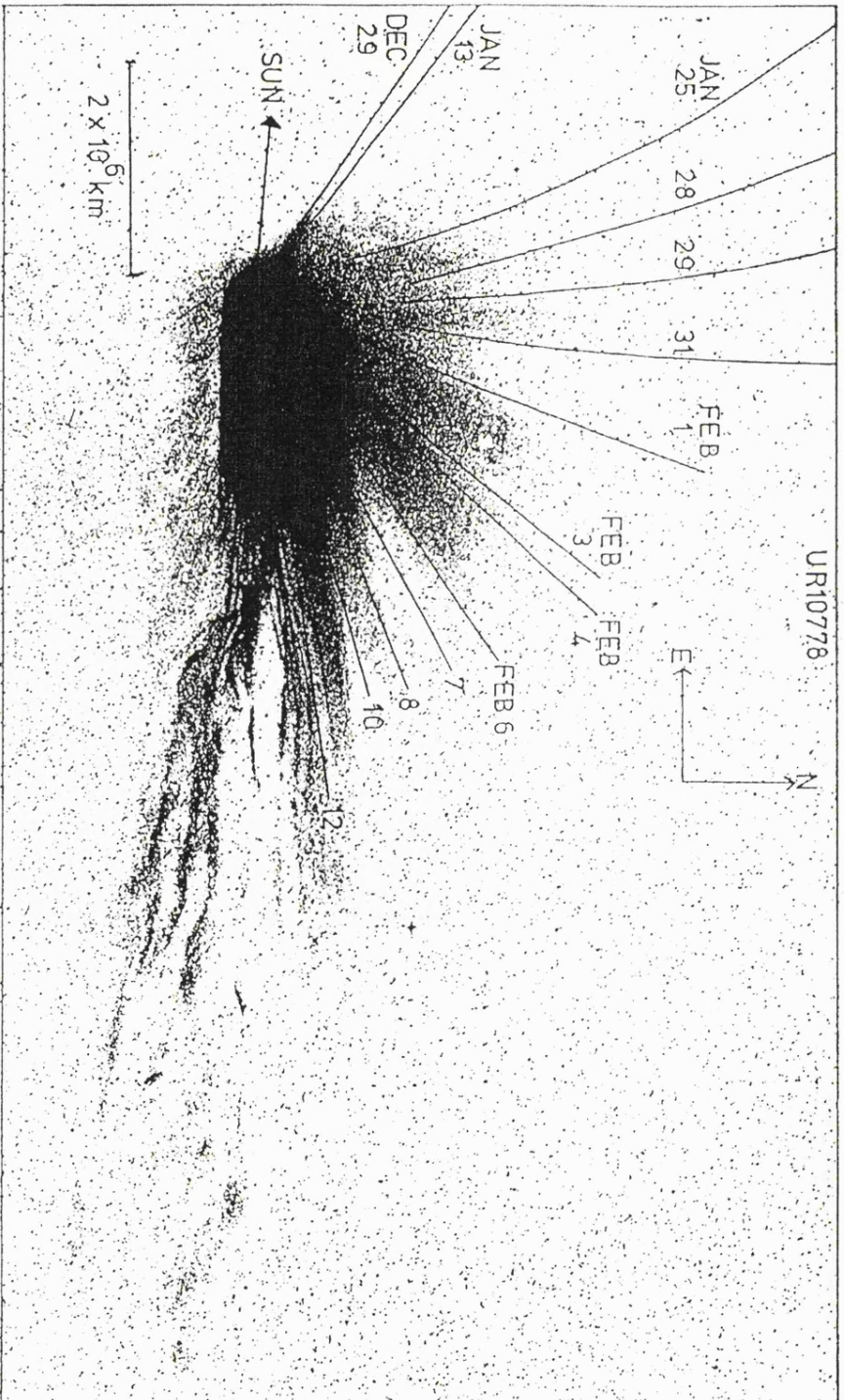


Fig. 7a. Schmidt image UR10778 showing both the plasma tail and the dust tail. The dust tail is composed of many different "bands", each corresponding to a range of ejection times prior to the observation date (22/2/86). The solid lines represent synchronones of arbitrary length.

UR10778

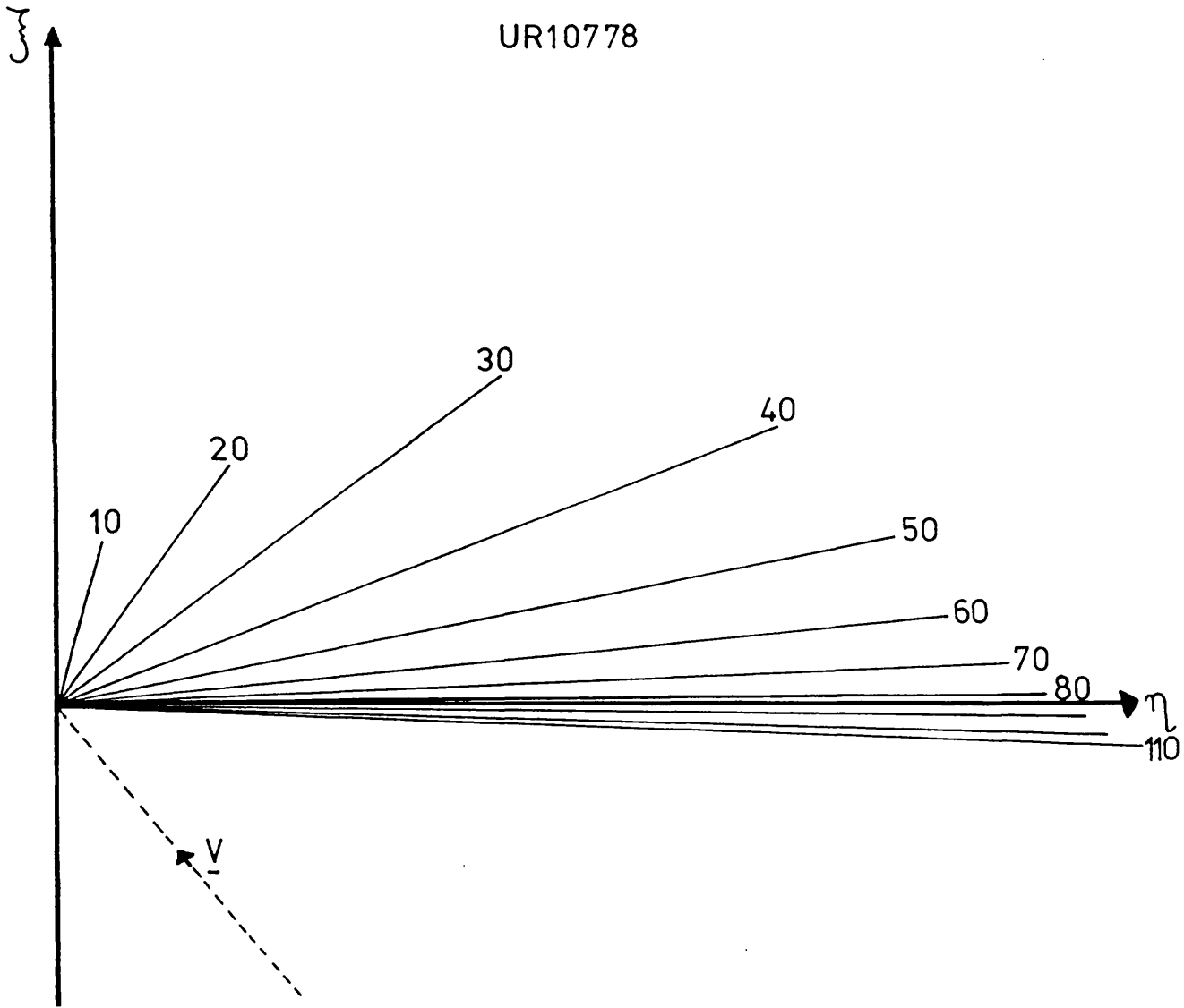


Fig.7b. Cometocentric co-ordinates of various synchrones. The synchrones are the loci of grains which have been emitted 10, 20, ..., 110 days previous to the observations date (22/2/86). Note how the synchrones become close together for early emission dates. The vector V denotes the motion of the nucleus in the (ξ, η) plane.

<u>Sekanina</u>	<u>van de Weg</u>	<u>UK Schmidt</u>
	August 6 1985	Prior December 1985
January 29.6613	January 30.4	January 29.8-31.8
February 2.7613	February 2.9	February 1.8-3.8
February 5.0613	February 4.9	February 4.8-6.8
February 5.7613		
February 9.9613	February 11.6	February 10.8-12.8
February 10.5613		
February 12.8613		

As can be seen the three data sets compare favourably.

When dating the observed dust bands, each image is displayed on an ARGS device and Starlink software is used to enhance the features. The enhancing procedure boosts particular intensity ranges, but a side effect is to defocus parts of the image, thus broadening the dust bands. This may lead to incorrect dating and it is particularly important if the synchrone appears narrow (the antitails, for example) on the original image. There is also error involved in judging the width of the dust bands by eye. It was hoped that scans across the bands could show the true widths to, say, five percent intensity levels. However the bands are not so clearly defined and one scan interferes with the next. There is also a small error introduced by choosing one point (situated in a saturated image area) to represent the position of the nucleus. Bearing all these factors in mind the upper limit on the error of a synchrone bandwidth is $\pm 1/2$ day.

Dust Ejection Times and Correlation with Outbursts

By computing and overlaying synchrones, four to six synchrone bands were found for the images B10800, J10822, R10858 and R10878. By the end of March the widely spaced dust bands were no longer apparent. However by displaying the late March/early April images in relative intensity contour form and greatly enhancing the resulting images, synchrone dates could be applied to "extensions of contours" or small features. For example, R10922 (Fig. 8) showed three faint features. The first (A) could be the relic of the previous antitail, while the broad features, (B) and (C) each correspond to the merger of two synchrone bands seen earlier on the UR10778 image. Images R11034 and R11060 (Figs. 9+10) show a fan-shaped dust tail and synchrones have been matched to certain contour extensions. Table 4 gives the details of all synchrone dates.

In general, the analysis shows three main periods of major emission.

1. Prior to December 1985.
2. 1986 January 13 - 1986 March 2.
3. Post 1986 March 12.

Clearly, the multistructured dust tail is due to the presence of the same synchrones on all images. Any variations from image to image are due to plane of sky effects, or recent dust grains being ejected.

Why should we see such prominent synchrone bands at these specific times? As there are no complete divisions between the dust bands (i.e. no dark "gaps"), it would suggest that dust grains are continuously ejected from the nucleus, but at specific times a more active area (or areas) faces the solar direction, leading to an increase in dust production rate. The

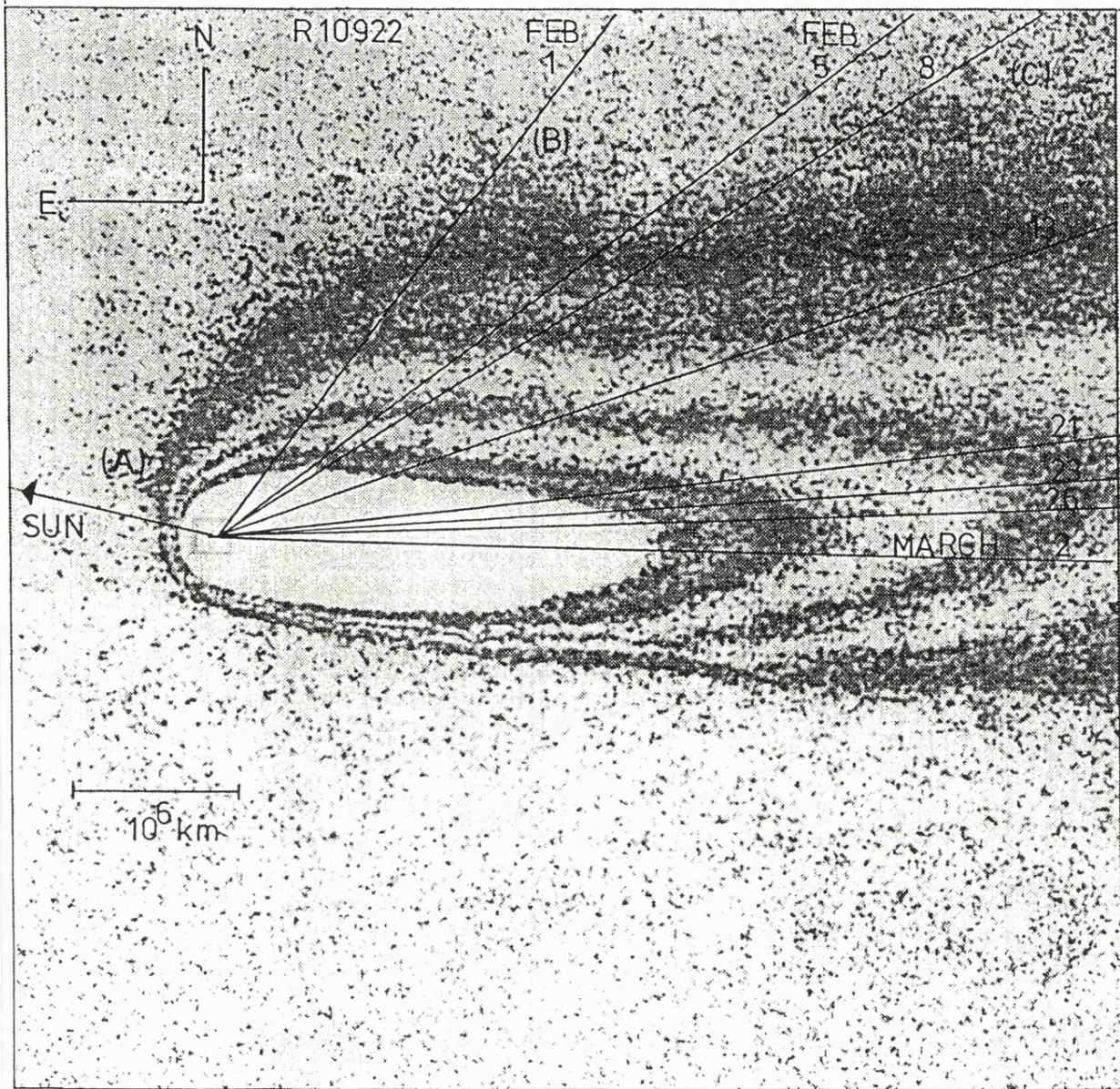


Fig.8. Computerised Schmidt image R10922. The broad dust bands can no longer be seen, but there are faint extensions of the outer contours. Synchrones have been drawn to match these extensions and the "swinging" round of the inner contours in the main tail.

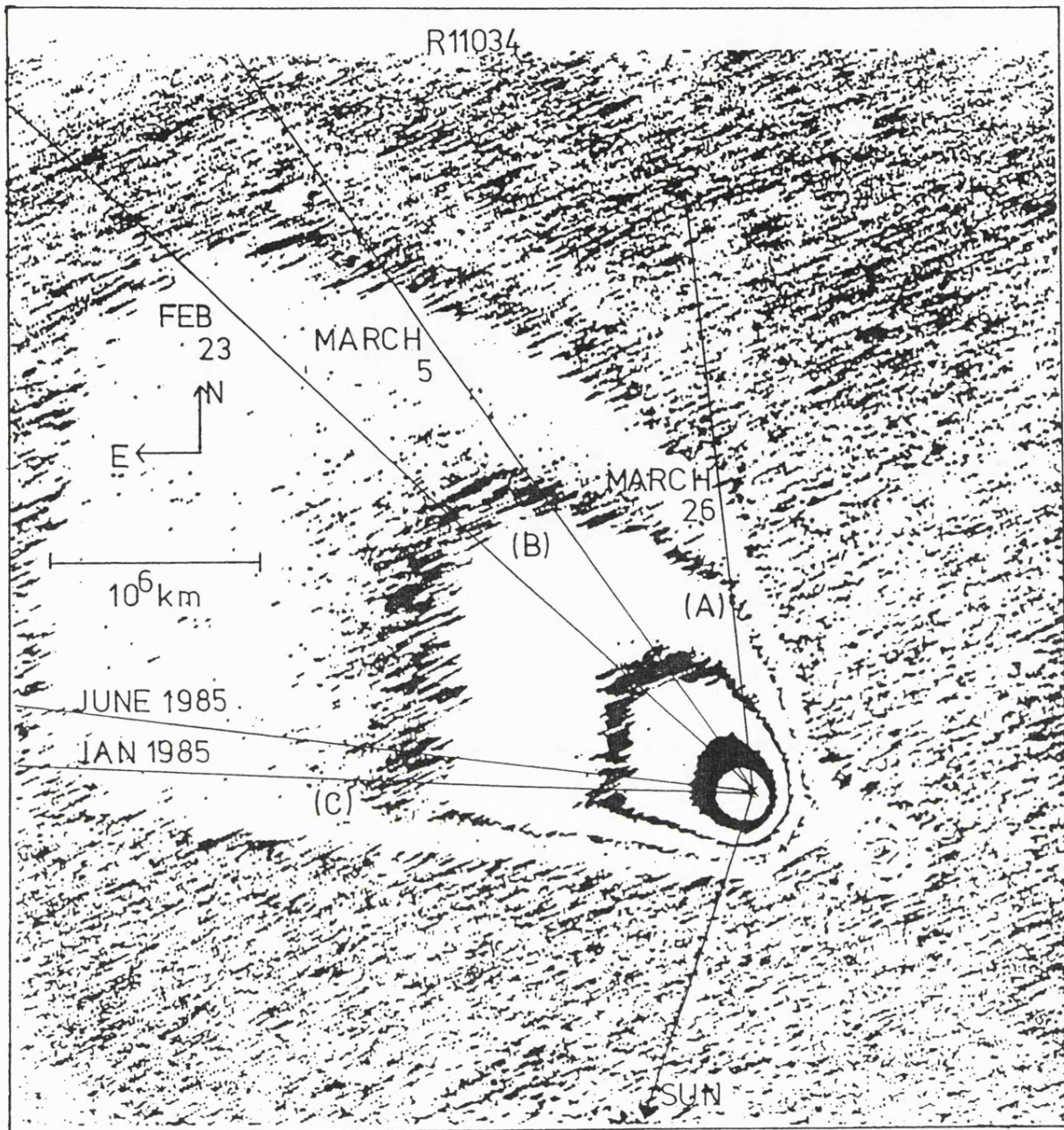


Fig.9. Computerised Schmidt image R11034 showing the delta-fan shaped dust tail. Synchrones have been drawn to match the distinct edges of the relative intensity contours.

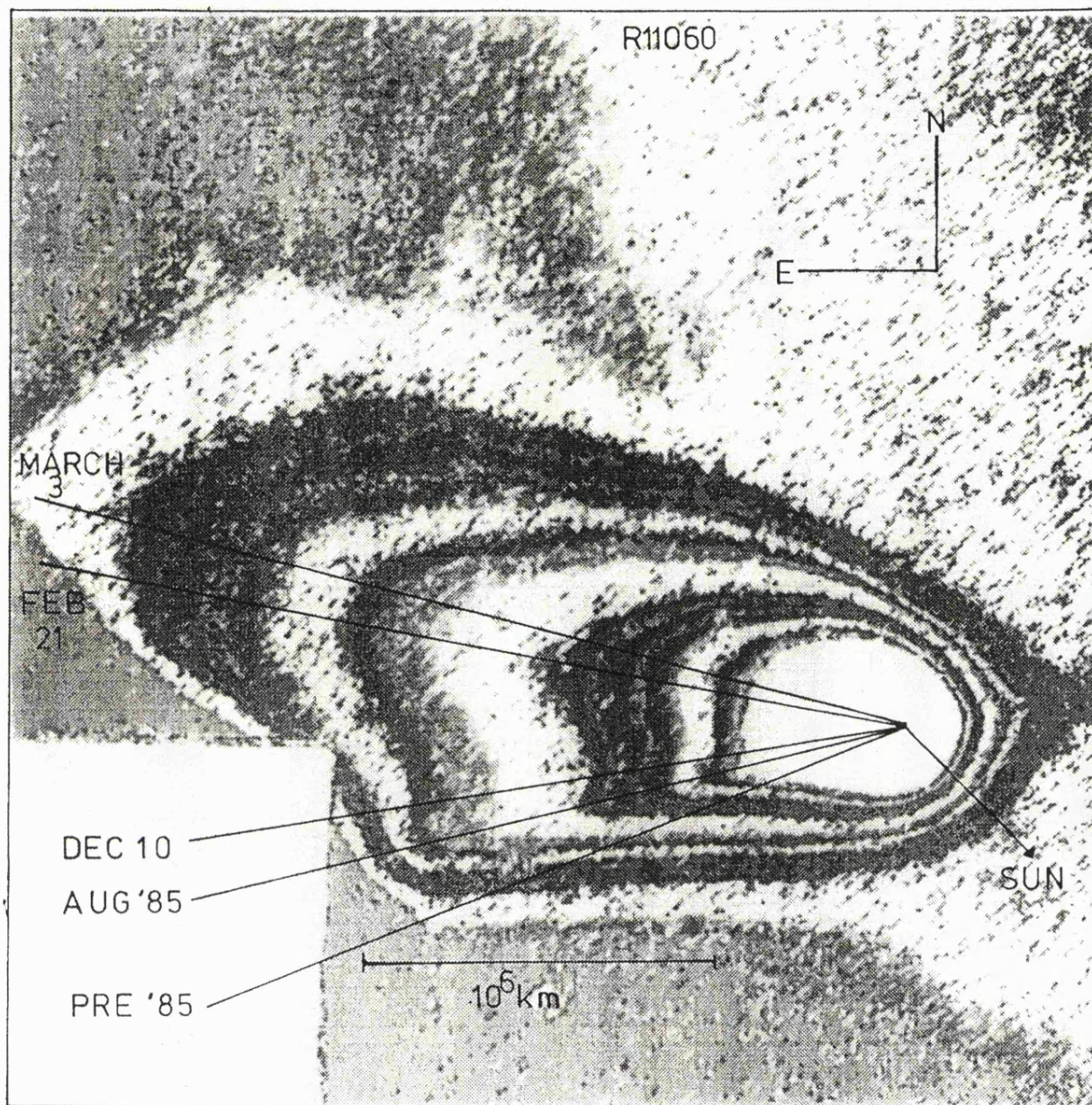


Fig.10. Computerised Schmidt image R11060 showing the delta-fan shaped dust tail and the beginnings of a sunward spike. Synchrones have been drawn to match the distinct "edges" of some of the relative intensity contours.

TABLE 4

Dust Tail Synchronone Dates found from UK Schmidt Plates of P/Halley

<u>Image</u>	<u>Antitail</u>	<u>Synchronones</u>
UR10778*	→Dec. 29 Jan 25 - 28 29 - 31	Feb 1 - 3 4 - 6 7 - 8 10 - 12
B10800*	→Dec. 2 Jan 15 - 23 24 - 29	Feb 3 - - 5 8 - 10 10 - 12 17 - 22 24 - 26
J10822*	Jan 13 - - - 28 Jan 31 - Feb 2	2 - 4 7 - 9 9 - 11 15 - 17
R10858*	→Oct. 14 Jan 20 - 22 23 - 29	Feb 1 - 3 3 - 5 10 - 12 14 - 19 21 - - 25 26 - March 2
R10878+	Jan 25 - 29	Feb 2 - - - 6 8 - 10 10 - - 14 15 - - - 23 24 - March 3
R10922+	Feb 1 - - - 5 8 - - - - - 13 21 - 23	26 - March 2
R10939+	Jan 27 - - - - - 6	Feb 26→
R11016x	→Nov. 11	
R11022x	Dec 22 - - - - - Jan 31	March 12→
R11060x	→Dec. 10	Feb 21 - - - - - March 3

*Image showing clear synchronone bands

+Gradual disappearance of synchronones

xDust tail becoming delta-fan shaped

idea that solar flares could have produced such strong outbursts can be rejected. Solar wind properties, quoted by Oyama et al., (1986), reveal no correlation between solar activity and the times of these outbursts. Internally generated explosions could not have repeated on such well defined time scales. Several synchrone bands correspond to outbursts observed by other authors (Table 5). For example, the synchrone bands 10-12 Feb. (UR10778, B10800, R10858) and 10-14 Feb. (R10878) correspond to the outburst on Feb 12.7 (Ney and Nutson, 1986). The Feb.26-March3 (R10858) and Feb.24-March3 (R10878) bands correspond to the outbursts between February 27 and March 3 (Berte, 1986). Some of the synchrone dates do not correspond to any known outburst. At the present time it is assumed that the outburst list is incomplete or that the increase in dust production was gradual enough so as not to be reported as a sudden outburst.

TABLE 5
Dates of Reported Major Outbursts

<u>Date</u>	<u>Reference</u>	<u>Comment</u>
13-14/10/85	Drechsel (1985)	Brightness increase.
8.5/11/85	R.Russell(p.c.)	Infrared outburst
12-16/11/85	Gammelgaard(p.c.)	Jet ejection
2.54/12/85	Wallis et al. (1985)	Dust and gaseous outburst seen when mapping in the ultraviolet.
4-5/12/85	S.F.Green(p.c.)	I.R. brightness increase
12.25/12/85	Kaminski et al. (1985)	Infrared brightness increase by 0.6 mag.
12/12/85	R.Russell(p.c.)	Infrared outburst
16.83/12/85	Itoh (1985)	Lyman alpha images varying
19/12/85	"	P=2.2 days, but with strong outbursts superimposed.
19.83/12/85	"	
25-26/12/85	"	
18-19/12/85	Nancay Team	OH productions show strong outburst.
24/12/85	Festou (1985a)	IUE monitored strong outburst factor x2 increase in brightness.
30/12/85	Festou (1985b)	IUE monitored outburst.
6.1/1/86	Larson and Levy (1986)	CCD images indicated a major outburst via occurrence of jets.
13/1/86	R.Russell(p.c.)	Infrared outburst
12.7/2/86	Ney and Knutson (1986)	Infrared increase in all filters
27/2/86- 3/3/86	Berte (1986)	Day to day variations episodic outbursts occurring in the infrared. Increase in brightness up to 1.5 mags.
2.4/3/86	West (1986)	Outburst had occurred 24 hrs prior to the observation date 2.4/3/86.
5.4-6.4/3/86	"	Schmidt observations show nucleus to be much brighter.
7.3/3/86	"	Major outburst, nucleus brighter by \approx 1 mag.
9/3/86	Festou et al. (1986)	IUE observations show a very strong outburst at roughly the same time as the Vega probe crossed the coma of P/Halley.
14/3/86	Cosmovici et al. (1986)	CCD images show a dust production increase by a factor x4.
18-19/3/86	Feldman et al. (1986)	IUE monitored outburst.
23.5-25/3/86	McFadden et al. (1986)	IUE monitored increase in brightness by factor x3 in 24 hrs.
24-31/3/86	S.F.Green(p.c.)	Silicate feature varying on a nightly basis.
7-11/4/86	R.Russell(p.c.)	Infrared outburst
(p.c.) denotes private communication		

Synchrone Bands - A Link to the Nuclear Rotation Period?

The number and duration of outbursts can reveal information concerning the rotation period and the number of active areas on the nuclear surface, see for example Sekanina (1986a). However the assumed rotation period has recently been questioned. Many observers, using data obtained from 1910 images (Sekanina and Larson, 1984), data from the Vega images (Sagdeev et al., 1986) and pre-perihelion photometry (Leibowitz and Brosch, 1986), have concluded that the rotation period of Halley is $P=52-53$ hrs. However the photometric observations of Millis and Schleicher (1986) and Williams et al., (1987) during 1986 March and May, indicate a double peaked light-curve with $P=7.4$ days. Sekanina (1987) has interpreted this light-curve, by assuming the nucleus is both rotating and precessing.

From Table 6, the duration of outbursts and their interval times vary from image to image, and no sequence or pattern can be found which includes all images. Only the first four images had prominent dust bands, with clear-cut dates. Considering these images, it can be seen that the duration of each outburst is 2 or 4 days. If the 4-day outbursts are two synchrone merged together then clearly the duration of these outbursts is $2 \pm 1/2$ days. It must be noted however, that dust grains are not ejected from the nucleus with zero relative velocity. There will exist some velocity dispersion, which is proportional to grain density and size. Such a dispersion may give rise to different broadening effects along the length of a synchrone. Considering the possibility of this effect and the absence of any clear duration pattern in Table 6, no comment can be made concerning the nuclear rotation period.

TABLE 6

Duration of Comet Halley Synchrones

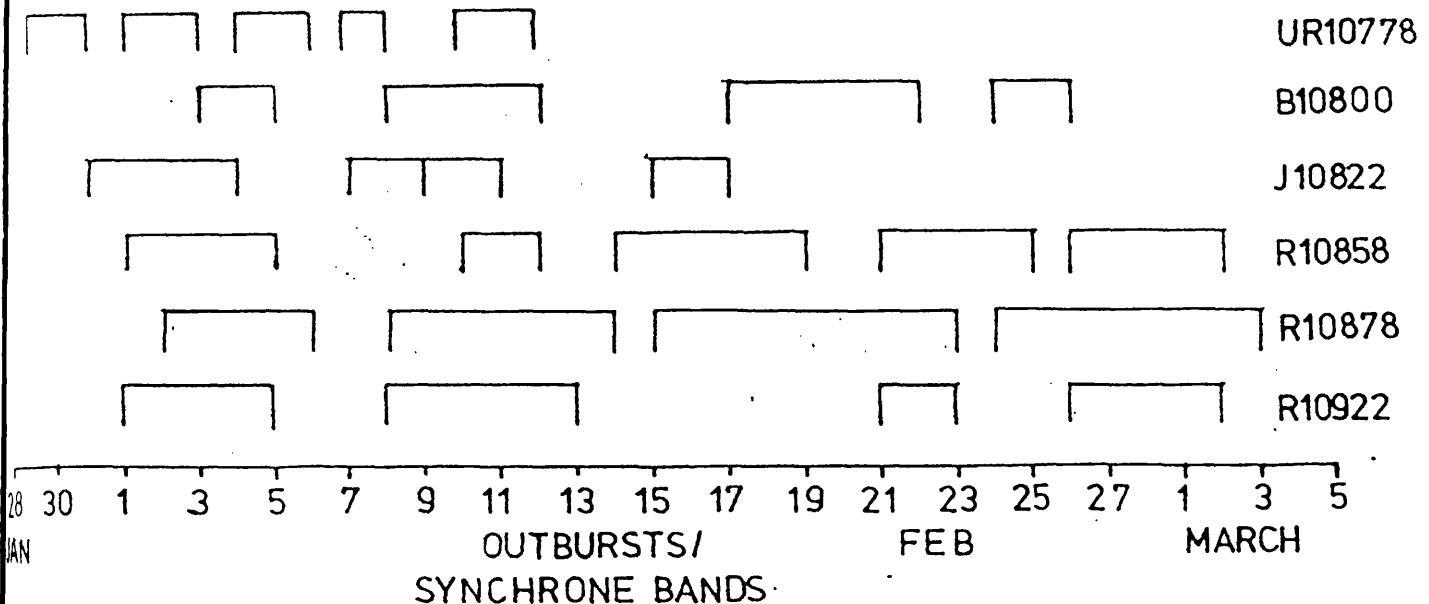
<u>Image</u>	<u>Dtn.</u>	<u>Int.</u>	<u>Image</u>	<u>Dtn.</u>	<u>Int.</u>	<u>Image</u>	<u>Dtn.</u>	<u>Int.</u>
UR10778	(days)		B10800	(days)		J10822	(days)	
Feb. 1-3	2	1	Feb. 3-5	2	3	Jan. 31-2	2	0
4-6	2	1	8-10	2	0	Feb. 2-4	2	3
7-8	1	2	10-12	2	5	7-9	2	0
10-12	2		17-22	5	2	9-11	2	4
			24-26	2		15-17	2	

<u>Image</u>	<u>Dtn.</u>	<u>Int.</u>	<u>Image</u>	<u>Dtn.</u>	<u>Int.</u>	<u>Image</u>	<u>Dtn.</u>	<u>Int.</u>
R10858	(days)		R10878	(days)		R10922	(days)	
Feb. 1-3	2	0	Feb. 2-6	4	2	Feb. 1-5	4	3
3-5	2	5	8-10	2	0	8-13	5	7
10-12	2	2	10-14	4	1	21-23	2	3
14-19	5	2	15-23	8	1	26-2	4	
21-25	4	1	24-3	7				
26-2	4							

Dtn. Duration/Width of the synchrones

Int. Interval between the end of one outburst and the beginning of the next.

Dtn. + Int. = Time between the start of one outburst and the start of the next.



KEY
 Outburst

Velocity of the Dust Grains - Dimensions of the Nucleus

From Finson-Probstein theory, if a dust tail can best be represented by a syndyne, then the width of the tail is directly related to the grain ejection velocity (see chapter 2.1 Fig.4). Only for the antitail, seen on February 22 can this be said to be true - the synchrones and syndynes are almost parallel to the tail. As an approximate calculation the width of the synchrone at its widest point is $\approx 54,000\text{km}$ and it corresponds to dust that has been emitted ≈ 60 days previously. Using the formula

$$\text{ejection velocity} = \frac{1/2 \text{ tail width at a point}}{\text{ejection time at that point}}$$

the ejection velocity $v_i = 5\text{ms}^{-1}$ which is small compared to the typical value of $v_i = 1\text{kms}^{-1}$ quoted by Finson and Probstein. Using the former velocity as an approximate escape velocity from the nucleus (assumed spherical with $\rho = 3\text{gcm}^{-3}$) the average diameter of the nucleus is $\approx 8\text{km}$.

The Antitail and the Sunward Spike

UR10778 was the first Schmidt image to depict the antitail, which unlike the sunward spike, could be explained as a line of sight effect. On February 22nd both sides of the antitail had sharp boundaries corresponding to December 4 and December 29. From Table 5 it can be seen that these dates correspond to a time when many outbursts were reported. Around the December 4 boundary, the older synchrones become very crowded together and so the date is only an estimate. December 4 need not necessarily be the "onset of activity time". It can only be interpreted as the onset time of dust particles that survived in sufficient quantities in space to be seen on the observation date. Such synchrone crowding can be seen on both the (M,N) and (ξ, η) plots (Fig.7b). Note how the older synchrones lag behind the comet's orbit. The antitail persisted until March 17th.

On November 21 and May 21 the Earth's position was such that its heliocentric longitude equalled that of the ascending and descending nodes of the comet, respectively. At such times the dust tail was viewed edge on. Thus for the five images, R11106, JB11120, R11135, R11202 and R11215 the fan shaped dust tail became viewed edge-on and observed as a narrow dust tail (Fig.11a). Finson-Probstein theory reveals synchrones and syndynes closely packed together (in both (M,N) and (ξ, η) co-ordinates, see Fig.12) although somewhat shifted in position with respect to the observed tail direction.

The sunward extension seen on R11060 now appears as a fully prominent sunward spike - not to be confused with the antitail seen earlier in February. The length of the dust tail decreased from $\approx 2 \times 10^7$ km (R11106) to $\approx 1 \times 10^7$ km (R11215). The

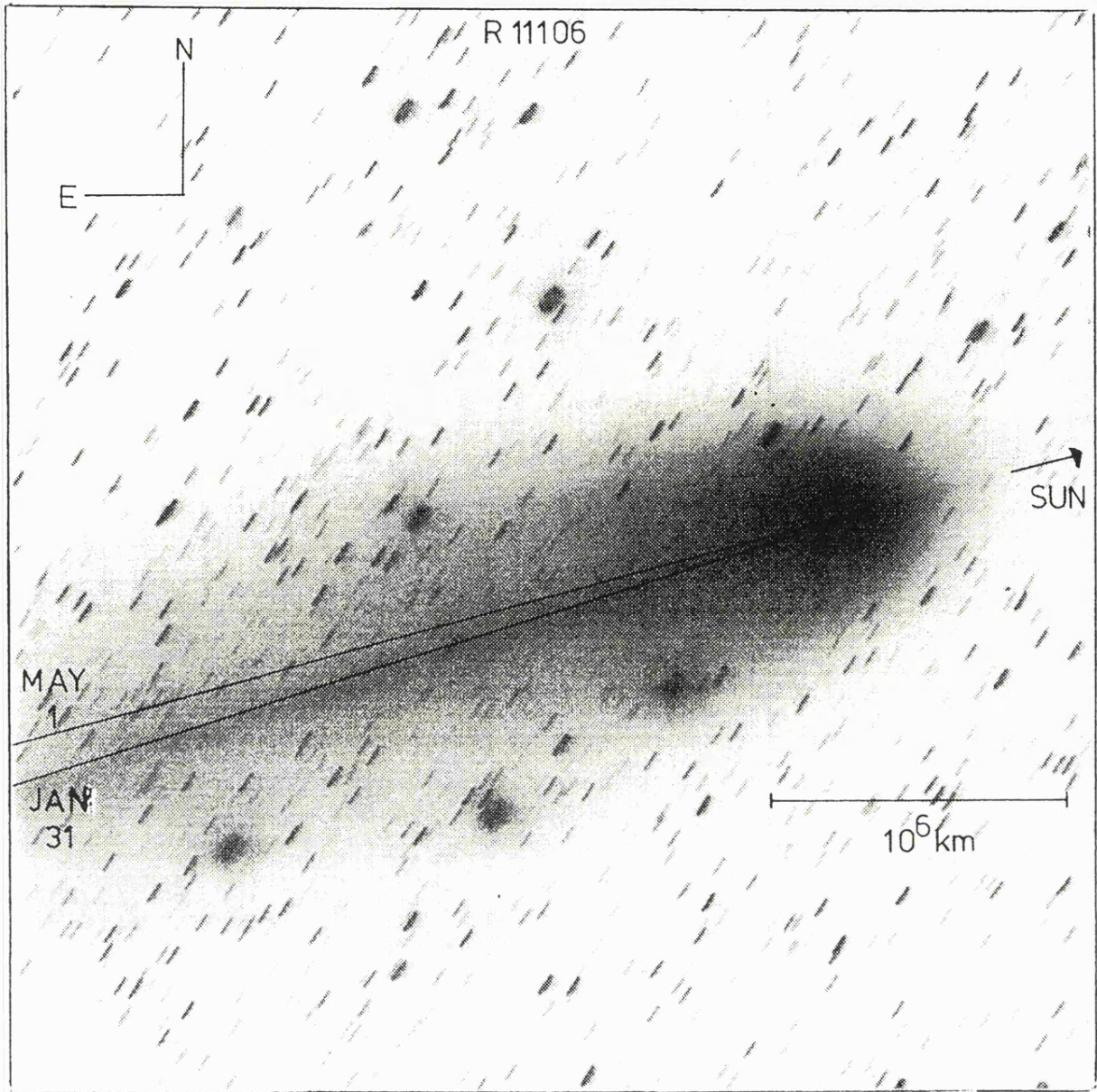


Fig. 11a. Schmidt image R11106. May 1 and Jan 31 denote the positions of two synchrotrons in the (M,N) plane. All synchrotrons lie very close together and are positioned on-top of the narrow dust tail. The sunward spike can just be seen on this photograph.

R11106

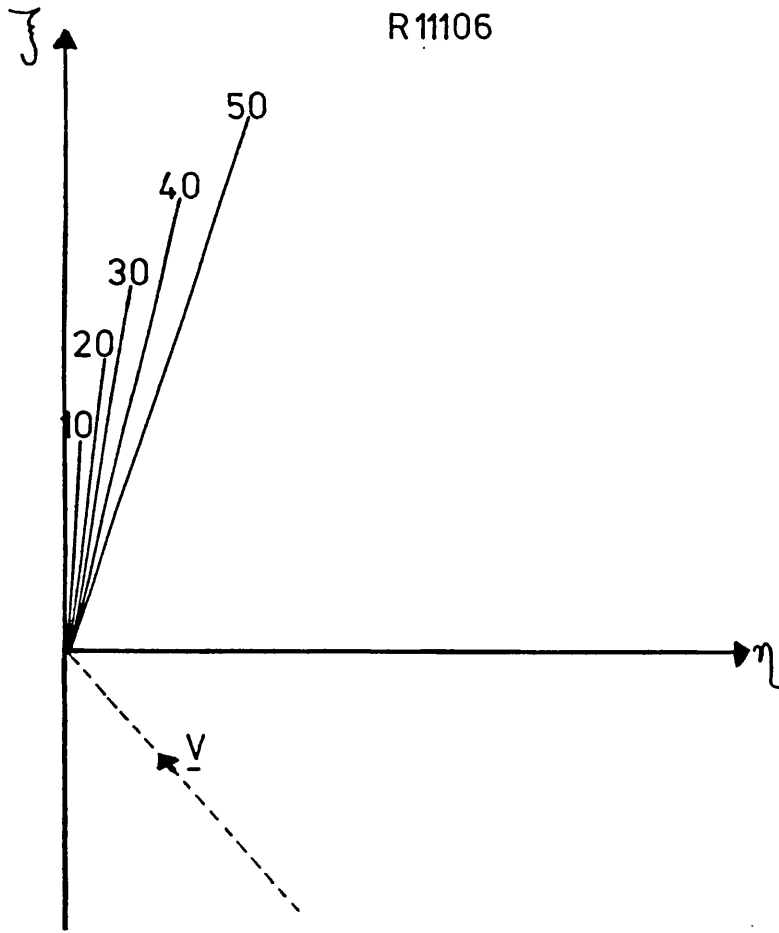


Fig.12 . Cometocentric co-ordinates of various synchrones. The synchrones are the loci of grains which have been emitted 10, 20, ... 50 days previous to the observation date (11/5/86). Note how the synchrones are very close together. The vector V denotes the motion of the nucleus in the (ξ, η) plane.

sunward spike is most prominent on R11106 and its length was $\approx 5 \times 10^5$ km. From the Schmidt images the spike appears directly opposite the dust tail and its appearance lasted for about 70 days. The Sun vector points West of the spike (R11106) then becomes almost parallel with the spike (JB11120 + R11135) and finally becomes North ($\approx 10^\circ$) of the spike (R11202 + R11215).

No variation in synchrone/syndyne values could produce the observed position of the sunward spike indicating that a different process was involved. Such a process would have to produce dust with high sunward ejection velocities and low radiation pressure values i.e. the spike could be composed of very small grains (see Fig.4). Sekanina (1986b) has concluded that the spike is composed of dielectric or slightly absorbing grains with $a \ll 0.1 \mu\text{m}$. He further stated that such grains could only be detected when the Earth is located in or very near the plane of their concentration. In fact, the predicted date for the Earth's transit across the equatorial plane of Halley's nucleus was April 15, quite close to the first Schmidt recorded appearance of the sunward spike on April 19.

Comet Arend-Roland also displayed a "sunward spike" although this turned out to be an antitail which could be represented by very old synchrone. Such synchrone when projected onto the sky plane arbitrarily pointed towards the Sun (Sekanina, 1974).

The Range of Dust Grain Sizes

For a constant grain density Finson-Probstein theory tells us that the force due to radiation pressure is smaller for large grains than smaller sized grains. Larger grains will therefore stay closer to the nucleus. As can be seen in Fig.13 syndynes (loci of equally sized particles) cross over synchrones, the loci of smaller grains being further out from the nucleus. The length of a synchrone is therefore indicative of the range of grain sizes. The true extent of each synchrone can only be found by scanning along its length (using Starlink software) and thus determine the position at which the sky background dominates. This was tried on several images, but it was evident that all dust bands (excluding the antitail) extended beyond the edge of the plates. The antitail seen on the computerised images was not sharp enough to have its "length" measured.

Although the true range of sizes could not be found, limited syndyne analysis was performed on the image UR10778 which had widely spaced and well defined dust bands.

UR10778 - 1986 February 22

The range of syndynes considered, dealt with those grains which move in orbits for which $F_{\text{grav}} > F_{\text{rad}}$ i.e. elliptical and hyperbolic orbits, for which μ values lie in the range 0.001 to 0.999. Most syndynes cross over the synchrones, but for the very old synchrones the syndynes are parallel (Fig.13). The antitail was superimposed with $\mu=0.995$ to $\mu=0.980$ syndynes with $\mu=0.99$ providing the best fit with regards to position and length (the length of the antitail was judged by eye).

If we choose $Q_{\text{pr}} = 1$ and the density of the grains to be 3gcm^{-3} (magnetite grains have $\rho \approx 5\text{gcm}^{-3}$, silicate grains $\rho =$

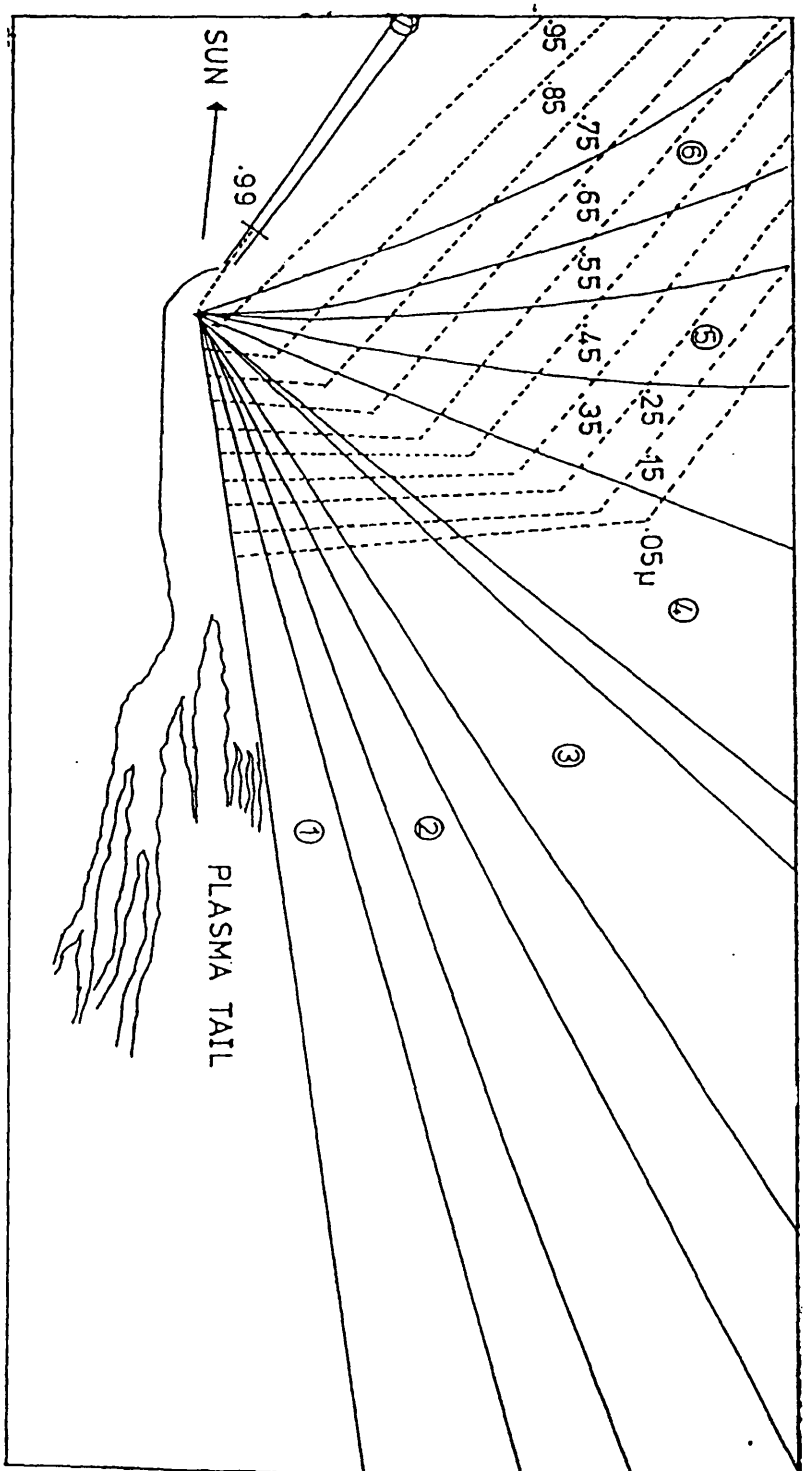


Fig.13 A schematic representation of Comet Halley (UR10778) showing the main dust bands 1 to 7. Dotted lines represent syndynes $\mu = 0.05$ to 0.95 . Note how dust bands 1-4 extend much further than $\mu = 0.05$ possibly indicating grains which are not bound to the solar system.

All syndynes become approximately parallel to synchroves at early emission dates. The approximate length of the antitail (denoted by cross-line) is well matched with the length of the syndyne $\mu = 0.99$ (for an emission time of 70 days previous).

2gcm^{-3} and icy grains $\rho \approx 1\text{gcm}^{-3}$) then from $1-\mu = \text{Constant} \times Q_{pr}/(\rho d)$, the diameter of the grains is $\approx 40\mu\text{m}$. Clearly the antitail represents large grains which have been ejected from the nucleus at least 2 months prior to perihelion.

The January 25-28 and 29-31 synchrones which extend beyond the plate boundaries, are crossed by many syndynes ranging from $\mu=0.5$ to $\mu=0.05$ i.e. grain diameters 0.8 to $0.4\mu\text{m}$. Such small μ values (0.05, or $\beta=0.95$) could only relate to materials such as magnetite (see Fig.4). Olivine cannot attain such low values.

If the range of sizes is the same for each outburst then it can be assumed that there are submicron and larger sizes being ejected each time. The largest dust grain detected by the DIDSY experiment on-board the Giotto spacecraft (McDonnell et al., 1986) had a mass of $\approx 1.1 \times 10^{-6} \text{kg}$ ($900\mu\text{m}$ for $\rho = 3000\text{kgm}^{-3}$). So due to lack of detection at visible wavelengths, the largest sizes are not being detected.

At the other end of the size range there are several problems. The remaining four synchrone bands extend further than the $\mu=0.001$ syndyne. This occurred for the other images too. There are several explanations.

1. The dust tail could be composed of very small and/or low density grains which have μ values < 0 i.e. convex hyperbolic orbits where the grains experience a net repulsive force and are removed from the Solar System.

2. The grains could be composed of ice embedded with small rocky deposits. As the ice vaporizes the grains fragment into smaller particles which then appear much further out from the nucleus than expected. From the inner coma images of Halley (chapter 3.6) there is no evidence to support the vaporization

theory. Perhaps instead rocky grains are fragmenting (due to collisions) and so producing a new population of small grains.

3. Another explanation is in the theory itself. Finson-Probstein theory should only be applied to comets with no plasma tails i.e. where there is no consideration of dust-plasma drag forces. The four synchrone bands are somewhat nearer the plasma tail than the others. The theory also applies to uniform isotropic emission from the nucleus. Quite clearly from the Giotto images this is not the case. The presence of small and large jets indicates a non-uniform surface which could be precessing. However the theory is adequate enough to show such variable emission by the presence of strong dust bands.

4. Comparison with the theoretical results by Ozeki (1986) indicate programming differences, although Sekanina's synchrone dates (1986a) are very close to this author's results.

The first explanation does appear to be the more probable. Sekanina's (1986c) analysis of the 1986 images has revealed repulsive accelerations, β up to 2.5 in the main tail (i.e. $\mu = -1.5$) indicating very small unbound particles ($0.15\mu\text{m}$) or grains of a "fluffy/crumby" nature. Hayward et al. (1987) and Smirnov et al. (1986) both agree on the latter nature of the grains and suggest that the dust density is $\rho < 1\text{gcm}^{-3}$. Assuming such a low density, the minimum size of the grains in the antitail will be $\approx 120\mu\text{m}$.

Burns et al. (1979) have confirmed that small iron, magnetite or graphite grains $\approx 0.1\mu\text{m}$ in size have $F_{\text{rad}} > F_{\text{grav}}$ i.e. β values > 1 . Considering the infrared spectral analysis of Comet Halley in chapter 5, where magnetite material is

shown to be a strong candidate for cometary grains, it is clear that the range of β values considered in this work has to be extended to include those grains on orbits for which $F_{rad} > F_{grav}$.

Dust Grain Orbits - Contribution to the Zodiacal Cloud

For a dust grain to become part of the Zodiacal Cloud, it must enter into an elliptical circumsolar orbit i.e. dust grains which have $e < 1$ and β values in the range $0 < \beta < 1$. What proportion of the grains leaving Halley's nucleus are on such orbits? Finson-Probstein analysis reveals that the smaller the grain (or the smaller the density) the higher the eccentricity of the resulting dust orbit i.e. the more hyperbolic the orbit. This is justifiable: the lighter the grain, the greater the radiation pressure force and the further it will be propelled away from the nucleus. For all β values, the eccentricity increased up to a maximum at perihelion and then decreased during post-perihelion (Table 3c).

For $\beta = 0.05$ dust grains assumed hyperbolic orbits during ≈ 96 days pre and post-perihelion. Outside of this range they assumed eccentric orbits. The onset of sublimation has been given as September 1984 (528 days prior to perihelion). If it is assumed that the "turn off" time is an equal number of days post-perihelion, then during Halley's active period $\approx 80\%$ of the dust grains with $\beta = 0.05$ assumed eccentric orbits. Likewise, similar calculations for $\beta = 0.10$ indicate 55% leave on eccentric orbits and for $\beta = 0.15$ only 20% have eccentric orbits. β values greater than this do not have eccentric orbits during the active ejection time.

In summary, grains larger than $\approx 8\mu\text{m}$ ($\rho = 1\text{gcm}^{-3}$) or $\approx 3\mu\text{m}$ ($\rho = 3\text{gcm}^{-3}$) are expected to go into elliptical orbits and contribute to the Zodiacal Light. For example, such grains are found in the antitail seen during February. Grains smaller than these values will go into hyperbolic orbits and leave the solar system. It is assumed that once on these hyperbolic

orbits they will remain so, i.e. there is no perturbation from the Poynting-Robertson effect to change the orbits from hyperbolic to elliptical. Numerous particles have been found to be travelling on hyperbolic orbits. For example, the β meteoroids exist in interplanetary space (Zook + Berg, 1975, Berg + Grun, 1973). The Pioneer spacecraft 8 + 9, found more particles streaming away from the Sun than into it. Recent studies (Sandford, 1986) of the Doppler shifts found from the Zodiacal Light show that many scattering particles have orbital velocities greater than the velocity of escape, thus opening the question as to whether grains on hyperbolic orbits do contribute, for some fraction of time, to the Zodiacal Light.

2.4 Conclusion

Finson-Probstein theory is quite complex, both with respect to its mathematical background and its applied concepts. Because of such, it has only previously been applied by a limited number of authors. However the approach taken in this work and the application of the computer programs have proven very successful in the analysis of the large scale Halley images. The theory accurately predicts the changing form of the dust tail as the line of sight changes during 1985/1986. The multi-structured dust tail seen during February and March, is interpreted as a series of "synchrone bands". These bands represent major outburst times which are of ≈ 2 days duration. A 2.2day or 7.4day rotation period could not be found from the UK Schmidt results.

The observed grain size distribution varies from submicron to micron sizes, in the main tail. The upper limit is extended to $120\mu\text{m}$ ($\rho=1\text{gcm}^{-3}$) for the antitail. The application of Finson-Probstein theory, further suggests the presence of very small (<submicron) grains, or grains of very low densities ($<1\text{gcm}^{-3}$). Such grains exist on orbits for which $F_{\text{rad}} > F_{\text{grav}}$ i.e. non-permanent members of the Solar System, on convex hyperbolic orbits. The presence of such grains has been confirmed for P/Halley by Sekanina (1986b).

Analysis of the grain orbits shows that grains larger than $\approx 10\mu\text{m}$ ($\rho=1\text{gcm}^{-3}$) are ejected from the nucleus into elliptical (and thus bound) orbits, thus contributing to the Zodiacal Cloud.

CHAPTER 3

DUST FEATURES IN THE INNER AND OUTER COMA

3.1 The UK Schmidt Telescope and The COSMOS Measuring Machine

The 1.2m UK Schmidt telescope employs 356x356mm² glass plates which are loaded at the prime focus. The plates can be coated with different emulsions which together with the properties of various filters, can restrict the responsivity of the resulting image to a certain wavelength range. All comets were tracked continuously using a newly devised computer controlled offset guidance system. The plates were digitised on the COSMOS measuring machine at the Royal Observatory Edinburgh.

COSMOS is an automatic high speed densitometer which uses a light beam for a number of raster scans across the photographic plate. The light beam produces a certain size microspot on the plate - 8, 16 or 32 μ m. A light sensitive diode detects the amount of light transmitted through the plate at each spot position. A VAX computer stores all density values in a 2 dimensional array. This array is compressed to form a 512x512 pixel, computer image. At the South-East corner of each Schmidt plate, a 16-step calibration wedge is projected through the filter used and onto the plate. The illumination of the step wedge is of the same exposure as the photographic plate. The calibration is placed onto a clear part of the plate to avoid contamination by nearby stars and also to ensure that the calibration is well determined to a level below that of the lowest sky density on the plate. The relative intensity between each step in the wedge is known and by determining the mean density value across each step, a density versus relative intensity curve can be drawn. Using this relation the whole of the required image can be converted to relative intensity units. If, for example, a

standard star of known magnitude appears on the plate then the relative intensity to absolute intensity (in standard flux units) conversion can be calculated and applied to the image, i.e. an absolute zero point can be applied to the calibration curve.

Some interference filters (loaned from the Anglo Australian Observatory) used with the Schmidt, are not of the same size as the plates. A second, smaller sized filter is therefore used, of similar transmission properties, to project a step wedge onto the South-East corner of the plate.

Processing CCD Images

Unlike Schmidt photographic images which can saturate due to the limit of the emulsion/filter combination, a CCD, which collects photons directly from distant objects, does not suffer from such an effect.

Before exposure, a CCD is raised to a level of $60e^-$ in each pixel to enable negative fluctuations to be recorded. This is the BIAS current. If the CCD is exposed for more than 20 mins., then stray electrons falling into the individual potential wells begin to make a significant contribution, this is termed the DARK current. At the side of each image a strip of pixels is usually left unexposed. The mean level of this intensity (due to BIAS and DARK) is subtracted from the image and the strips are removed. For each filter used, a "flat-fielded" image is recorded, i.e. an exposure, of for example, the inside of the dome taken through each filter. This is done to record the individual and overall response of the pixels. The flat-fielded image is smoothed to distinguish the underlying gross responsivity. This is then divided into the original flat-fielded image to show the net pixel

response. The final image is then divided into the cometary images to remove all pixel response.

3.2 CCD and UK Schmidt Images of Comets Crommelin

Giacobini-Zinner and Halley.

Comet Crommelin

Although Comet Crommelin is a well recognised comet (Period=27.4yrs), it had not been studied in detail, prior to its selection as a trial-run object for the Comet Halley campaign. At the previous apparition it was simply described as a fuzzy nebulosity with a short ($1/2^\circ$) tail (for further details see Vsekhsvyatskii 1964; Festou 1984). Observations on 1984 January 3 showed the comet to be 2 arcmin across with an integrated magnitude of 10.5mag. By mid-February a 3 arc-minute coma had developed. The comet reached its maximum brightness of 7.5mag. in early March. On March 3, a weak plasma tail (at PA 85°) and a weak tail-like feature (at PA 30° on a red plate) was reported (Romanishin and Sitko, 1984). By mid-March a tail was reported, 3 arcmins. long at PA 45° . By early April the comet had faded to around 10mag. (M.J. Hendrie, personal communication). During the observational period various gaseous species were identified via spectra, such as C_2 , NH_2 , CN , C_3 and CH (Spinrad et al., 1984a, Larson, 1984).

Many UK Schmidt plates of Comet Crommelin were taken, using narrow- and broad-band filters, but only two (representing the distribution of cometary dust) will be discussed here. See Tables 7 and 8 for details of all plates/images. For Comet Crommelin the central cometary condensation is sharply defined, of the order of 1-2 arcsecs. similar to the seeing disc. With a $16\mu m$ COSMOS spot size, an $8 \times 8 mm^2$ area produced a 512×512 pixel frame with 1 pixel \approx 1 arcsec. This size frame was large enough to contain the entire

TABLE 7

Observational Summary of Cometary Images

<u>Plate/Image</u>	<u>Mid-Expos.</u>	<u>Expos.</u>	<u>Emulsion/Filter</u>	<u>Effective</u>	<u>Date</u>
	<u>(GMT, h m s)</u>	<u>(mins)</u>	<u>Combination</u>	<u>Width(nm)</u>	
<u>P/Crommelin</u>					
IF9155	11 49 58	30	IIaf + AA0643	638-648	30/3/84
R9176	10 56 01	30	IIaf + RG630	630-690	4/4/84
<u>P/Giacobini-Zinner</u>					
5881	4 05 56	10	HeI star filter	586-590	11/9/85
10839*	5 57 58	10	Z	1077-1090	"
R	4 12 59	3.3	R	570-720	12/9/85
5881/2	4 48 02	13	HeI	586-590	"
JB10484	18 07 00	30	IIao + GG395	395-500	22/9/85
<u>P/Halley</u>					
IF10573	9 58 00	40	IIaf + AA0643	638-648	5/12/85
IF10621	11 17 00	50	IIaf + AA0643	638-648	19/12/85
R10620	11 02 00	1	IIaf + RG630	630-690	19/12/85
R10777	19 03 00	0.5	IIaf + RG630	630-690	21/2/85

* This filter represents scattered emission at 1 μ m but unfortunately the image was small and noisy.

TABLE 8

Orbital Data For Comets Crommelin, Giacobini-Zinner and Halley

<u>Plate/Image</u>	<u>Date</u>	<u>RA</u>	<u>Dec</u>	<u>R</u>	<u>Δ</u>
		<u>(h m)</u>	<u>(° ')</u>	<u>(AU)</u>	<u>(AU)</u>
<u>P/Crommelin</u>					
IF9155	30/3/84	5 05	-16 05	1.03	0.80
R9176	4/4/84	5 37	-17 24	1.09	0.81
<u>P/Giacobini-Zinner</u>					
5881	11/9/85	5 54	+23 56	1.03	0.47
10839	"	"	"	"	"
R	12/9/85	5 57	+22 31	"	"
5881/2	"	"	"	"	"
10484	22/9/85	6 29	+ 8 56	1.06	0.50
<u>P/Halley</u>					
IF10573	5/12/85	0 29	+20 40	1.43	0.67
IF10621	19/12/85	22 59	+ 1 57	1.21	0.90
R10620	19/12/85	"	"	"	"
R10777	21/2/85	20 43	-13 29	0.64	1.42

comet image down to the sky background. For the R9176 plate, the photographic densities were converted to relative intensities via the method previously described. The IF9155 plate did not have a calibration wedge and so an average response curve was introduced.

Giacobini-Zinner

Giacobini-Zinner is a short period comet in an elliptical, prograde orbit with $P=6.42$ yrs. It is a relatively young, small comet and exhibits irregular brightness variations over intervals of a few days. One of its distinctive features is a narrow ion tail which develops near 1.7AU and reaches a length of $\approx 10^6$ km. The Earth's passage through the Giacobinid meteor stream, produces a spectacular meteor display. The shortness of the meteor tracks has been interpreted as evidence that the meteoroids have very low densities $\approx 100\text{kgm}^{-3}$ (Jacchia, 1980). Unlike Comet Crommelin, which is considered an old comet with a stable orbit, Giacobini-Zinner is noted for its peculiar non-gravitational effects.

The comet was recovered on April 3 1984 (Djorgovski et al. 1984) with a stellar appearance. By mid-August 1985, the comet was reported to be elongated East-West and spectra showed the presence of $\text{CN}, \text{C}_2, \text{C}_3 + \text{CH}$ (Cochran + Barker, 1985). Many tail lengths and position angles were reported throughout July and August e.g. tail 21' at PA 270° (Cavagna, 1985). Using narrow-band filters, Rees and Wallis (1985) observed an ion tail several thousand km long.

Giacobini-Zinner was observed with the 1m JKT at La Palma during 1985 September 10-16. The observation run was partly carried out as a dry run for the future Comet Halley observations, but also as a backup ground-based programme for

the ICE (International Comet Explorer) mission which encountered Giacobini-Zinner on 1985 September 11. The standard IHW filters could not be used in conjunction with the mounted CCD (GEC chip) and so a suitable selection of stellar filters were used. The telescope tracked the comet for each exposure. The seeing was $\approx 1''$ and the CCD pixel size was $0.3''$. The UK Schmidt telescope obtained several large scale JB (blue filter) photographic plates of the comet a few days after the CCD exposures. The final resolution of the Schmidt images is $4''$ per pixel. Tables ⁺⁸7_^ list those images which best represent the dust grain continuum.

Comet Halley

This well known comet has been described in detail in Chapter 2. The UK Schmidt telescope was involved with an astrometric programme, determining accurate near nuclear positions for the Giotto spacecraft encounter. Although the exposure times were very short (6 seconds), some of these images showed inner coma features. Parabolic dust hoods or envelopes could clearly be seen on many plates. Another set of Comet Halley plates used narrow-band interference filters to monitor the water production rate as a function of heliocentric distance. One of these filters, the "IF" filter/emulsion combination represents the dust continuum. A small number of astrometric and "IF" type images are presented here.

3.3 Intensity Contours - Their Shape and Symmetry

Figs.14,15+16 show relative intensity contour plots for most of the images described in Table 7. All images have been smoothed using a 5 point Gaussian profile and sky background has been subtracted. The contours have been drawn such that they represent various fractions of the central maximum intensity.

Images of Comet Crommelin were taken through several different gas and dust filters and although it showed neither a plasma tail nor a multistructured dust tail, the contoured gas images (with underlying continuum) were generally more circular, while the dust-only images, for example R9176, were appreciably elongated, especially at lower intensity levels. It was noticed that the direction of elongation for the R9176 image contours changed from inner to outer contours. R9176 was contoured by thresholding (i.e. rejecting all pixels below a certain intensity level) at a series of levels up to a normalised peak intensity level. In this way Starlink software was able to calculate a best-fit ellipse for each contour and compute the position angles indicated by the major axes of these ellipses. The results for the central regions of the image are probably unreliable owing to the near-circularity of the contours and saturation effects, whilst those for the outer contours are unreliable due to the faintness of the image. The results for the remaining contours are found in Table 9. The IF9155 image was not processed in this way, its contours were considered too noisy.

The Giacobini-Zinner images depicted the comet with an elongated coma, and again there is no clear separation between dust and plasma tails. All images taken through various gas

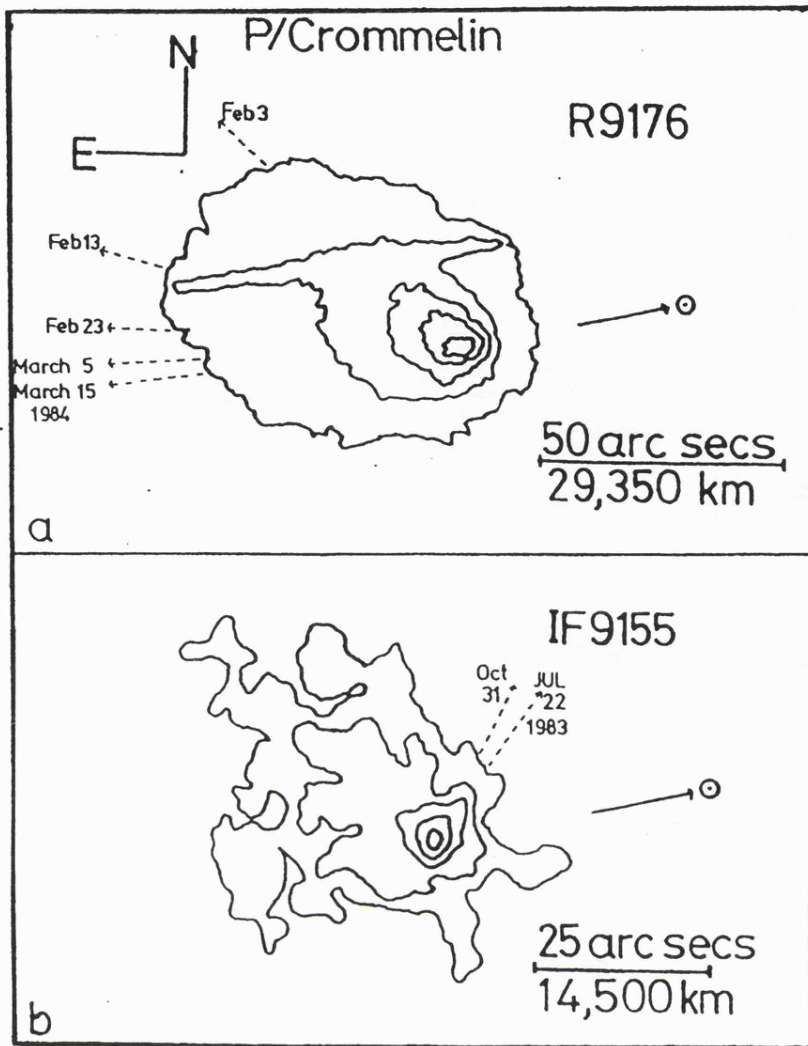
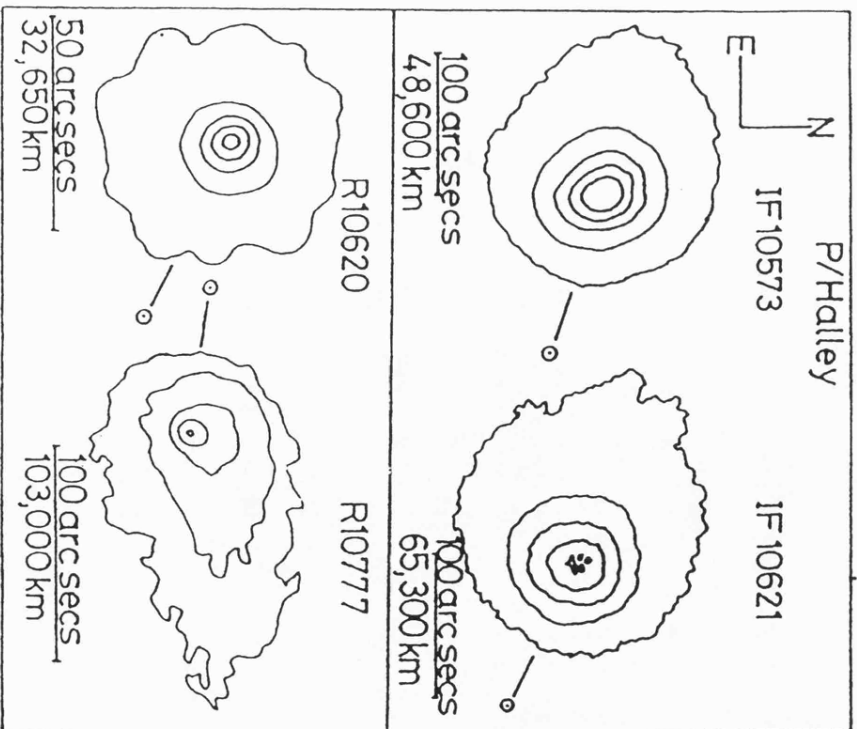
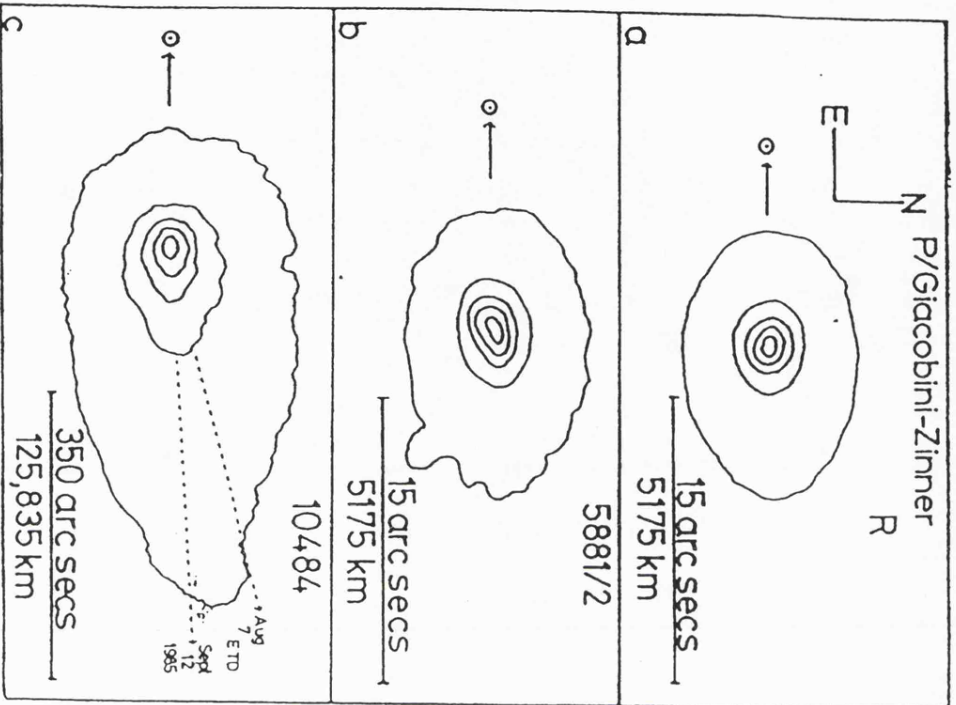


Fig.14 Intensity contour plots of P/Crommelin.

All images have been smoothed and background subtracted. The contours represent various fractions of the central maximum intensities: 0.1, 0.3, 0.5, 0.7 and 0.9. The extension in the 0.3 contour for R9176 is due to a star trail. The dotted lines represent dust synchrones (see text for details).



Figs. 15+16. Intensity contour plots of P/Halley and P/Giacobini-Zinner. All images have been smoothed and background subtracted. The contours represent various fractions of the central maximum intensities. The dotted lines represent dust synchroes (see text for details).

Figs. 15a+b (Giacobini-Zinner) are CCD images while Fig. 15c is a Schmidt image. Figs. 16a,b,c + d (Halley) are also Schmidt images, a + b are astrometric and c + d are narrow-band images.

TABLE 9

Position Angles* of the Major Axes
for the Contours Ellipses of Comets

Crommelin¹, Giacobini-Zinner² and Halley³

<u>Rel.</u>	<u>R91761</u>	<u>5881/2²</u>	<u>10484²</u>	<u>R²</u>	<u>IF10573³</u>	<u>R10777³</u>	<u>R10777³</u>
<u>Int.</u>							<u>(s.m.a.)*</u>
10	79°	268°	303°	271°	64°		
20	83	275	317	270	41	284	74036km
30	81	280	315	268	29	287	42766
40	65	284	296	264	26	296	25915
50	59	289	293	262	26	329	16604
60	58	289	296	261	23	357	10939
70	58		358	253	24	355	7189
80			283	254	22	316	4388
90					29	360	2060

+ These angles represent the tail/extension end of each contour.

* semi-major axis

Rel. Int. Relative Intensity Level

IF9155, IF10621 and R10620 contours were primarily circular.

Some intensity levels have been omitted due to noise/incorrect processing.

and dust CCD filters were remarkably alike. Fig.15 shows contour plots for the continuum images, R and 5881/2, and also the Schmidt image JB10484. Again, best fit ellipses were calculated.

Itoh (1985) reported that Comet Halley experienced two major outbursts on 1985 December 19 and 19.83. He indicated that these outbursts were the result of two sources - a weak and a strong jet. The Schmidt image IF10621 (December 19) did record a jet feature, but it was not apparent from the contours, which were generally circular. Another image IF10573 was included as a comparison, representing the comet at a more quiescent state. Two astrometric images were considered, R10777 and R10620. R10777 was taken on 1986 February 21, when the comet was post-perihelion and very active. Large scale images show the comet to have a wide synchrone band which corresponds to outbursts between February 15-26 (see Chapter 2.3). R10620 depicts the comet at a pre-perihelion stage (December 19), but there is no indication of the above mentioned jet feature on either the original image or the contoured image.

Discussion

Apart from R10620 and IF10621 which had near-circular contours, rotation of contours is apparent for the remaining images (see Table 9). The effect varies from slight rotation for JB10484 (Giacobini-Zinner) to quite pronounced for R10777 (Halley). That such an effect exists suggests that there is a systematic change in the photometric axis of each image, from the central condensation outwards. However the scale of the rotation does not match that seen for P/Arend-Rigaux (Chapter 5.2). What causes such a rotation and why do we see it on some

images and not others?

Storrs et al (1986) studied contours of Comet Iras-Araki-Alcock (1983d) from high resolution CCD images. They assumed that the "swinging round of contours" was due to a hot spot on the nucleus passing the sub-solar point or close to it. The extent of each contour elongation (measured from the nucleus), and the amount that each contour rotates can give information about the velocity of the dust providing the spin period is known, using the simple formula,

$$\theta = \left(\frac{w}{v} \right) \cdot r$$

where θ and r are measured from a reference point, w is the angular velocity of the rotating nucleus and v is the outflow velocity. Projection effects would obviously complicate the situation. If the values of r and θ , deduced from the contours, represent a non-linear function, then the plane of the contoured image could be highly inclined to the line of sight.

In Chapter 5 it is suggested that the rotation of contours for Arend-Rigaux resulted from the product of an outburst, which appeared to originate at a position angle of 55° , and a short rotation period. The size and extent of the Arend-Rigaux image suggests that the outburst was not a directed jet but rather continuous emission from the sunlit hemisphere. Obviously a comet with a very fast or very slow rotation period would not suffer from such a "rotation of contours" effect. Taking the outburst position as the reference point $r=0, \theta=0$, (r, θ) values were measured for each contour. The rotation period of Arend-Rigaux is not well known, but may be in the range 6.76hrs (Jewitt and Meech, 1985)

to 13.5hrs (A'Hearn, 1985). For either limits, the (r,θ) values represented a non-linear function indicating a large projection effect or possibly errors in the measurements. The true mean value of the outflow velocity would probably be at the lower end of the calculated velocity range $0.9-7 \text{ kms}^{-1}$.

Comet Halley's rotation period is believed to be at least a few days. It therefore raises the question as to the contour rotation seen on R10777. The other Halley images show some rotation, but mostly in the outer contours. Their image scale is such that they represent only the inner portion of the R10777 image. It is suspected that the effect of radiation pressure on the dust is responsible for the contour rotation in R10777. (In fact, the outer contours lie along the the expected tail direction (ETD) for this date). It is interesting to note that the position angle of the original active region on the nuclear surface (i.e. finding θ for $a \rightarrow 0$, where "a" is the semi-major axis of a contoured ellipse) was found to be 90° i.e. the subsolar point, and confirms that emission is from the sunlit hemisphere.

The rotation periods of Giacobini-Zinner and Crommelin are not well known. Estimates for the former have been published by Sekanina (1985), $P=1.66\text{hrs}$, and Leibowitz and Brosch (1986), $P=9.5\text{hrs}$. From Table 9 it can be seen that the direction of rotation for the 5881/2 image and the R image are opposite. Many other CCD images taken on the same night have their innermost contours pointing in different directions. Although CCD images do not suffer from saturation effects, it is therefore possible that the elongation and rotation effects are due to seeing, tracking or blurring. The outer

contours of the Crommelin and Giacobini-Zinner Schmidt images have probably been affected by radiation pressure.

3.4 Near Nuclear Features - Examination of the Fountain Model

The coma of a comet may be considered to undergo three separate dust related processes. The first is the dust-gas coupling which occurs only up to a small region from the nucleus. From this process the terminal velocity (after de-coupling) is important. The dust grains emitted in the solar direction will travel with this terminal velocity until the force due to solar radiation pressure overcomes the total energy of the particle (second process). At such a point the dust velocity is zero. Finally, Finson-Probstein theory deals with the structure of the forming dust tail as the grains are pushed back by radiation pressure. The assumptions made at the beginning of this third process (i.e. the dust grains are emitted from a point with zero initial relative velocity) are only very generalised as the orbits of the grains during process two maybe more complex.

An inspection of the astrometric plates reveals inner coma features which are parabolic in shape. The origin of such features lies with the orbits of dust grains associated with process two. Eddington (1910) developed the "Fountain Model" to explain the orbits of such dust grains. Mendis et al. (1985) explain the theory as follows.

Consider the orbits of dust grains that are emitted in the sunward direction. The only force acting on the dust grains is that due to radiation pressure. The constant retardation is g where,

$$g = \frac{3 Q_{pr} S}{4 c r_s^2 a \rho_d}$$

r_s = heliocentric distance

Q_{pr} = scattering efficiency for radiation pressure

c = speed of light

S = solar constant

ρ_d = dust grain density

a = grain radius

For a cometocentric frame (ξ, η) , the equation of motion for a grain with initial velocity, ejected at an angle α_i to the solar direction $(-\xi)$ is given by,

$$\xi = -v_i t \cos \alpha_i + 1/2gt^2 \quad \eta = v_i t \sin \alpha_i$$

which represents a parabola. All parabolas associated with different angles of projection are enveloped by a bounding paraboloid whose equation is,

$$\eta^2 = 4a(\xi + \alpha) \text{ where } \alpha = v_i^2/2g$$

The apex is at $\xi = -\alpha$ and is the distance travelled towards the Sun by a grain which was initially projected in the Solar direction.

Sekanina and Larson (1984) have used the basis of this theory to study 1910 photos of Comet Halley. After using enhancement techniques to reveal near nuclear features, they noticed a number of jet features which appeared to unwind from the nuclear condensation. Following these jets, it was seen that they evolved into a type of parabolic hood. They attributed the process to continual emission of dust from discrete sources on the sunlit hemisphere of a rotating nucleus. For example, for a source on the equatorial plane (which coincides with the orbital plane) its evolution depends on the nuclear spin period. If the unwinding jet features are short lived and the resulting parabolic hood is symmetrical, then the spin period is short (few hours say). But for $P \approx$ few days the unwinding of the jets is more apparent and an asymmetrical envelope is formed. A more recent

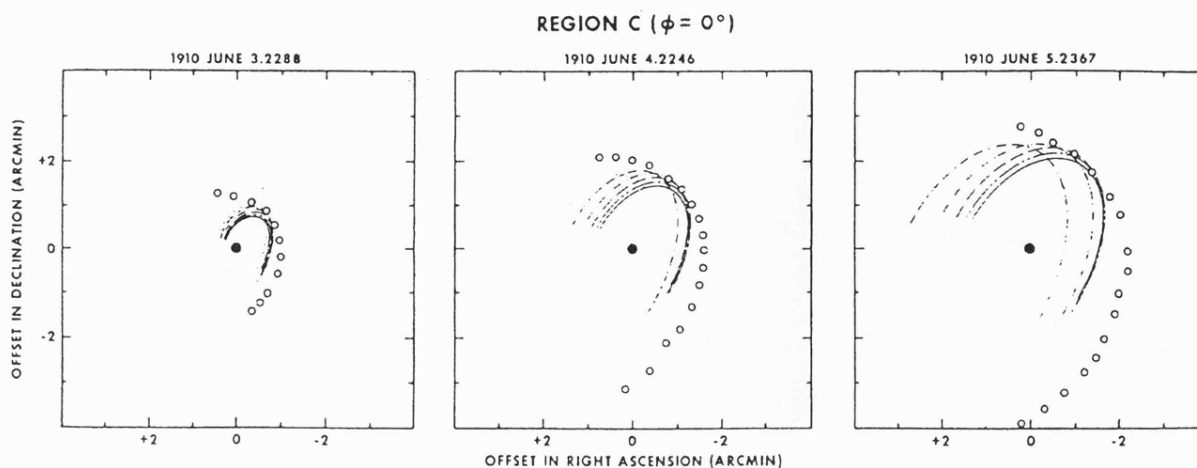


Fig.17 Comparison of the measured boundaries of evolving spiral jets with the model of continuous dust ejection from discrete emission regions on the rotating nuclear surface. Plots shown are for latitude zero degrees. The nucleus is shown as a solid circle and the measured parabola as open circles. The sets of theoretical curves represent particles subjected to different acceleration β . See Sekanina & Larson, 1984 for details.

study of asymmetrical envelopes by Horanyi + Mendis, (1985), attributes the askew parabolas to the effect of electromagnetic forces (resulting from the electric field in the solar wind) acting on small ($<1\mu\text{m}$) charged grains.

Sekanina and Larson's theory is complicated by several parameters which must be taken into consideration, e.g. longitude and latitude of the hot spot, spin period P , obliquity and argument of equator with respect to the orbital plane, the range of emission times, the number of active areas and the velocity distribution as a function of the acceleration β . Sekanina and Larson (1984) used the positions and motions of the unwinding jets to place constraints on many of the parameters above. With a set of fixed parameters, they determined the positions of a set of curves, each marking the boundary of a group of grains with equal acceleration (β) values. The quasi-parabolic envelopes observed from the images are then compared to these sets of curves (Fig.17).

Each envelope is composed of the boundaries of the individual β curves. ^{Smaller} grains ejected with higher velocities are subjected to higher radiation pressure accelerations and vice-versa. As time increases the heavier particles will move forward to dominate the boundary. Therefore the values of β , responsible for the boundary, change with time.

Various enhancement techniques have failed to show clearly such unwinding jets in the inner coma. This could be due to the fact that we are not seeing close enough to the nuclear region or that the enhancement programs are lacking. The parameters determined above may well be inconsistent, now that there is the possibility of a precessing nucleus which would alter how we would see such jets and envelopes.

The photographs shown in Fig.18 show two of these astrometric images, R10779 and R10785. Quite clearly the envelopes are asymmetrical, in particular for R10779, indicating a rotation period of a least a few days.

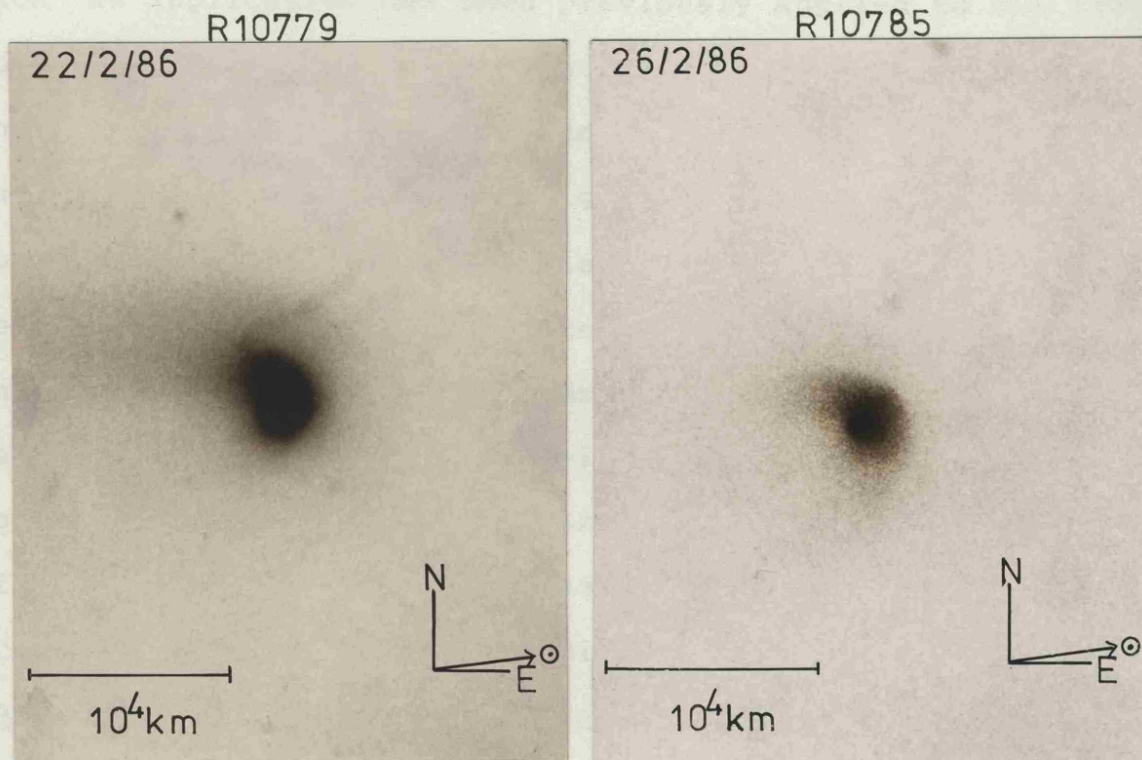


Fig.18a+b Two photographs showing the astrometric images R10779 and R10785 respectively.

3.5 Application of Finson-Probstein Theory

A Finson-Probstein analysis (1968), which is usually used on well-developed dust tails was attempted to explain the orientation of the Crommelin and Giacobini-Zinner contours. Such an application has been previously applied to the IF9155 Comet Crommelin image by Eaton and Zarnecki(1985): they found that the elongation of the contours did not match the expected tail direction for typical grain sizes (order of μm) and concluded that anisotropic emission was taking place. It must be noted, however, that the scale of the IF9155 image is such that the outer contours represent dust which has only been released a couple of hours previously. Finson-Probstein theory does not work well on such short time scales. The application of Finson-Probstein theory was therefore restricted to R9176 (Crommelin) and JB10484 (Giacobini-Zinner).

JB10484 Giacobini-Zinner

Apart from the scattered radiation by dust grains, the JB filter/emulsion combination transmits radiation due to gaseous emissions such as CN , C_2 , C_3 and most importantly CO^+ . Is the extension we see on the JB image a plasma or dust tail or a combination of both? The contours deviate from the antisolar direction by only a few degrees, which can be expected for a plasma tail. However the plasma tail had been reported as very narrow and greatly extended, it was therefore assumed that the extension in the JB10484 image was due to dust grains. A Finson-Probstein analysis revealed that at such a small image scale the syndynes and synchrones lie very close together. "ETD" marked on Fig.15c marks the positions of the synchrones, 1985 August 7 and 1985 September 12. Their curvature and direction match the extension direction. However caution

must be exercised when putting specific synchrone dates on the tail as the scale of the image suggests dust grains which have been emitted only a few days previous to the image date, (assuming $v=1\text{kms}^{-1}$).

Telesco et al. (1986) analysed a "jet feature" on a $10.8\mu\text{m}$ thermal infrared map of Giacobini-Zinner taken on 1985 August 4.4. The feature was identified as a dust tail syndyne ($\beta = 0.001$, $\mu = 0.999$) associated with grains $100\mu\text{m}$ in size, with initial ejection velocities $<3\text{ms}^{-1}$. The low dust grain albedo, and the calculated syndyne inferred large fluffy grains. The experiments (Kissel et al., 1986) carried out on the Giotto spacecraft indicated the presence of abundant CHON particles in the coma of Comet Halley. Apart from gases which are the product of direct sublimation from the nucleus, these particles are potential sources of the daughter and parent molecules (Hanner, 1985). The presence of an anti-sunward C_2 tail for Giacobini-Zinner was discovered by Wallis et al., (In Prep.). Are some of the C_2 molecules being produced via sputtering/sublimation of dust grains? Schleicher (1985) studied spectral line strengths of Giacobini-Zinner and concluded that the comet was depleted in C_2 and C_3 and speculated that it could be hidden in the form of dust grains. Previous observers e.g. Jacchia (1980) found that the Draconid meteors (associated with the Giacobini-Zinner) were composed of a "soft" material with very low densities and which were easily vaporized.

P/Crommelin

R9176

At such a small scale the syndynes lie close together (Fig.14a). The synchrone for Comet Crommelin, however, are

fairly well spaced. Its outer contour suggests dust emitted between 1984 February 3 and February 13. Again considering the image scale caution must be exercised considering the precise dates.

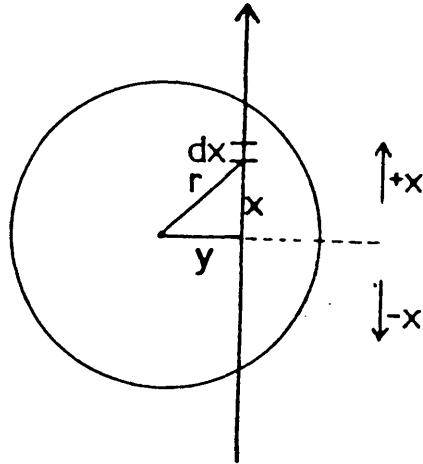
IF9155

Although this image is noisy (Fig.14b), it had been noted that there appears to be an extension of contours at p.a. 330° .

This could be noise or some form of jet indicating anisotropic emission. A test of various synchrone dates puts this extension as being due to grains that are emitted previously to November 1983 (the synchrones lie very close together at such early dates), although it is doubtful whether Crommelin was active at such an early date. A look at such early synchrones on a (ξ, η) plot, shows that they are approaching the direction opposite to the orbital motion of the comet. This orbital lagging is to be expected for such grains. Is this feature of the same nature as that seen by Telesco et al. (1986) for Giacobini-Zinner? While the Crommelin feature lies in a sunward direction the Giacobini-Zinner feature is directly opposite the Sun. At such a small image scale the syndynes run very close together and no size estimate could be put on such old synchrones. Zarnecki et al. (1984) found that the dust production of Comet Crommelin was quite low compared to other short period comets, but that its dust temperature was high indicating the presence of hot absorbing grains ($<10\mu\text{m}$). However Hanner (1984) studied the visual and infrared spectra of Crommelin and concluded that the dust grains were both unusually large and dark (albedo 0.05). Could this jet feature be old large dust grains which are lagging behind the orbit? An infrared map of Crommelin would be very useful in resolving this question.

3.6 Dust Distribution and Intensity Profiles

For an optically thin coma we can assume that the three dimensional dust density decreases as a power law, where, density $\propto R^{-\lambda}$.



The surface brightness is the integral along the line of sight,

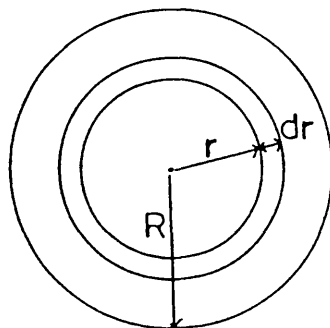
$$\begin{aligned} \text{Surface brightness} &= 2 \int_0^{\infty} \bar{r}^{-\lambda} dx = 2 \int_0^{\infty} (x^2 + y^2)^{-\lambda/2} dx \\ &= 2 \int_0^{\infty} \left(\frac{x^2}{y^2} + 1 \right)^{-\lambda/2} y^{-\lambda} dx \end{aligned}$$

y is a constant for a given line of sight so the above can be expressed as,

$$\begin{aligned} &= 2 \int_0^{\infty} \left(\frac{x^2}{y^2} + 1 \right)^{-\lambda/2} d\left(\frac{x}{y}\right) y^{-\lambda+1} \\ &= 2 \int_0^{\infty} (u^2 + 1)^{-\lambda/2} du y^{-\lambda+1} \quad \text{where } x^2/y^2 = u^2 \end{aligned}$$

and so the surface brightness is $\propto y^{-\lambda+1}$.

Consider again a 3-D dust coma where the flux in a small annulus is dF .



Now,

$$dF = 2\pi r dr k' / r \quad \text{or } F = 2k' \pi R \text{ i.e. } F \propto R.$$

Column density \propto flux

Flux \propto surface brightness $\propto R$

So the dust density is $\propto 1/r^2$. This is consistent with a model in which the dust is blown out from the nucleus in a continuous, uniform manner i.e. it satisfies the continuity equation. Deviation of the intensity fall-off profiles from $I \propto r^{-1}$ are indicative of nonuniformity in dust production or outflow, i.e. acceleration of grains or sublimation of volatiles (Storrs et al., 1986). If the grains are accelerating then the dust density falls off faster than r^{-2} . If the grains are decelerating (perhaps due to radiation pressure, if the grains are moving in the sunward direction) then the reverse occurs. Accretion of gaseous material by a grain is not thought to exist due to the gas being thin and the grain hot. Sublimation or breaking up of grains could occur and lead to an increase in surface area and a brightness fall-off slower than r^{-1} . The grain break-up should decrease with increasing distance from the Sun, leading to a uniform "bend" in the brightness profile. Storrs et al. (1986) studied the dust distribution in the inner coma of Comet IRAS-Araki-Alcock (1983d) and concluded that the brightness fall-off could not be fitted by a single power law. Estimates from the linear portions of the profiles indicated a fall-off slower than r^{-1} and they attributed this to fragmentation of the grains.

Baum and Kreidl (1985) have used dust profiles to prove that volatiles in dust grains sublimate as the grains flow away from the nucleus. Such a sublimation causes the grains to

"fade" due to the decrease of their X-sections, their albedos or both. From studies of Comet Gun-Westphal they found that intensity profile slopes had steeper than $1/r$ gradients and that the rate of fading decreased with increasing heliocentric distance.

There are several ways to determine the gradient of a dust profile. One obvious way is to scan across the nucleus in any direction, split the profile in two, and plot two graphs showing $\log(\text{relative counts})$ versus $\log(\text{pixel distance})$. The gradient of each plot is γ . This method was tested, but found to give very noisy graphs. The method described below (and subsequently used) produced fairly smooth profiles from which gradients could be easily found.

A simple Starlink routine integrates the counts within a computerised aperture which is centred on the brightest pixel in the image. A plot of magnitude ($= -2.5 \log \text{ counts}$) versus $\log(\text{aperture radius})$ has a gradient "n".

$$\text{magnitude } m = c_1 \log(\text{aperture area}) + c_2$$

$$\text{or } m = c_1 \log(\pi R^2) + c_2$$

$$\text{or } m = n \log R + c_3 \quad \dots 1)$$

Now, let the brightness within the aperture be B, where $m = -2.5 \log B$, rearranging 1) gives,

$$B = c_4 R^{(-n/2.5)} + c_5 \quad \dots 2)$$

The brightness may also be expressed in terms of the surface brightness, $S(r)$ which is the brightness at a point.

$$B = \int_0^R S(r) 2\pi r dr \quad \text{or} \quad \frac{dB}{dr} = 2\pi R S(r) = \frac{-n}{2.5} c_4 r^{(-n/2.5-1)}$$

$$\text{therefore } S(R) = \frac{-n}{2\pi 2.5} R^{(-n/2.5-2)}$$

$$\text{or } \gamma = \left(\frac{-n - 2}{2.5} \right)$$

As dB/dr is positive then n is taken to be negative.

This method, which averages out the coma structure, was applied to all the images in Table 8. Additionally it was applied to P/Arend-Rigaux (see Chapter 5) and to the far-infrared photometry obtained for Comet Halley with the 1.9m SAAO during April 1986 (Chapter 4). Also included was the multi-aperture photometry performed on Comet Halley on 1986 March 6 with the 24" SSO telescope, Australia, in conjunction with a CCD. These latter results are absolute R magnitudes obtained through a range of apertures from 12.8" to 110.1" on 1986 March 6.8 ($r=0.799\text{AU}$, $\Delta=1.138\text{AU}$, observations performed by S.F.Green and D.W.Hughes). The standard stars used for calibration were SA0227940, SA0230002 and SA0163520. Average extinction curves were assumed. The profiles are found in Fig.19 and the resulting γ values are found in Table 10.

It is immediately apparent that the gradients of the Schmidt images are very low compared to those of the CCD. It is possible that the gaseous contamination of a filter could lead to the alteration of a profile, considering the exponential decay and production of parent and daughter molecules. For example, GZ10484 is highly contaminated by various emissions but its gradient is equal to that of IF9155 whose transmission is restricted to dust scattering only. A closer inspection of the original density plates revealed that most images did suffer some form of saturation in the nuclear region. This saturated area would be present in all aperture sizes and thus lead to a smoothing effect on the profiles.

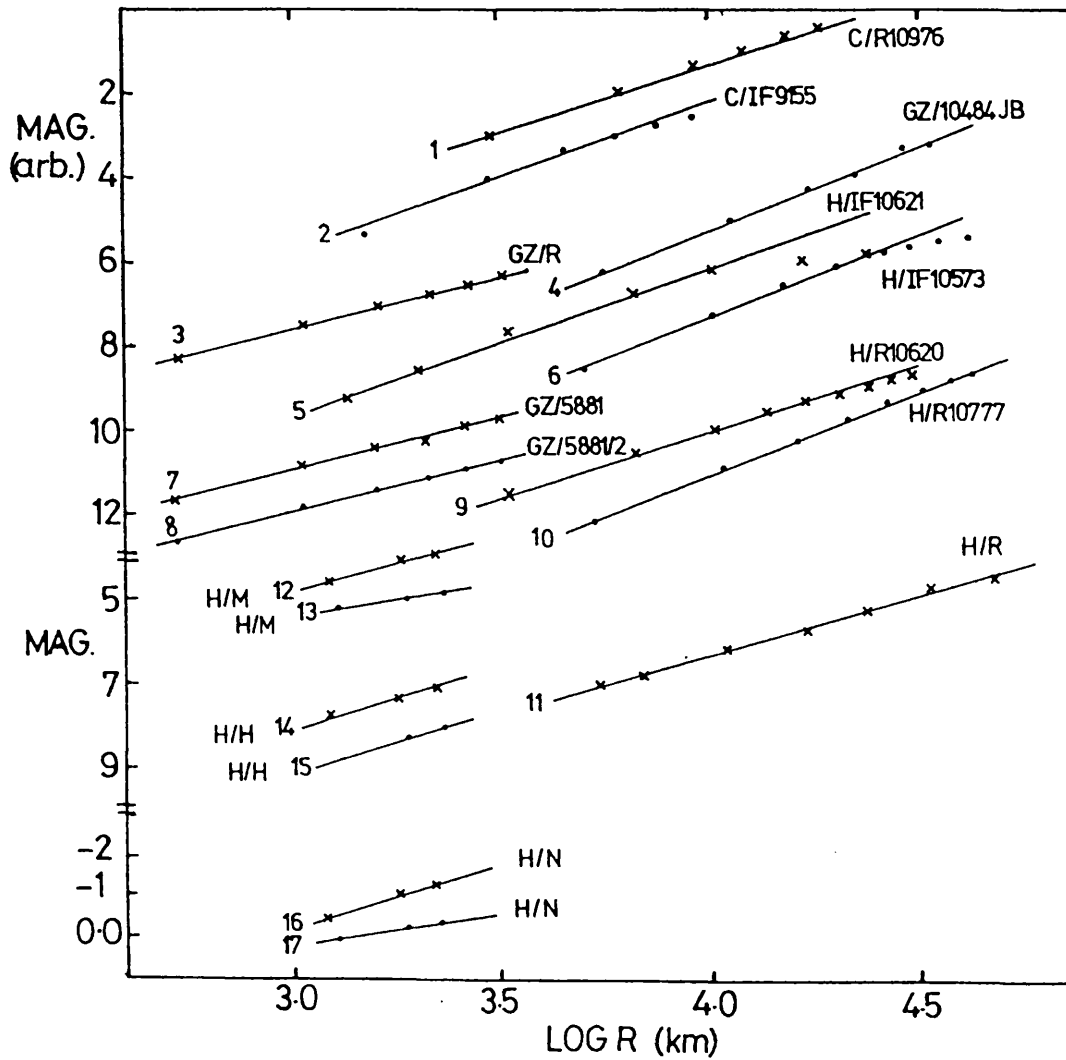


Fig.19 Plot of magnitude versus log(distance from the nucleus) for P/Crommelin, P/Halley and P/Giacobini-Zinner.

1+2 Crommelin Schmidt plates

3,7+8 Giacobini-Zinner CCD images

4 Giacobini-Zinner Schmidt image

5+6 Halley narrow-band Schmidt images

9+10 Halley astrometric Schmidt images

11 Halley R-band visible photometry

12-17 Halley infrared photometry filters M,H,N

Profiles 11-17 are in true magnitude units.

TABLE 10

Gradients (- γ) from Dust Continuum Profiles

<u>P/Crommelin</u>	γ^1	γ^2	<u>P/Halley</u>	γ^1	γ^2
IF9155	0.55	1.20	R10620	0.70	1.30
R9176	0.70	1.20	R10777	0.60	0.80
<u>P/G-Zinner</u>			M(20/4/86)	1.00	
R	1.05		M(21/4/86)	1.35	
5881	1.05		H(20/4/86)	0.75	
5881/2	1.00		H(21/4/86)	0.80	
JB10484	0.55	0.95	N(20/4/86)	0.85	
<u>P/Halley</u>			N(21/4/86)	1.40	
IF10573	0.45	1.30	R(24"SSO)	0.85	
IF10621	0.55	2.20			

Errors are typically ± 0.1

¹ Gradients found via multi-aperture method

² Gradients found from Schmidt images via annuli method

Following Baum's method, using annuli (centered on the brightest area), the previous multi-aperture data was inter-subtracted to produce the mean count per pixel in an annulus whose thickness was 2.5 or 5 pixels. Plotting $\log(\text{mean count per pixel})$ versus $\log(R)$ (where for two aperture sizes, R refers to the largest radius) gives a direct surface brightness profile. New values of γ are also listed in Table 10. Within the errors, Crommelin, Giacobini-Zinner and Halley (R10777, R10620 and IF10573) images have their gradient values close to 1. The activity of Halley during 1986 February 21 does not seem to have affected its gradient. Could the jet feature noticed on R10621 be responsible for such a large gradient $\gamma=2.2$? R10620, taken only a few minutes earlier shows no such gradient, unless the effects of the jet are more apparent in the outer coma. Such a high gradient would suggest rapid acceleration of the grains from perhaps such a jet outburst.

Deviations from the straight line fits do occur especially for IF10621, IF10573 and R10620 and are due to the aperture not being completely filled by the comet at large apertures. From the gradients, comets Giacobini-Zinner and Crommelin are seen to have uniform dust outflow, although many profiles taken at various heliocentric distances would have to be processed before any conclusion regarding uniformity of the nuclei (i.e. no hot spots causing jets etc.), could be announced. It is interesting to note that a CCD image recording Giacobini-Zinner through a V filter (C_2 emission) gave a gradient value of $\gamma = 0.9$, while photometry using B and V filters on the 24" telescope gave gradient values of $\gamma = 0.8$ and 0.9 respectively. Considering the JB10484 gradient as

well, is the method of determining dust profiles too crude to reveal gaseous contaminations or is the underlying continuum dominating the profiles? The method cannot be too crude, however, to confirm the change in physical appearance of Comet Halley between 1986 April 20-21. Although the change is not too pronounced in the H filter (scattered light), the average gradient change between the M and N filters is 0.45. The new average dust density $1/r^{2.45}$ indicates a slower fall-off caused by a non-uniform dust production at the nucleus, leading to a diffuse comet.

It is interesting to note that the DIDSY experiment onboard the Giotto spacecraft recorded flux profiles (i.e. number density profiles) as it passed through Halley's coma. On average, the density profiles followed an inverse square law close to the nucleus, but there were exceptions. Larger particles did not follow such a law and jet streams had a much steeper fall-off. During pre-encounter, all density levels had lower than $1/R^2$ fall-offs corresponding to an approach from the unlit side. A mild transition marked the crossing of the terminator to the sunlit side i.e. no sharp dawn enhancement could be seen.

In this data set, any deviation along the profiles can be explained by aperture effects. No effects of sublimation or vaporization can be detected. No effect of vaporization can be seen for Giacobini-Zinner to confirm the presence of large fluffy volatile grains.

3.6 Conclusion

Unlike P/Halley, P/Arend-Rigaux, P/Crommelin and P/Giacobini-Zinner did not display separate plasma and dust tails on the UK Schmidt plates. The majority of the dust

images, indicated a "swinging round" of the contours i.e. there was a systematic change in the photometric axis of each image from the central condensation outwards. The size of the effect varied from a slight rotation for Giacobini-Zinner to quite pronounced for Halley and Arend-Rigaux. For Arend-Rigaux, such an effect is due to a combination of rapid rotation and directed emission from the sunlit hemisphere. For Halley (and probably for Crommelin and Giacobini-Zinner) the effect is due to radiation pressure.

The application of the "Fountain Model" (Mendis et al., 1985) to analyse the near-nuclear orbits of dust grains is complicated by many factors, the most important being the suspected precession effect. Enhancement of the P/Halley astrometric images reveals the presence of "parabolic hoods". Such hoods are suspected of representing the loci, or envelopes, of the different grain orbits. Limited analysis reveals that due to the asymmetrical nature of these hoods the rotation period of Halley is at least a few days.

The application of Finson-Probstein theory to the large-scale images of Crommelin and Giacobini-Zinner, agrees with the general form and curvature of the dust tails. In both cases the tails are comprised of dust that has been emitted up to two months previously. There is a possibility that a jet feature, seen on the IF9155 Crommelin image, represents a series of old synchrones i.e. dust grains which have been emitted up to 4 months previously.

Caution must be exercised, when examining intensity profiles which have been obtained by averaging over the whole cometary image. The method of using annuli (Baum + Kreidl, 1984) is useful in overcoming the problems of saturation

effects. For Crommelin, Giacobini-Zinner and Halley, most of the profile gradients follow an $I \propto r^{-1}$ law, indicating uniform dust grain outflow. However, intensity profiles, from filters which allowed additional transmissions from gaseous emissions, gave similar gradient values indicating that a more precise method of gradient determination is required.

CHAPTER 4

THERMAL SPECTRA

MIE THEORY AND DUST TEMPERATURES

4.1 Properties of Dust Grains -

Scattered and Thermal Radiation

A cometary spectrum is composed of two types of continuum; one is due to the scattering of radiation by dust grains and the second is an infrared continuum caused by thermal emission from dust grains.

General Properties of Thermal Emission (Ney, 1982)

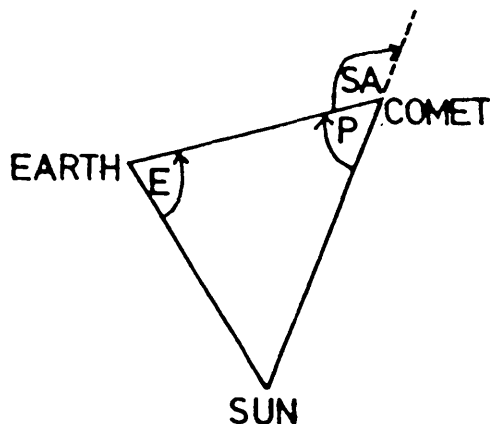
1. When fitting a standard blackbody spectrum to the thermal emission, the colour temperature is normally higher than that expected for a true blackbody at the same heliocentric distance. This temperature excess has been attributed to small grains which cannot radiate efficiently at wavelengths comparable to their size. All size grains cannot radiate efficiently at wavelengths $\lambda > 10 \times$ their radius.

2. A silicate emission feature is sometimes present at $10\mu\text{m}$. Such a feature indicates the presence of small grains ($a < 0.5\mu\text{m}$). Small grains do not contribute significantly to either the observed brightness or to the total mass loss from the nucleus. It was first proposed by Maas et al. (1970) that the dust grains consisted of a mixture of silicates and a black material, with silicates in the excess and carbonaceous chondrite a strong candidate for the black material. The antitail of Comet Kohoutek (which showed no temperature excess in its spectrum) was observed near perihelion (Ney, 1974) and while the silicate feature was strong in the coma and tail it was absent in the antitail. This could indicate the presence of non-silicates or large particles of the same average composition as the coma. In order for the silicate feature to appear, the grains must be of the order of 1 optical depth or less in a single grain (i.e. $a < 5\mu\text{m}$).

3. When the energy spectrum is modelled to a blackbody curve, $(\lambda F_{\lambda})_{\max}$ is proportional to the total energy under the Planck function. Since $(\lambda F_{\lambda})_{\max \text{ IR}}$ for thermal emission gives the total energy radiated, this is also the total energy absorbed. A fit to the short-wavelength data gives the energy reflected. The grain albedo γ is thus given by,

$$\left(\frac{\gamma}{1-\gamma} \right) = \left(\frac{(\lambda F_{\lambda})_{\max \text{ VIS}}}{(\lambda F_{\lambda})_{\max \text{ IR}}} \right)$$

and is dependent on the scattering angle A , where (phase angle, P + scattering angle, SA) = 180° . The thermal spectrum is not dependent on scattering angle as the dust grains are considered isotropic at these wavelengths.



Forward scattering can lead to higher albedos and bright comae. Very large albedos can indicate the presence of a bright, cold component such as icy grains. At 1AU, pure ice may have a lifetime of years, but slightly dirty ice has only a lifetime of hours. These icy grains would be large and would have a range of only a few hundred km from the nucleus except during an outburst. The ice absorption features at 1.5 and $2\mu\text{m}$ (in the scattered spectrum) have never been detected (Hanner, 1983). Observations at a variety of scattering angles give a phase function compatible with dirty dielectric grains.

4. Mass loss rates may be determined by calculations based on optical scattering (where mass loss is proportional to the size distribution and the scattering phase function). In the infrared, for particles smaller than a few μm , the infrared luminosity measures the mass of the grains independent of particle size. (App.3).

5. The thermal spectrum may overlap the scattered spectrum between 1-3 μm . This contamination is heliocentric distance dependent.

6. The colour of the scattered radiation (for which grain sizes are comparable to the radiation wavelength) depends on grain size, composition, surface roughness and scattering angle (Campins and Hanner, 1982). Scattered spectra (devoid of gaseous emissions) which are redder than solar colours indicate the presence of an absorbing material in the dust grain matrix e.g. magnetite is an absorbing material present in meteorites. The lack of Rayleigh scattering implies characteristic grain sizes comparable to the wavelength, i.e. $\approx 1\mu\text{m}$. Blue colours at large scattering angles are a consequence of strong backscattering in silicate spheres. But again silicate spheres with a small amount of absorption material in the matrix would tend to make the colours redder.

Hanner (1981) has compared cometary JHK colours (as a function of scattering angle) with various colours computed by Mie theory (see next section) for a variety of grain compositions. Variations in grain size, scattering angle and the inclusion of various fractions of impurities in the grains leads to difficulties in associating a particular cometary colour to one specific type of grain.

Direct observations of icy grains (which have blue

colours) are difficult as they are expected to rapidly sublime at $r < 2\text{AU}$. This could be the reason why ice absorption bands are difficult to detect.

4.2 Mie Theory

While Finson-Probstein theory reveals information concerning a large range in dust grain sizes, Mie theory is restricted to grains of radii 0.1-20 μ m.

From the general properties we can say that there are two dust components: hot absorbing grains and silicate grains. Scattering properties of grains were first investigated by Mie in 1908, and has subsequently been explored by various authors, such as Eaton (1984), for a variety of grain shapes. It is likely that Brownlee particles are the most representative of cometary dust grain morphology. However closer inspection reveals complicated "cluster of grapes" morphologies for which no single scattering function could apply. The application of Mie theory (for a single sphere) would have to represent the gross scattering properties of a large number of grains. Eaton (1984) discusses the extent to which scattering by laboratory grains deviates from that predicted by Mie theory. A full analysis is given by van de Hulst (1957).

For a particle of radius "a" in a field of plane polarised radiation of wavelength λ , the scattering properties can be determined in terms of the parameters,

$$x = \frac{2\pi a}{\lambda} \quad m = n - ik$$

where "m" is the complex index of refraction, "n" and "k" are the refractive and absorptive indices respectively. For example, a typical expression for a magnetite grain is $m=2.5-0.6i$. The radiation interacting with the particle is either absorbed in the grain or is scattered (reflected externally, internally or refracted) out of the beam. The total amount of light removed from the beam, Q_{ext} is given by,

$$Q_{ext} = Q_{abs} + Q_{sca}$$

where Q is a dimensionless efficiency factor. An efficiency factor of 1 means that the particle removes from the incident beam an amount of radiation equivalent to its cross sectional area and

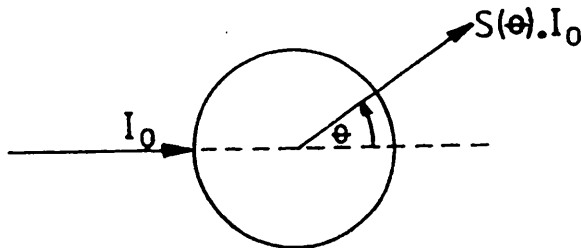
Cross section for absorption = (Efficiency factor x Geometrical cross sectional area of the particle.)

The albedo of the grain A , is defined as

$$A = \frac{\text{Total energy scattered in all directions}}{\text{Total energy removed from the incident beam}}$$

$$A = Q_{sca} / Q_{ext}$$

The light scattered by the particle in any given direction is altered from its original intensity, I_0 by the phase function $S(\theta)$ (per unit solid angle), θ is the scattering angle.



For a sphere the scattering phase function $S(\theta)$ is derived from the two complex functions $S_1(\theta)$ and $S_2(\theta)$ which describe the scattering of radiation with electric fields perpendicular and parallel with the plane of scattering.

$$S(\theta) = \frac{1}{2k^2} (|S_1(\theta)|^2 + |S_2(\theta)|^2)$$

where k is the wave number = $2\pi/\lambda$.

Q_{sca} is found by integrating the phase function over all directions. Q_{ext} is found from the phase function for $\theta = 0$

degrees and both of these efficiencies can be expressed as functions of the Mie coefficients a_n and b_n . The efficiency for radiation pressure Q_{pr} , which determines the dynamical evolution of dust tails can also be expressed in these coefficients as well as in the following form,

$$Q_{pr} = Q_{ext} - \langle \cos\theta \rangle Q_{sca}$$

where $\langle \cos\theta \rangle Q_{sca}$ represents the mean of $\cos\theta$ weighted by the phase function $S(\theta)$ over all solid angles, for a given substance and particle size, by integrating over all wavelengths. Q_{pr} is therefore a mean value, from which $1-\mu$ can be determined. In fact Q_{pr} varies with particle size and density (see Fig.3a). Note that small particles do not interact with the solar radiation for wavelengths considerably larger than their size.

4.3 The Application of Mie Theory to Thermal Spectra

The index of refraction, m is proportional to the nature of the material, the wavelength of interest (0.3 to 30 μ m) and the temperature. What type of material are cometary grains composed of?

Brownlee particles are known to be extraterrestrial because of solar wind-implanted noble gases. They are black fluffy/crumbly grains and most grains are conglomerates of submicron particles. Most grains have high porosities and their compositions are similar to primitive meteorites (types CI or CM). The grains are thus composed of iron-magnesium silicates, nickel-rich sulphides and organic material. There are also rare embedded crystals of enstatite and olivine, and very rare grains of metals (Eaton, 1984). The CI and CM meteorites belong to the carbonaceous chondrite class. These type of meteorites are considered to be the most primitive (i.e. undifferentiated),

Chondrites are so called because of the presence of chondrules, which are spherical aggregates of olivine and/or pyroxene. The chondrite meteorites do not have such high porosities as the Brownlee particles, thus suggesting that the latter originate in cometary nuclei where the "gaps" are filled with ice. The grains that comprise the Zodiacal Cloud are of two types a) Those that are porous with anhydrous minerals such as olivine and pyroxene and b) Those that are compact with layer lattice silicates. The presence of two such different types has given further thought to the question as to whether both asteroids and comets contribute to this cloud of material.

The composition of cometary dust (presumed primitive) is

not definitely known so substances are chosen which can closely model the scattering properties of the dust, e.g. magnetite, to model dark absorbing grains and olivine to account for the silicate emission feature.

Olivine $(\text{Mg,Fe})_2\text{SiO}_4$ or $(\text{Mg,Fe})\text{SiO}_4$

The refractive index of pure olivine has essentially a zero absorption index k , between $0.35 < \lambda < 5 \mu\text{m}$ i.e. the material is a transparent dielectric which absorbs little radiation and has a low equilibrium temperature. Grain size is therefore not a strong determinant of temperature. The absorption coefficient k , can be set at an arbitrarily low number to imitate a small amount of absorption (such as that found in micrometeorites).

Magnetite (Fe_3O_4)

The scattering efficiencies for magnetite are similar to metallic spheres with very high refractive indices. The absorption efficiency is ≈ 1 throughout the spectrum.

We assume that grains of various sizes and composition, contribute to the overall shape and temperature of the spectrum. Mie theory gives the absorption efficiencies and leads to the temperature of such grains. Consider the energy balance between absorbed sunlight and emitted thermal radiation. If an equilibrium temperature is reached,

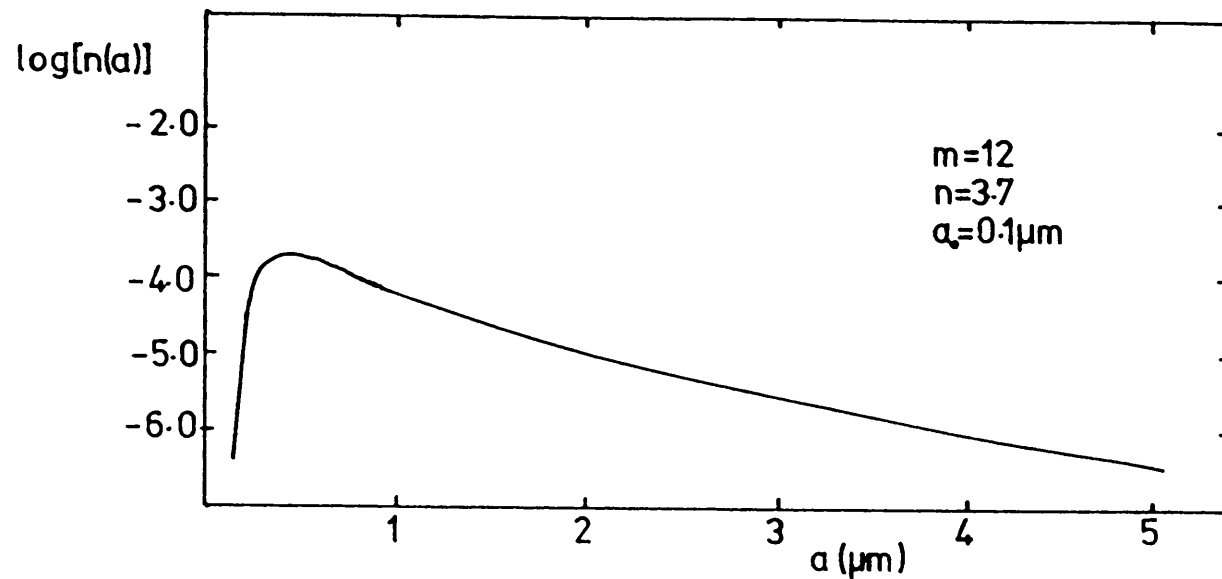
$$\frac{\pi a^2}{r^2} \int_0^{\infty} Q_{abs}(m, a, \lambda) S_{\lambda} d\lambda = 4\pi a^2 \int_0^{\infty} \pi B_{\lambda}(T) Q_{abs}(m, a, \lambda) d\lambda \quad \dots (1)$$

where a =particle radius, r =heliocentric distance in AU, S_{λ} =solar flux at 1AU, πB_{λ} = blackbody flux for a given temperature T .

An iterative approach is used to balance the two sides of the equation for a given a , r , and substance (Q_{abs}). Magnetite grains with $a < 1\mu\text{m}$ are hotter than the blackbody temperature, the small grains cannot radiate efficiently in the infrared. Olivine grains (with $k=0.01$) have approximate blackbody temperatures for all sizes at 1AU. For $r \ll 1\text{AU}$ they are hotter, the peak of the Planck function moves away from the middle infrared where grains can radiate efficiently. For $r > 1\text{AU}$, the grains are cooler, the peak of the Planck function moves to the middle infrared and can suppress the $10.2\mu\text{m}$ silicate feature. Integration of thermal emission with a size distribution is the next step. Previous size distributions deduced from tail observations failed to fit the infrared spectrum at long wavelengths. Hanner (1983) proposes

$$n(a) = \left(\frac{1 - a_0}{a} \right)^m \left(\frac{a_0}{a} \right)^n$$

where a_0 is the minimum grain radius, m and n are varied to fit the data, a_p is the peak radius (or sometimes thought of as the maximum grain radius which can be lifted from the nucleus) $= a_0(1 + m/n)$. In fact "n" defines the slope of the size distribution at large "a". Hanner's relative size distribution has an advantage over, say, a Gaussian distribution in that it can have an artificial cut-off at small grain sizes. Such small grains ($a < 0.1\mu\text{m}$) are not plentiful, otherwise the scattered spectrum would appear much bluer, and they do not contribute significantly to the infrared spectrum. The diagram below shows a plot of $\log[n(a)]$ versus a , for $m = 12$, $n = 3.7$ and $a_0 = 0.1\mu\text{m}$.



The variable "n" controls the size distribution. If "n" is increased there are more smaller particles than larger and vice versa. If "m" is increased/decreased the opposite effect happens as to varying n, but on a less effective scale.

A program written by N.Eaton performs the following steps to produce spectra which are dependent on size distributions and grain types.

1. For a given grain size, grain type and heliocentric distance the refractive indices and Mie coefficients are calculated for a range of wavelengths (0.17 to 55μm).
2. Q_{abs} for each wavelength is determined and the left hand side of equation (1) is calculated.
3. Refractive indices and Q_{abs} are calculated for $0.5 < \lambda < 30\mu\text{m}$.
4. Choosing a wavelength range 0.1 to 20μm for the infrared spectrum, Planck's function is used to find the black body flux at each wavelength.
5. For an initial estimate of the grain temperature the black-body formula $T=277/r^{0.5}$ is used. Hence the right hand side of equation (1) is calculated.
6. The temperature is varied until the two sides of the

equation balance to within a certain degree of accuracy.

7. The process is repeated for various grain sizes (1 to 20 μ m).

8. For a size distribution, Q_{abs} and T values are noted from the above process (1-7).

9. For a given wavelength the right hand side of equation 1 is calculated for a given size. Using the parameters m and n, the number of grains of this size is determined.

This number is then used to calculate the total flux for this wavelength and size. The process is repeated for all sizes and then for all wavelengths.

10. The total flux for each wavelength, is output to produce a relative spectrum.

4.4 Application of Mie Theory to Comet Halley

As part of the IHW campaign to monitor Comet Halley in the infrared, a seven day observing run was carried out using the 1.9m SAAO during April 1987. Many problems were encountered including bad weather conditions, changing sensitivity due to instrumental problems and finally the removal of the Q filter towards the end of the week. Multi-aperture photometry was performed using H,M,N and Q filters. The comet was tracked in RA and Dec. but there was a certain amount of backlash in the Dec tracking. Therefore during the multi-aperture photometry procedure, the aperture was repeatedly reset on the cometary nucleus.

A television screen was used to centre each aperture on the comet. During the week, Halley changed from a bright point source-like object to a diffuse object at the end of the week. Centring therefore became a problem, particularly on the last night (April 21/22). The chop size was varied during the week. While Halley was a point-like source with a very steep intensity profile, a chop size of 36" was used for apertures placed at the cometary centre (various chop sizes were tested, but the profile was so steep that the differences in magnitude were only ≈ 0.1). Offsets (up to 60" East and West) had their chop size increased to 102" so as not to chop across the same intensity contour. While Halley was diffuse this larger chop size was used.

The maximum chop size for the nuclear region was limited by the size of the television screen (80x80") and the need to guide on the comet centre. All chopping was done in a North-South direction.

The results were calibrated using the standard stars

listed below (Thomas et al. 1973),

Infrared Standard Stars

		H	M	N	Q
α Car	2326	-1.36	-1.43	-1.52	
λ Vel	3634	-1.50	-1.41	-1.73	(-1.9)*
ϵ Mus	4671	-1.29	-1.28	-1.63	
2 Cen	5192	-1.49	-1.53	-1.85	

* Assumed magnitude (I.Glass, private communication)

The above standards were used to calculate extinction coefficients: $H=0.06$, $M=0.28$, $N=0.10$, $Q=0.35$. Unfortunately, sky transmission values and filter responses could not be obtained, and so the M, N and Q magnitudes could not be reduced to monochromatic magnitudes (see for example the reduction of the Arend-Rigaux data, chapter 5.2). However magnitudes and λF_{λ} values were calculated using the filter wavelengths and zero-magnitude fluxes defined by Hanner et al. (1984), (see Table 11).

Results

Fig.20 shows the infrared spectra obtained during the observation run. Fig.20a displays the spectra taken with the same aperture (9") but on different nights. At first glance it appears that Halley was brighter in the infrared on April 20/21. However caution must be exercised as there were sensitivity problems during the nights 17/18 and 19/20.

TABLE 11a

Comet Halley Infrared Results - 1.9m SAAO*

<u>Date</u>	<u>SAST</u>	<u>Ap.</u>	<u>Chop</u>	<u>Filter</u>	<u>log(λF_{λ})</u>	<u>Mag.</u>	<u>Error(+)</u>
17-18/4/86	20 39	9"	36"	H	-12.03	8.21	.30
	21 17			M	-11.79	4.43	.10 (1)
	21 15			N	-10.76	-0.50	.14
	21 16			Q	-10.83	-2.51	.04

19-20/4/86	19 20	9"	36"	M	-11.83	4.54	.10
	19 25			N	-10.71	-0.63	.05 (2)
	19 37			Q	-10.96	-2.19	.03

20-21/4/86	19 52	9"	36"	H	-11.70	7.40	.10
	19 48			M	-11.67	4.12	.03
	19 41			N	-10.57	-0.97	.03

	20 15	6"	36"	H	-11.85	7.78	.10
	20 09			M	-11.90	4.70	.10
	19 59			N	-10.80	-0.40	.10 (3)
	20 37			H	-11.85	7.77	.10
	20 30			M	-11.91	4.73	.10
	20 20			N	-10.80	-0.39	.10

	21 55	11"	36"	H	-11.55	7.02	.09
	21 49			M	-11.63	4.02	.09 (4)
	21 42			N	-10.51	-1.12	.09

	22 48	9"		H	-11.65	7.28	.08
	22 45			M	-11.73	4.27	.08 (4)
	22 39			N	-10.61	-0.87	.08

	23 18	9"	102"	N	-12.17	3.03	.10 (5)
		(30"W)					

	00 15	9"	102"	N	-12.49	3.83	.15
		(60"W)					
	00 22	9"	102"	N	-12.83	4.69	.25 (6)
		(60"E)					
	00 31	9"	102"	N	-12.17	3.03	.06
		(30"E)					

	01 05	9"	102"	N	-11.12	0.40	.40 (7)
		(12"W)					

21-22/4/86	20 18 9"	36"	H	-12.07	8.33	.03	
	19 56		M	-12.02	5.01	.03	
	19 47		N	-10.90	-0.14	.03	
	21 53 11"	36"	H	-11.98	8.10	.10	
	21 42		M	-11.98	4.90	.08	
	21 17		N	-10.88	-0.20	.08	(8)
	23 07 11"	36"	H	-11.96	8.04	.10	
	23 23		M	-11.99	4.93	.08	
	23 27		N	-10.86	-0.24	.08	
	01 05 6"		M	-12.13	5.29	.15	
	01 10		N	-11.00	0.11	.15	(9)

* The observational data were obtained by Dr.I.Skillen.

(1) Changing sensitivity problems

(2) As above and readings at a high air mass

(3) Centering errors involved with difficult tracking

(4) Seeing 4"

(5)+(6)+(7) Offset positions were only detectable in N

(7) Poor seeing and high air mass

(8) Comet very diffuse making guiding difficult

(9) As above and centering problems

Reference Wavelengths and Zero Magnitude Fluxes

<u>Filter</u>	<u>λ_{ref}</u>	<u>E_{λ} for $0^m .0$</u>
H	1.68 μ m	$1.08 \times 10^{-9} \text{ Wm}^{-2} \mu\text{m}^{-1}$
M	4.80	2.00×10^{-11}
N	10.10	1.09×10^{-12}
Q	20.00	7.30×10^{-14}

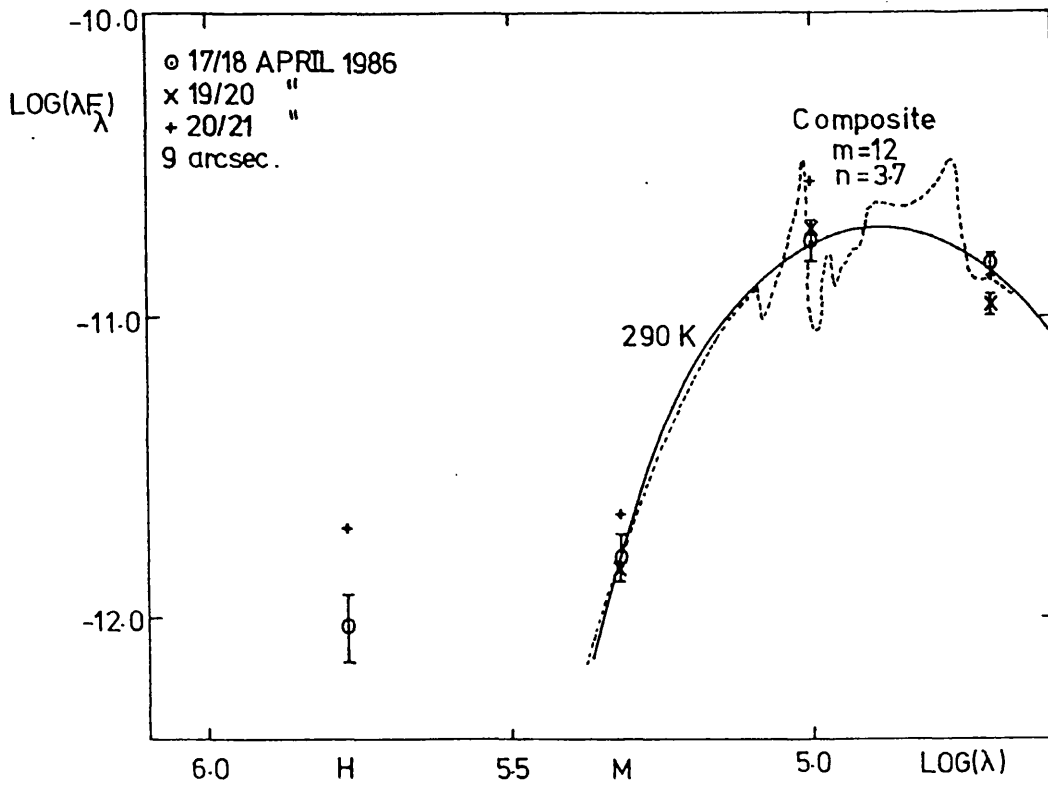


Fig.20a. Infrared spectra of P/Halley taken on three different nights with a 9 arcsec. aperture. The solid curve shows a 290K blackbody fit to the 17/18 April data. The dotted line represents a theoretical spectra from a size distribution of composite grains again fitted to the 17/18 April data. See text for details.

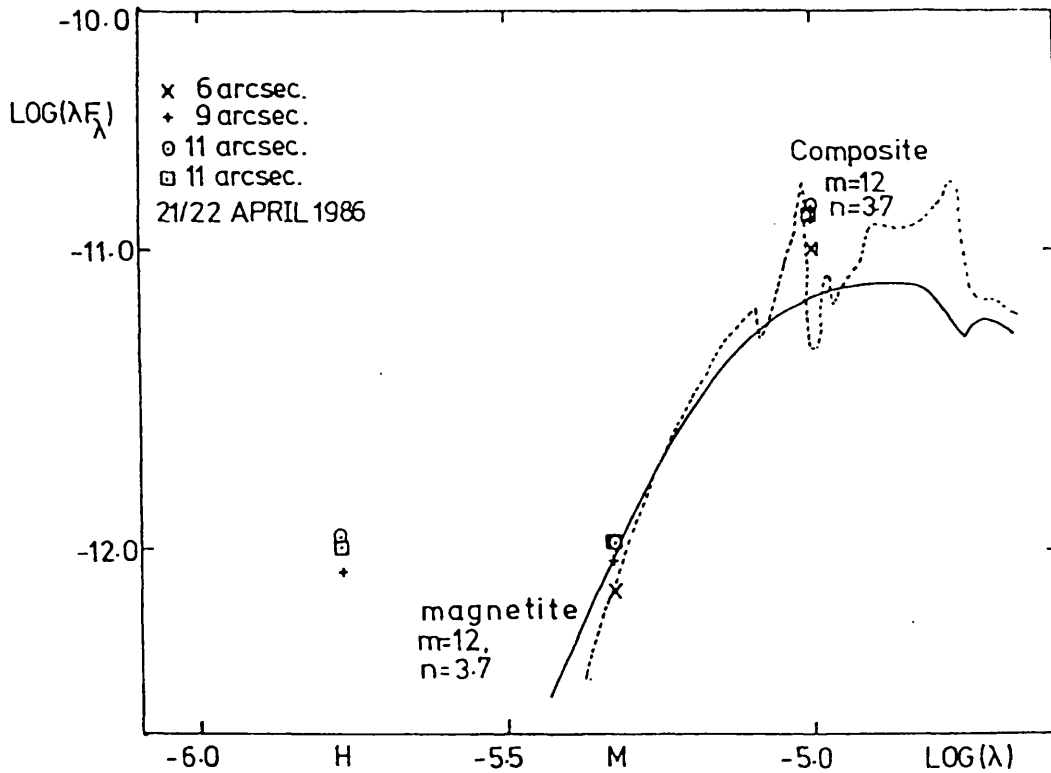
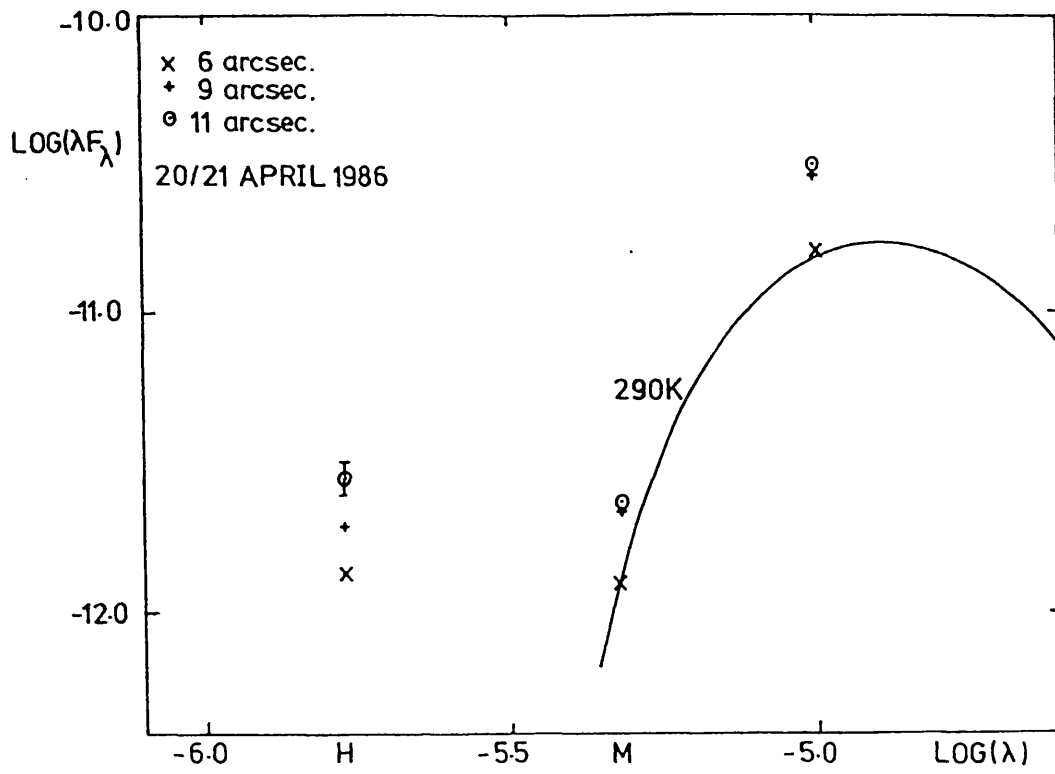


Fig20b+c. Infrared spectra of P/Halley taken on 20/21 April 1986 (b) and 21/22 April (c) with a range of aperture sizes. The solid line in Fig.20b shows a 290K blackbody fit to the 6 arcsec data. In Fig.20c the solid line represents a theoretical spectra from a size distribution of magnetite grains and the dotted curve from a size distribution of composite grains. See text for details.

Figs.20b+c show the spectra obtained during 20/21, 21/22 with 6,9, and 11" apertures.

Fig.20b shows a clear difference between the 6 and 11" apertures while the comet was point-source like. By the end of the week this difference was not so marked. The decrease in brightness was ≈ 0.9 mag. for the H,M and N filters.

On April 20/21 the N filter was used to determine offset magnitudes (the comet could not be detected at the other filter wavelengths). Table 10 (chapter 3.6) shows the steepness of the N profile. For e.g., at the 30" position the brightness has dropped by 3.9mag. At distances greater than this, the comet appears non-symmetrical, the magnitude falls-off by 4.7mag. towards the West and 5.6mag. towards the East.

Although some spectra were only represented by two or three data points, black-body functions were fitted to each spectra, and although the visual appearance of the comet changed, its mean grain temperature, $T=290K \pm 10K$ did not. (see Fig.20a). This temperature is $\approx 60K$ higher than the black-body temperature at the same heliocentric distance and only 20K higher than the temperature, calculated from the formula given by Eaton (1984) which is a mean fit to all known dust temperatures as a function of heliocentric distance. Such a high temperature indicates that the spectrum is dominated by the presence of small absorbing grains ($<10\mu m$) which cannot radiate efficiently at these wavelengths (Campins and Hanner, 1982).

The mean albedo of these grains can be found (Ney, 1982).

The albedo γ is given by,

$$\left(\frac{\gamma}{1-\gamma} \right) = \left(\frac{(\lambda F_{\lambda \max})_{VIS}}{(\lambda F_{\lambda \max})_{IR}} \right)$$

TABLE 11b

Mass Loss Rates \dot{M} for Comet Halley - 1.9m SAAO

<u>Date</u>	<u>Aper.</u>	<u>$(\lambda F_{\lambda_{max}})_{IR}$</u>	<u>\dot{M}</u>	<u>$\dot{M}(1AU)$</u>
	<u>(")</u>	<u>$\times 10^{-15} Wm^{-2}$</u>	<u>$kg s^{-1}$</u>	<u>$kg s^{-1}$</u>
17-18/4/86	9	2.19	3335	6820
20-21/4/86	6	1.82	4777	10323
	9	3.16	5221	11948
	11	3.47	4968	10735
21-22/4/86	6	1.05	2793	6284
	9	1.45	2571	5785
	11	1.51	2190	4928
0 ^h GMT 18/4/86	$\Delta = .47AU$	$r = 1.43AU$	phase angle = 20.9°	
20/4/86	$\Delta = .54AU$	$r = 1.47AU$	21.4°	
21/4/86	$\Delta = .56AU$	$r = 1.50AU$	22.1°	

By fitting a solar spectrum (taken from Labs and Neckel, 1970) to the available H data points, and the 290K black-body spectrum to the infrared points, pairs of $\lambda F_{\lambda \text{max}}$ values could be found. The resulting albedos range from $\gamma = 0.11$ to $\gamma = 0.27$. No systematic change in albedo occurred during the week.

Dust mass-loss rates were calculated, from the observed thermal flux, using the method described by Ney (1982) (see App.3). The April 19/20 spectrum was omitted because the Q data point was not a good fit to the 290K black-body curve. The second set of 9" results from April 20/21 were not used as they had larger errors than the first set. Likewise the first set of 11" results were not used for April 21/22. The mass loss results can be found in Table 11b.

Green et al. (1986) calculated approximate mass loss rates, for Comet Halley during 1985 and up to May 1986. Their results range from $\dot{M} = 100$ to $10,000 \text{ kgs}^{-1}$. Tokunaga et al. (1986) observed Comet Halley during late 1985 and early 1986 (pre-perihelion). Using a more detailed and model dependent approach to calculating mass loss rates, (taking into account a size distribution, the total area of the grains, a velocity distribution and assumed grain density) values between 100 and 9000 kgs^{-1} were found. The latter maximum occurred on 1986 January 8. This author's results may also be compared with the average $\dot{M} = 4 \times 10^3 \text{ kgs}^{-1}$ for long period comets quoted by Ney (1982). Although Ney's procedure is approximate it does show that the dust mass loss rate decreased (by a factor of 1/2) when the visual appearance of the comet changed on 21/4/86.

Although the Halley spectra consisted of only a few data points, Mie theory was applied and tested. A size

distribution,

$$n(a) = \left(\frac{1-a_0}{a} \right)^m \left(\frac{a_0}{a} \right)^n$$

with $a_0 = 0.1\mu\text{m}$ (grains with radii smaller than this do not contribute significantly to the observed fluxes), and $m=12$ $n=3.7$ was assumed. (Following Hanner's example, (1984), and the previous antitail work by Sekanina (1979), (although an infrared spectrum is mostly produced by grains with radii $<20\mu\text{m}$)).

Three different types of grain material were considered: 1) magnetite 2) olivine, to represent silicate features, although the relative number of grains necessary to produce an observable feature at $10\mu\text{m}$ is related to temperature which again depends on their absorption properties. A small absorption index, $k=0.01$ is therefore introduced and 3) a composite material defined by Hanner (1983) to represent absorbing grains with silicate emission features. This composite material is a combination of two refractive indices, $n=1.66-0.4i$ for $\lambda < 8\mu\text{m}$ and an olivine refractive index for $\lambda > 8\mu\text{m}$. The resulting grain temperatures are similar to magnetite but the smallest grains $a_0 = 0.1\mu\text{m}$ are $\approx 100\text{K}$ cooler. The optical constants for olivine and magnetite were taken from Huffman and Stapp (1973), and the infrared constants for disordered olivine from Kratschmer and Huffman (1979) and Kratschmer (1980). The infrared constants for magnetite have been obtained from Hanner (personal communication). The resulting spectra were shifted relative to the Halley spectra to achieve a good fit. The olivine spectrum was relatively smooth, but with a sharply defined peak at $\lambda \approx 12\mu\text{m}$ which represents the silicate feature. No variation of m

or n could produce an olivine spectrum to fit the data. This is not surprising, a small amount of absorption cannot raise the temperature high enough to fit the observational data. A magnetite spectrum is smooth throughout the wavelength range, apart from a small absorption around $18\mu\text{m}$. A composite spectrum has many sharp peaks and dips between 6 and $13\mu\text{m}$ and a broader emission feature between 13 and $18\mu\text{m}$. Obtaining a good fit with either composite or magnetite spectra, by varying m or n , proved difficult due to the limited number of data points and the knowledge that the N data points could be contaminated by the silicate emission feature which was reported to be quite variable by Gehrz and Ney (1986). If we assume that the N point is on the downward slope of the sharp emission peak centred on $\lambda \approx 9.3\mu\text{m}$ and then fit the spectra, ^{one finds that} $m=12$ with $n=3.7$ is a reasonable fit for the composite spectrum (Fig.20a+c). The magnetite spectrum for $m=12$, $n=3.7$ is also shown for comparison (Fig.20c). It is interesting to note that the maximum size a_p where, $a_p = a_0(1 + m/n)$ and $m=12$, $n=3.7$, is $a_p \approx 0.4\mu\text{m}$. The diameter of such a grain, gives rise to β values $=1.5$ ($\rho=1\text{gcm}^{-3}$) and $\beta=0.5$ ($\rho=3\text{gcm}^{-3}$). The first β value lies in the range of grains for which $F_{\text{rad}} > F_{\text{grav}}$ and the orbits are convex hyperbolae. The latter β value corresponds to grains for which $F_{\text{rad}} < F_{\text{grav}}$ and the resulting concave orbit maybe eccentric or hyperbolic. A β value of 0.5 is well within the range of grains found to be contributing to the dust tail of Halley's comet (see chapter 2.3).

Intercomparison of Albedos

Fig.21 has been taken from Gehrz and Ney (1986). It clearly shows the variation of albedo with scattering angle for Comet Halley. The limits of the albedo range, calculated by this author are also shown on the diagram.

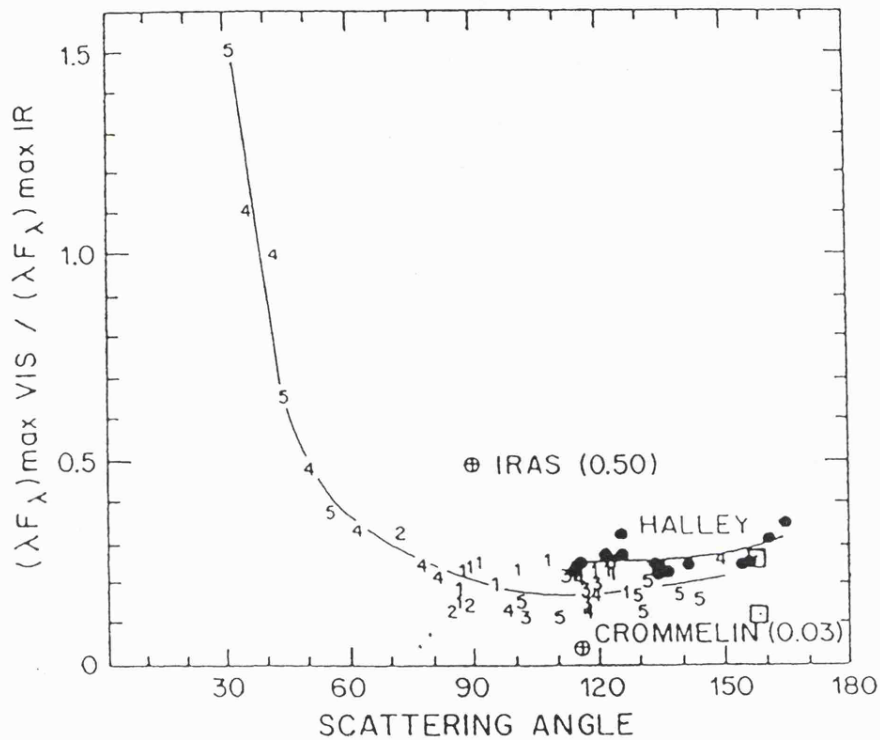


Fig.21 The albedo of comet grains as a function of scattering angle (Gehrz+ Ney, 1986).

- 1 Kohoutek 2 Bradfield 1974b
- 3 Kobayashi-Berger-Milan 4 West
- 5 Bradfield 1980t
- Solid circles - Halley (Gehrz + Ney)
- Open boxes - Halley (this author)

4.5 Conclusion

During the week 17-23/4/86, the physical appearance of P/Halley changed considerably, from a bright point-like source to a diffuse nebulous object. Although its appearance changed, its mean dust grain temperature, deduced from the infrared spectra, remained constant at $T=290K \pm 10K$. This temperature is $\approx 60K$ hotter than a blackbody temperature at a similar heliocentric distance, indicating the presence of small absorbing grains ($< 10\mu m$) which dominate the spectrum. The mean albedo of the grains was found to be in the range $0.11 < \gamma < 0.27$, and did not change appreciably during the week.

Mass loss rates were calculated, giving an average of $4.6 \times 10^3 \text{ kgs}^{-1}$ for the beginning of the week and $2.5 \times 10^3 \text{ kgs}^{-1}$ at the end of the week - a decrease, by a factor of two.

The presence of small absorbing grains was also confirmed by the application of Mie theory. Theoretical modelling with grain materials, such as magnetite (absorbing) and a composite material (magnetite and olivine) gave reasonable fits to the observed infrared spectra. Hanner's (1983) size distribution, with $m=12$ and $n=3.7$ also proved a reasonable fit. Such a distribution has its peak radius at $0.4\mu m$. Such small grains are confirmed to be present in the dust tail (chapter 2).

To summarize, the application of Mie theory is in itself quite useful as a first approximation, to modelling cometary spectra. However chapter 2 indicates that the dust tail of P/Halley possessed very small/low density grains of a crumbly nature. Such a physical deviation from the assumed "dust grain sphere" causes the breakdown of Mie theory. More complex scattering functions (covering a range of physical shapes) and

physical constants (to cover the diversity of chemical constituents) are needed for the modelling of cometary spectra.

CHAPTER 5

DETECTION OF FAINT COMETARY ACTIVITY

5.1 Comet Halley - Early Preperihelion Images

The Recovery and Coma Development of Comet Halley

Jewitt and Danielson (1982) recovered Comet Halley on 16 October 1982 using the 5.1m telescope on Palomar Mountain and a CCD electronic camera. The comet was 11AU from the Sun and its visual magnitude was estimated to be 24.2mag. From that day, observers began photometric programmes to monitor the comet's changing brightness.

Observations of comets over large distances can provide a critical test of water ice sublimation models. It is thought that sublimation of water does not occur at distances greater than 3AU. A few comets at $r > 3\text{AU}$ have been observed to have extended comae, e.g. Comet Kohoutek (at $r=4.6\text{AU}$), and processes other than water sublimation are thought to contribute to coma formation. For example, CO_2 is a substance which is more volatile than water. Spinrad et al (1984b) produced the first clear evidence of a coma (an extension was seen 6" to the North) during 1984 September 25-27. Meech and Jewitt (1986) reported photometric evidence of coma formation in October 1984. By comparing magnitudes (as a function of "r") for standard thermal models of slowly rotating, low albedo, asteroids with those found for the comet, it could be seen that at $r=5.1\text{AU}$ (January 1985) Halley deviated markedly. Meech and Jewitt attributed this brightening to the production of a coma containing dust grains, which had been emitted in September 1984, and due to the sublimation of water ice. Wyckoff et al. (1985) also proved that the onset of sublimation began during this month. Prior to September 1984, many observers reported fluctuations of \approx one magnitude when Halley was at large heliocentric distances, but this has been

attributed to nuclear rotation effects.

The UK Schmidt telescope began its search for Comet Halley in September 1982. Regular exposures of the correct sky field area did not occur until late 1984, and it was in December 1984 that the comet's image was successfully found. A selection of these early Halley plates was digitised by COSMOS.

Plate Details

The plates were taken using a VR filter. At such large heliocentric distances the plates were probably sensitive to light scattering by dust particles and not to any gaseous emissions. The dates of these images ranged from 1984 December 19 to 1985 March 17 ($r = 5.4$ to 4.7 AU, $\Delta = 4.4$ to 4.7 AU). Although the exposure times were 30 mins, Halley appeared as a tiny speck. On some plates the image had to be clearly identified amongst the many images produced by asteroids in the ecliptic plane.

The Aim of the Analysis

It was originally hoped to have a large set of early Halley images and by various means, detect the presence of a coma surrounding the nucleus, hence proving that sublimation was taking place. The first method, using changing relative magnitudes, was ruled out owing to differences in plate exposure times and sky background values (which were sometimes hard to determine). The Starlink software would not permit aperture photometry on such small images. The method finally used was that of comparing relative intensity profiles of the comet image with those of nearby star trails (taken to be point sources).

Method

The Halley images were situated in a dense star field and where possible, two scans at right angles were taken across each comet image. On each plate one or two stars were chosen (of comparable brightness to the comet) and scans normal to the star trails were recorded. The star and comet profiles were then normalised to the same peak relative intensities. In this way the shape of the two profiles could be compared.

Results and Conclusion

There was no evidence that the comet profile was broader than any star profile. The conclusion therefore is that the photographic plates could not detect any signs of coma activity during late 1984 and early 1985.

5.2 Decaying Comets: Optical and Infrared Measurements

Infrared and Optical Observations of Low Activity

Comets, P/Arend-Rigaux (1984k) and

P/Neujmin 1 (1984c)

Introduction

The evolutionary links between short period comets and Apollo asteroids have been discussed frequently (Green et al. 1985a; Degewij + Tedesco 1982; Hughes 1982). Hartmann (1985), and coworkers have suggested that cometary nuclei have similar spectral properties to the dark, red, outer main-belt D-type asteroids. Marsden (1970, 1971, 1972) has indicated that (i) the size of the non-gravitational effects and (ii) the object's closest approach distance to Jupiter are important parameters to be considered in this respect. Arend-Rigaux and Neujmin 1 (thought to be transitional objects between asteroids and comets) are two short period comets that have approached Jupiter to within 0.9AU during the past two hundred years. The numbered asteroids do not come within 1.1AU of Jupiter and their orbits are considered to have long-term stability. However, Kresak (1980a) has argued that although the orbits of Arend-Rigaux and Neujmin 1 are stable, they will not evolve into typical asteroid-like orbits.

It has also been noted that Arend-Rigaux and Neujmin 1 display the lowest level of activity amongst known comets. At times of minimum activity, the spectrum of Arend-Rigaux has resembled that of an RD-type asteroid (low albedo and red colours longward of $0.7\mu\text{m}$), although it has been known to have a weak coma at small heliocentric distances, showing the presence of $\text{CN}(0,0)$, C_3 , $\text{C}_2(1,0)$ and $\text{C}_2(0,0)$ emission bands. Sekanina (1976a) has plotted photographic nuclear magnitudes

versus phase angle for both Arend-Rigaux and Neujmin 1, and has concluded that the measurements follow an asteroidal phase relation, suggesting that ^{these} comets have optically thin comae.

Comets Neujmin 1, Arend-Rigaux and Shoemaker, along with the asteroid 3200 Phaethon passed their perihelia near the end of 1984 or early 1985. This provided a unique opportunity for study and intercomparison. An infrared observational programme was devised with a back-up of photographic plates from the UK Schmidt Telescope. The results for 3200 Phaethon have been published previously (Green et al. 1985a)

Comet Neujmin 1 (18.21yr period) was recovered on 1984 February 26 with a reported stellar appearance (Gilmore and Kilmartin, 1984). In August, CN and OH were detected, indicating weak activity (A'Hearn et al., 1984). Continuum measurements suggested a nuclear radius of 9.5km and geometric albedo 0.02 with little or no surrounding dust; the continuum colours were similar to those of S- or C-type asteroids (depending on the time of observation). However the combination of red colours with steeper near-ultraviolet spectrum, and a very low albedo was not consistent with any known type of asteroid. In September (Barker, 1984), the coma showed only a reflected solar continuum in the central condensation, but a fan (extension 12 arcsec to SE) displayed the presence of CN and C₂. This emission was detected 7 arcsec from the central condensation, and suggested that the solar continuum masked the emission at the centre.

Comet Arend-Rigaux (6.84yr period) was recovered 1984 August 6, it was mainly stellar in appearance, but with a faint tail 1-2 arcmin long at PA255° (Gibson 1984). Optical

and infrared observations in January 1985 (A'Hearn, 1985) indicated neutral colours similar to F- or C-type asteroids. The comet was clearly extended, and from the aperture-dependence of observed magnitudes the contribution from the nucleus was derived. An axial ratio of 1.7, rotation period of 13.5 hrs, radius of 5km at maximum light, and albedo 0.02 ± 0.01 were derived. Tokunaga + Hanner (1985) also observed P/Arend-Rigaux on 1985 January 18-20 but found no detectable dust coma. They derived an average dust radius of 4.8 ± 0.4 km and geometric albedo at $1.25\mu\text{m}$ of 0.05 ± 0.01 . Brooke and Knacke (1986) observed P/Arend-Rigaux on 1985 February 16 and concluded that it had a dark RD-type nucleus of radius 5.1 ± 1.1 km and geometric albedo 0.02 ± 0.01 . They also detected a faint coma. Jewitt and Meech (1985) used a CCD for cometary photometry and deduced a nuclear rotation rate of $P=9.58$ or $P=6.78$ hrs.

Comet Shoemaker (1984s), a long period comet, was discovered 1984 October 25 as a diffuse object (Shoemaker + Shoemaker, 1984), but later in November developed a tail (McNaught, 1984). In December, weak OI (630nm) emission, was detected out to a distance of 4.5 arcsec from the nuclear region (Belton et al. 1985).

Optical Observations

The 1.2m UK Schmidt telescope was used to obtain a total of six photographic images of Arend-Rigaux, Neujmin 1 and asteroid 3200 Phaethon. Unfortunately the 3200 Phaethon images suffered from tracking errors, but there was no sign of any cometary extension. Data concerning the six images are given in Table 12. The expected main cometary emissions have been taken from Wyckoff (1982). On the COSMOS machine a 32 μ m spot size and 16 μ m increment was used for Neujmin 1, and a 16 μ m spot size and 16 μ m increment for Arend-Rigaux. The scales are thus 1 pixel \approx 2 arcsec for Neujmin and 1 pixel \approx 1 arcsec for Arend-Rigaux, although the spatial resolution was limited by seeing to 4-6 arcsec. The photographic densities have been converted to relative intensities via a sensitometric step wedge.

TABLE 12
UK Schmidt Plate Summary

<u>OBJECT</u>	<u>DATE</u>	<u>PLATE</u>	<u>MID</u>	<u>EXP.</u>	<u>FILTER/</u>	<u>EFFECTIVE</u>	<u>POSSIBLE</u>
				<u>EXPOSURE (MINS)</u>	<u>EMULSION</u>	<u>WIDTH</u>	<u>EMISSIONS</u>
					<u>COMBINATION</u>	<u>(NM)</u>	<u>(+CONTINUUM)</u>
P/NEUJMIN-1	14/12/84	J9806T	10 ^h 26 ^m 35 ^s	30	GG395+IIIaJ	395-534	C3,C2,CO+
P/NEUJMIN-1	14/12/84	OR9807T	11 7 35	30	OG590+IIIaF	630-690	OI,NH2,HI
P/AR.RIGAUX	20/12/84	J9823T	16 35 56	30	GG395+IIIaJ	395-534	C3,C2,CO+
P/AR.RIGAUX	21/12/84	OR9827T	16 47 59	30	OG590+IIIaF	630-690	OI,NH2,HI
3200 PHAETH.	24/12/84	J9835T	10 51 10	30	GG395+IIIaJ	395-534	Trailed
3200 PHAETH.	24/12/84	OR9836T	11 35 10	30	OG590+IIIaF	630-690	Trailed

Infrared Observations

Observations were carried out on 1984 December 20 and 21 using the 3.8m United Kingdom Infrared Telescope (UKIRT) on Mauna Kea, Hawaii. Photometry from 1 to 5 μ m was obtained using the infrared photometer UKT9 on the nights of December 20 and 21. A variety of aperture and chop sizes were used. A number of standards from the UKIRT list were observed on both nights for extinction corrections (A. Longmore, private communication). Photometry from 5 to 20 μ m was obtained for Arend-Rigaux on December 21, using the bolometer UKT8 with an aperture size of 6 arcsec and a 19 arcsec E-W chop. The standard stars α Tau, β And and β Peg were used for extinction correction and calibration (see Table 13). The adopted magnitudes (Hanner et al. 1984) required slight correction for the difference in reference wavelengths of the UKIRT wide-band filters and those on the IRTF (see Table 14). Wide bandpass photometric measurements can be reduced, (by Δm), to monochromatic magnitudes at a reference wavelength for each filter. The Mauna Kea sky transmission was obtained from Traub and Stier, (1976) and the filter responses from the Royal Observatory Edinburgh.

The derived magnitudes and fluxes for the three comets are given in Table 15. The corrections (Δm) to the magnitudes obtained with the wide-band filters are to allow for the difference between the stellar spectra (approximated by a black body for the 2-20 μ m region) used to calculate the reference wavelengths and the comet's spectrum over the bandpass. For Arend-Rigaux, the 5-20 μ m spectrum was represented by a best fit blackbody with $T=330\text{K}$. The corrections for the L and L' filters were made by assuming

TABLE 13

Infrared Standards

<u>Star</u>	<u>J</u>	<u>H</u>	<u>K</u>	<u>L</u>	<u>L'</u>	<u>M</u>
HD 77281	7.11	7.05	7.03	6.99	(6.98)	(6.98)
GL 347A	8.465	7.86	7.63	7.40		
BS 718	4.385	4.39	4.39	4.395	4.40	4.37
HD 225023	7.08	6.99	6.96	6.935	6.955	(6.95)
HD 1160	7.06	7.05	7.04	7.045	7.03	(7.03)
BS 3314	3.92	3.92	3.94	3.93	3.925	(3.93)

Uncertainties $0^m.02$

() Indicates estimated values from other magnitudes.

	<u>M</u>	<u>N</u>	<u>Q</u>	<u>8.7</u>	<u>9.7</u>	<u>10.3</u>	<u>11.6</u>	<u>12.5</u>
β And	-1.80	-2.09	-2.10	-1.97	-2.05	-2.07	-2.14	-2.18
β Peg	-2.20	-2.57	-2.62	-2.45	-2.53	-2.55	-2.64	-2.70
α Tau	-2.76	-3.01	-3.09	-2.98	-2.99	-2.99	-3.08	-3.14

Uncertainties $0^m.05$

TABLE 14

Reference Wavelengths and Adopted Zero Magnitude Fluxes.

<u>Filter</u>	<u>λ_{ref}</u>	<u>$^* \Delta\lambda$</u>	<u>F_λ for $0^m.0$</u>
	<u>(μm)</u>	<u>(μm)</u>	<u>($Wm^{-2} \mu m^{-1}$)</u>
J	1.25	0.3	3.3×10^{-9}
H	1.65	0.3	1.4×10^{-9}
K	2.2	0.4	4.0×10^{-10}
L	3.53	0.6	6.6×10^{-11}
L'	3.73	0.6	5.3×10^{-11}
M	4.73	0.5	2.1×10^{-11}
	8.7	1.2	1.9×10^{-12}
	9.7	1.0	1.3×10^{-12}
	10.3	1.0	9.9×10^{-13}
N	10.6	2.6	9.0×10^{-13}
	11.6	1.25	6.2×10^{-13}
	12.5	1.2	4.6×10^{-13}
Q	19.2	4.5	8.6×10^{-14}

* F.W.H.M. of convolution of sky and filter transmissions.

TABLE 15

Infrared Photometry of Comets P/Arend-Rigaux (1984k)
P/Neujmin 1 (1984c) and Shoemaker (1984s).

<u>TIME</u>	<u>INT.</u>	<u>APERTURE</u>	<u>CHOP</u>	<u>FILTER</u>	λ_{ref}	<u>MAGNITUDE</u>	<u>ΔM</u>
<u>(UT)</u>	<u>(SECS.)</u>	<u>(")</u>	<u>(")</u>		<u>(μm)</u>	<u>(\pm ERROR)</u>	
<u>P/AREND-RIGAUX 1984/12/20</u>							
1337	20	7.8	17	J	1.25	13.21 \pm 0.05	
1342	30	"	"	J	1.25	13.09 0.05	
1349	100	"	"	H	1.65	12.58 0.05	
1352	80	"	"	K	2.2	12.35 0.05	
1356	120	"	"	L	3.53	10.25 0.05	+0.08
1400	120	"	"	L'	3.73	9.29 0.05	+0.08
1404	160	"	"	M	4.73	7.28 0.10	+0.01
1412	140	19.6	68	J	1.25	12.41 0.05	
1416	120	"	"	H	1.65	11.97 0.05	
1419	80	"	"	K	2.2	11.78 0.05	
1450	36	7.8	17	J	1.25	12.94 0.05	
1453	100	"	"	H	1.65	12.50 0.05	
1456	80	"	"	K	2.2	12.27 0.05	
<u>P/AREND-RIGAUX 1984/12/20 5"N 2"E</u>							
1508	140	"	"	J	1.25	14.07 0.05	
1512	140	"	"	H	1.65	13.60 0.05	
1504	120	"	"	K	2.2	13.43 0.05	
<u>P/AREND-RIGAUX 1984/12/21</u>							
1323	80	7.8	25.5	J	1.25	12.94 0.05	
1316	100	"	"	H	1.65	12.43 0.05	
1335	40	"	"	H	1.65	12.48 0.05	
1319	80	"	"	K	2.2	12.23 0.05	
1322	120	"	"	L	3.53	10.02 0.07	+0.08
1326	120	"	"	L'	3.73	9.29 0.07	+0.08
1329	120	"	"	M	4.73	7.24 0.10	+0.01
1505	80	6.0	19	M	4.73	7.51 0.10	+0.01
1507	80	"	"		8.7	3.64 0.10	
1509	80	"	"		9.7	3.27 0.10	
1512	100	"	"		10.3	2.97 0.10	
1525	120	"	"	N	10.6	2.93 0.10	-0.02
1516	120	"	"		11.6	2.39 0.10	
1520	200	"	"		12.5	2.30 0.10	
1530	240	"	"	Q	19.2	1.37 0.16	-0.01
<u>SHOEMAKER 1984/12/21</u>							
0852	60	7.8	25.5	J	1.25	12.07 0.05	
0854	60	"	"	H	1.65	11.60 0.05	
0856	80	"	"	K	2.20	11.46 0.05	
0900	120	"	"	L	3.53	10.34 0.05*	
0904	200	"	"	L'	3.73	10.08 0.20*+	
<u>P/NEUJMIN 1 1984/12/21</u>							
0506	180	"	"	J	1.25	14.96 0.05	
0511	180	"	"	H	1.65	14.47 0.05	
0501	180	"	"	K	2.20	14.30 0.05	
0542	210	12.4	25.5	J	1.25	14.83 0.05	
0548	150	"	"	H	1.65	14.44 0.08	
0552	150	"	"	K	2.20	14.57 0.20	
20/12/84	0 ^h	UT		P/AREND-RIGAUX	r=1.461AU	Δ =0.602AU	Phase Angle=30°
21/12/84	0 ^h	UT		P/AREND-RIGAUX	r=1.463AU	Δ =0.598AU	Phase Angle=30°
"	"			SHOEMAKER	r=1.235AU	Δ =0.371AU	Phase Angle=44°
"	"			P/NEUJMIN 1	r=1.793AU	Δ =1.754AU	Phase Angle=31°

* The thermal spectrum of Shoemaker was not recorded, hence the corrections ΔM , could not be calculated.

+ Suspected cloud interference.

this model to be correct and adding the contribution from the reflected solar spectrum (Labs & Neckel, 1970) fitted to the J,H and K data. The J,H,K filters, which measure the reflected component of a comet spectrum, and the narrow-band filters do not require any corrections. The 10.3 μ m magnitude has been corrected to allow for a short-wavelength leak corresponding to 10% of the measured flux for the standard stars (M.S.Hanner, private communication).

The errors in the magnitudes correspond to statistical variations in measurements, uncertainties in extinction corrections and standard star magnitudes.

Discussion

Dust Distribution

Despite being a candidate for an inert cometary nucleus due to its association with the Geminid meteor stream, 3200 Phaethon showed no faint emissions during this apparition. Although incorrectly tracked, the 3200 Phaethon images showed no signs of nebulosity and the infrared observations (Green et al. 1985a) indicated a rocky surface.

Fig.22 shows the Arend-Rigaux and Neujmin 1 images. The sky background has been subtracted and the images smoothed using a 5 pixel Gaussian function. The contours have been drawn at various fractions of the peak intensity to show the structure present.

The Neujmin 1 plates show essentially stellar images although some extension and faint nebulosity is present to the East for the J image. The intensity profile across the centre of the J image is very similar to that of stars elsewhere on the plate except for the nebulosity which appears as a small deviation.

Both Arend-Rigaux images show definite extension towards

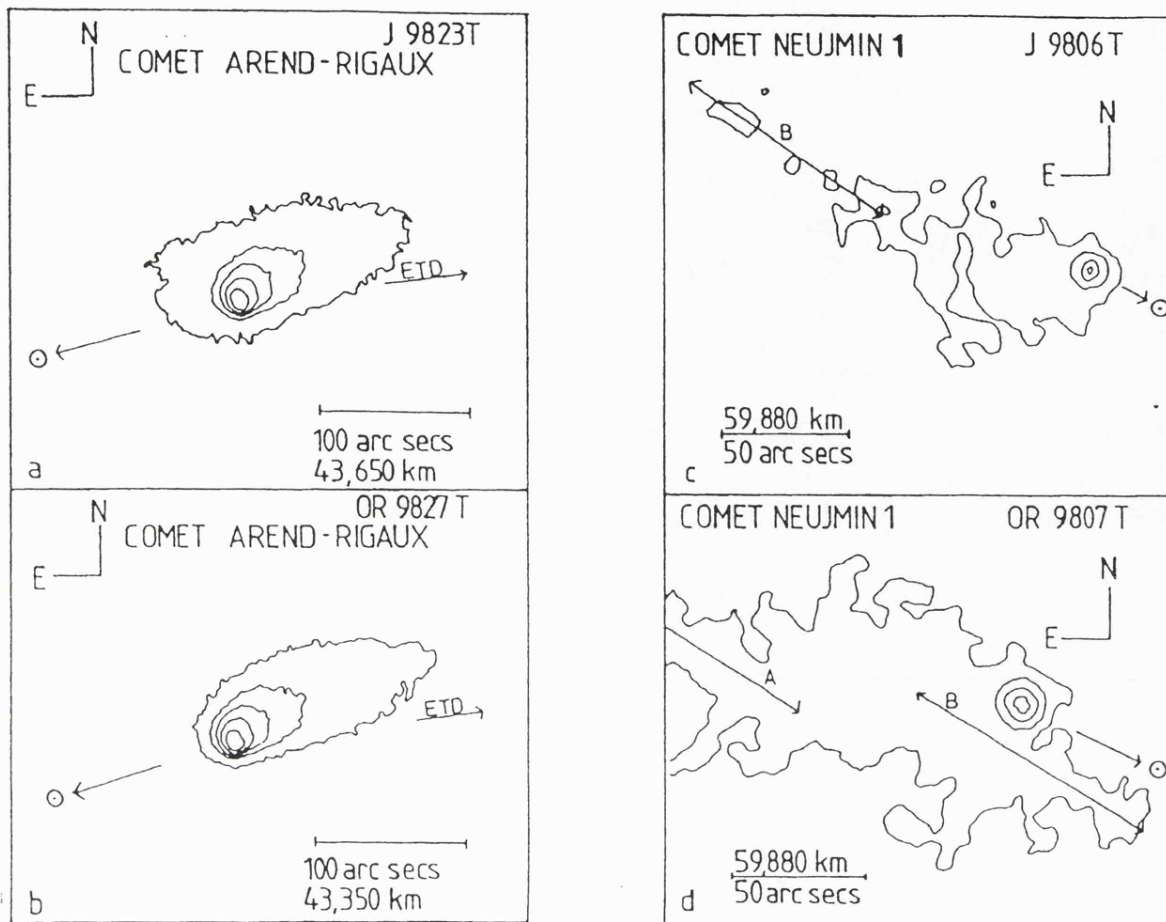


Fig.22 Intensity contour plots for P/Arend-Rigaux (a+b) and P/Neujmin 1 (c+d). The contours represent various fractions of the central maximum intensity: 0.1, 0.3, 0.5, 0.7, 0.9 for Arend-Rigaux and 0.01, 0.1, 0.7, 0.9 for Neujmin 1. The arrows labelled A and B denote star and galaxy contamination respectively. ETD marks the estimated tail direction from dynamical analysis (see text).

the North-West. Apart from the seemingly greater extension in the sunward direction (South-East) for the J image the two images are almost identical. This suggests that the contours are representative of the dust distribution. A best-fit ellipse was calculated for contours at intensities of 90%, 80% etc. of the peak, and the position angles indicated by the major axes of these ellipses were then computed. The results for both images (Table 16) are similar and suggest that there is a systematic change in the photometric axis of the comet from the central condensation outwards.

TABLE 16

Position Angles of the Major Axes For The Contour
Ellipses* for P/Arend-Rigaux

<u>Relative</u>	<u>Semimajor Axis</u>		<u>Position Angle</u>	
<u>Intensity</u>	<u>J9823T</u>	<u>OR9827T</u>	<u>J9823T</u>	<u>OR9827T</u>
10%	26,680km	32,450km	296°	299°
20	17,020	17,680	300	298
30	12,490	12,480	303	302
40	9530	9410	316	311
50	7420	7290	324	324
60	6140	6000	337	343
70	5060	4970	358	6
80	4190	4070	12	16
90	3350	2970	31	35

* Best fit ellipses to the intensity contours.

The position angles are measured from North to East.

A Finson-Probstein (1968) analysis (usually used on well developed dust tails) was attempted to explain the orientation of the contours. The nucleus of the comet is considered to be at the centre of a right-handed system of axes (ξ, η, ζ). ξ points radially away from the sun, η points directly away from

the comet's motion and ζ forms the right hand set. Both ξ and η lie in the comet plane. The trajectories of various sized dust grains under the influence of solar radiation pressure are then computed for various ejection times from the nucleus. The ejection velocity is assumed to be zero. The resulting dust tail is then projected onto the sky plane.

The syndynes for plausible particle sizes (see infrared data) lie along the lines marked ETD in Fig.22a+b. Isotropic ejection would produce a dust coma roughly symmetrical about this line. The data in Table 16 imply anisotropic emission possibly from an active region at P.A. 80-90° (θ for $a \rightarrow 0$, where "a" is the semi-major axis of a contour ellipse). The comet also showed extension up to 10 arcsec at P.A. 30° on the television finder at UKIRT. This is unlikely to be a single jet since the scale of the image is such that the outer contours indicate dust emitted some 4hrs previously. If this occurs on the "afternoon" side of the rotating nucleus, then the observing geometry would imply prograde rotation. Multi-aperture photometry was performed on the inner coma of the Arend-Rigaux OR image (presuming the light intensity is from dust scattering only). A plot of magnitude versus $\log(\text{aperture radius})$ (Fig.23) has a gradient n which is related to γ , where

$$\gamma = \left(\frac{-n}{2.5} - 2 \right)$$

and $\gamma = \text{gradient of surface brightness profile}$, such that $S \propto R^\gamma$ and R is the distance from the nucleus. A γ value = -1 would indicate a dust density distribution $\propto R^{-2}$. Points plotted in Fig.23 correspond to apertures of radius 10-30 arcsec. Outside this region the effects of radiation pressure

on the outflow direction of grains becomes significant.

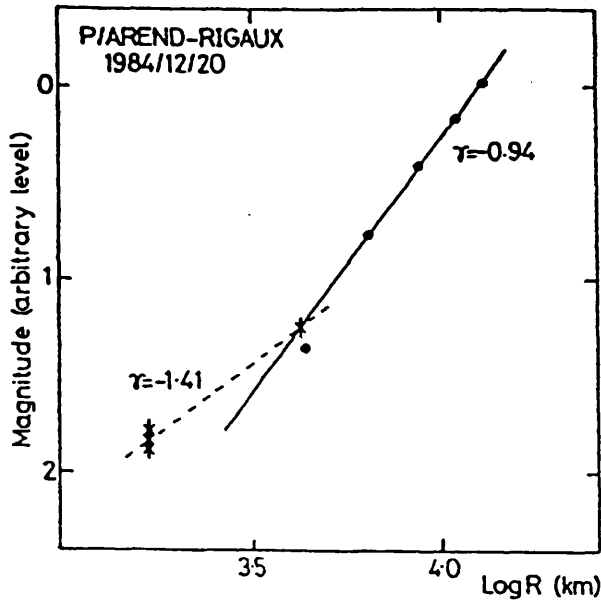


Fig.23 Magnitude versus $\log(\text{aperture radius})$ for multiaperture photometry of OR9827 (circles) and UKIRT JHK data (crosses). The γ values represent derived intensity distribution assuming $I \propto R^\gamma$.

The mean dust density distribution appears to follow an $R^{-1.94}$ relationship. Differences from R^{-2} will occur if the dust emission rate is not constant.

Fig.23 also shows the near infrared JHK photometry with 7.8 and 19.6 arcsec apertures, arbitrarily fitted to the Schmidt data at 19.6 arcsec. The large difference between the two data sets could indicate strongly variable emission or that the nucleus is actually providing a considerable fraction of the total observed intensity. If the latter is the case then this fraction can be calculated. The magnitude difference between the 7.8 and 19.6 arcsec apertures Δm is

$$\Delta m = m(7.8) - m(19.6) = 2.5 \log \left(\frac{I_c(19.6) + I_N}{I_c(7.8) + I_N} \right)$$

where I_c and I_N are the contributions to the observed intensity from the dust coma and nucleus respectively. For a radial intensity distribution $\propto R^\gamma$ the intensity observed in a given aperture $\propto R^{\gamma+2}$. For large apertures the nucleus contribution becomes small relative to the coma so $\gamma = -0.94$ is adopted and

$$I_c(19.6) = \left(\frac{19.6}{7.8}\right)^{1.06} I_c(7.8)$$

By substitution, $I_N = (1.41 \pm 0.13) I_c(7.8)$ and the nucleus contributes $(59 \pm 3)\%$ of the total observed intensity in the 7.8 arcsec aperture. For a 6 arcsec aperture this value is 65%.

Applying the same type of analysis to the J and H data for Neujmin 1 and assuming $\gamma = -1$ for the dust component indicates between 80 and 95% contribution from the nucleus. The observed J-magnitude is consistent with a nucleus of radius 8km for an albedo of 0.02, in good agreement with A'Hearn et al. 1984.

Dust Production and Nucleus Properties

Thermal emission from cometary dust usually dominates the observed infrared flux from comets. The wavelength of maximum emission falls within the range 3-20 μ m. Dust grains are thought to contain two components: hot absorbing grains responsible for grain temperatures (generally hotter than the equilibrium black body temperature) and silicate grains responsible for the 10 and 18 μ m emission features sometimes seen superimposed on the thermal emission. Fig.24 represents the infrared observations of Arend-Rigaux between 1-20 μ m on 21 December, reduced to an aperture size of 6arcsec [$m(7.8) - m(6) = 0.11\text{mag.}$].

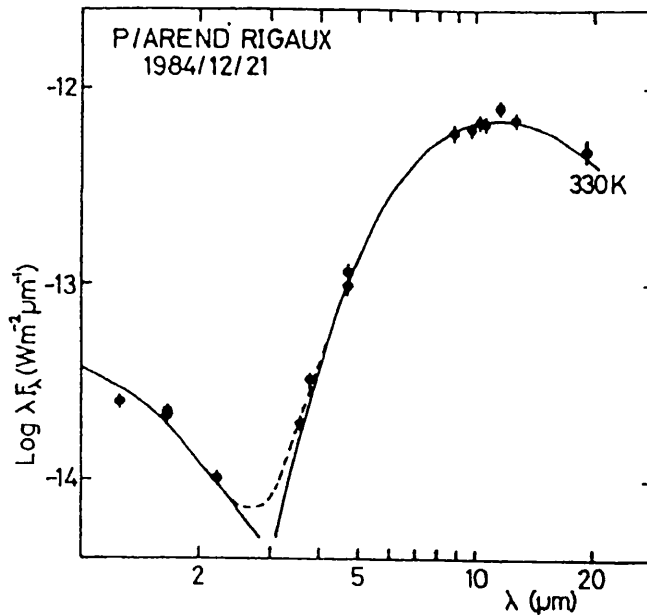


Fig.24 The December 21 infrared observations of P/Arend-Rigaux in a 6 arcsec aperture. A 320K blackbody fit to the 5-20 μ m data and solar spectrum fit to the 1-2 μ m data are also shown.

The best fit blackbody temperature is 330 ± 10 K. This is hotter, by 100K, than the equilibrium blackbody temperature $T=277r^{-0.5}$ (where r = heliocentric distance in AU) implying that the spectrum is dominated by absorbing grains smaller than about 10 μ m which cannot radiate efficiently at these wavelengths (Campins & Hanner, 1982), or by emission from the nucleus itself. Eaton (1984) found a mean dust grain temperature for 12 comets of $T=329r^{-0.53}$ with typical deviations of $\pm 10\%$ for individual observations. The observed temperature for Arend-Rigaux is 60K higher than the 270K predicted by this formula. The $\lambda=11.6\mu$ m flux is 20% above the corresponding 330K blackbody flux at the same wavelength. This difference is outside the error bars but at a longer

wavelength than the broad silicate emission feature, which has been previously noted in some other comets such as Comet Kohoutek (Ney, 1982). The observations of asteroid (3200) made at the same time show no such feature, ruling out the possibility of calibration errors. Since the signal is higher than expected it cannot be due to cloud or a star in the reference beam.

From the observed thermal flux, an estimate of the mass of dust in the beam, and the mass loss rate can be made (Ney, 1982). If the observed thermal flux were due to a dust coma, the mass in the 6 arcsec beam on December 21 was 3.5×10^5 kg, corresponding to a mass loss rate \dot{M} , of 120 kgs^{-1} . This corresponds to 250 kgs^{-1} at 1 A.U. (assuming $\dot{M} \propto r^{-2}$, Ney 1982) which apparently places Arend-Rigaux among the more active comets. However this mass loss rate is a considerable overestimate, since emission from the nucleus itself produces a considerable proportion of the observed infrared flux.

If 65% of the thermal infrared flux observed in the 6 arcsec aperture is due to the nucleus it would have an effective radius of 3.7km which lies close to the value for minimum light (3.9km) derived by A'Hearn (1985). However, the fractional contribution from the nucleus to the thermal flux will not be identical to that for the reflected flux because of the different scattering properties of grains compared to a particulate surface. The true value is probably much closer to 100% (i.e. $R=4.6\text{km}$). Tokunaga and Hanner (1985) found no observable dust coma at $10\mu\text{m}$ on January 19 while A'Hearn (1985) found a considerable coma at wavelengths less than $5\mu\text{m}$ but only a tiny contribution at 10 and $20\mu\text{m}$. Fig.25a shows an asteroid standard model with $R=4.6\text{km}$ fitted to the thermal data after subtraction of the scattered component.

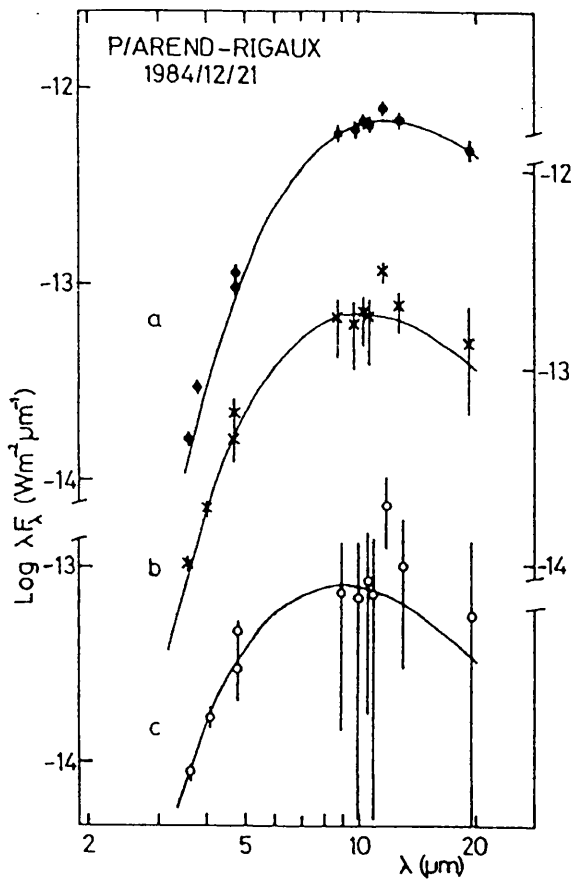


Fig.25 Infrared observations of P/Arend-Rigaux showing:

- (a) standard asteroid thermal model $T_0=340K$ (Morrison & Lebofsky, 1979), $R=4.6km$ fitted to total thermal emission. (b) 360K blackbody fitted to thermal emission after subtraction of 3.9km nucleus. (c) 410K blackbody fitted to thermal emission after subtraction of 4.3km nucleus. See text for explanation.

The standard model (Morrison & Lebofsky, 1979) with geometric albedo of 0.05, phase integral 0.6, emissivity 0.9, modelling constant 0.9 and infrared phase coefficient of 0.01 mag^{-1} , is not sensitive to errors in albedo for low values of the albedo. It appears that if there is any observed emission from the dust coma it must come from grains which are even hotter than 330K.

Figs. 25 b+c show blackbody fits to the data after subtraction of 3.9 and 4.3km nuclei. The best fits are for $(360 \pm 20)K$ and $(410 \pm 20)K$ respectively. These imply dust grain production rates of 23 or 6 kgs^{-1} . These values must be taken with caution however, since the temperatures imply extremely small grains which would have bluer colours than observed at JHK. The grain temperatures are determined essentially by the LL'M photometry which was made with a 7.8 arcsec aperture, corrected assuming a 60% contribution from the nucleus. Since the contribution for the thermal data is greater, then the derived grain temperatures would be even higher. The most likely explanation is that the observed cross-section of the nucleus changed during the ≈ 100 minute period between the UKT9 and UKT7 measurements. Tokunaga and Hanner (1985) noted a change of 35% in thermal flux over a period of 60mins.

The geometric albedo, P_{λ} , of the nucleus can be derived from the balance between thermal and reflected fluxes. For a solid nucleus the reflected flux is given by

$$F(\lambda) = \frac{S_0(\lambda) P_{\lambda} \left(\frac{R}{\Delta}\right)^2 10^{-0.4(ab)}}{r^2}$$

where S_0 is the solar flux at 1AU, r is the heliocentric distance in AU, R is the nucleus radius obtained from the thermal flux, α is the phase angle and β is the phase coefficient. A value of $\beta=0.035 \text{ mag degree}^{-1}$ for Arend-Rigaux at large heliocentric distances (Sekanina, 1976a) is typical of dark asteroids. Assuming 60% of the reflected flux in a 7.8 arcsec aperture is due to reflection from a nucleus, with R between 4.6 and 3.7km the albedo lies in the range

$P_J=0.06-0.10$, $p_H=0.08-0.13$, $p_K=0.08-0.12$. Tokunaga and Hanner (1985) derived values at the lower end of this range, and since they did not take into account the possibility of a contribution from the coma to the reflected flux, their values would in fact be upper limits. Bearing in mind the fact that the observed nuclear radius is probably closer to 4.6km than 3.7km, and probable light curve effects for the near infrared data, values of $P_J=0.06 \pm 0.03$, $p_H=0.08 \pm 0.03$, and $p_K=0.08 \pm 0.03$ have been adopted for the nuclear albedos. These values class the nucleus as a very dark object. The silicate feature now has to be considered in more detail. The typical silicate feature is expected at $\lambda \approx 9\mu\text{m}$ and is associated with silicon-oxygen vibrational modes. From laboratory tests on mineral compositions, two clear types of silicate emission features emerge. The first type (at the Restrahlen frequency) has its peak between 9-11 μm and shifts to longer wavelengths for decreasing SiO_2 content. Examples of objects whose spectra show this type are the asteroids Lutetia and Fortuna. The emission is attributed to a monolayer of particles in the 1-5 μm range. The second type (at the Christiansen frequency) has its peak between 7-9 μm and is associated with a densely packed layer of particles of 1-74 μm size range and is therefore optically thick. The lunar surface provides such a feature (Yamamoto, 1982). The silicate feature of Arend-Rigaux falls into the first type.

Infrared Colours

Both 3200 Phaethon and Neujmin 1 had stellar appearances on the television guider at UKIRT. For 3200 Phaethon, only sky background could be detected at a point 6 arcsec North.

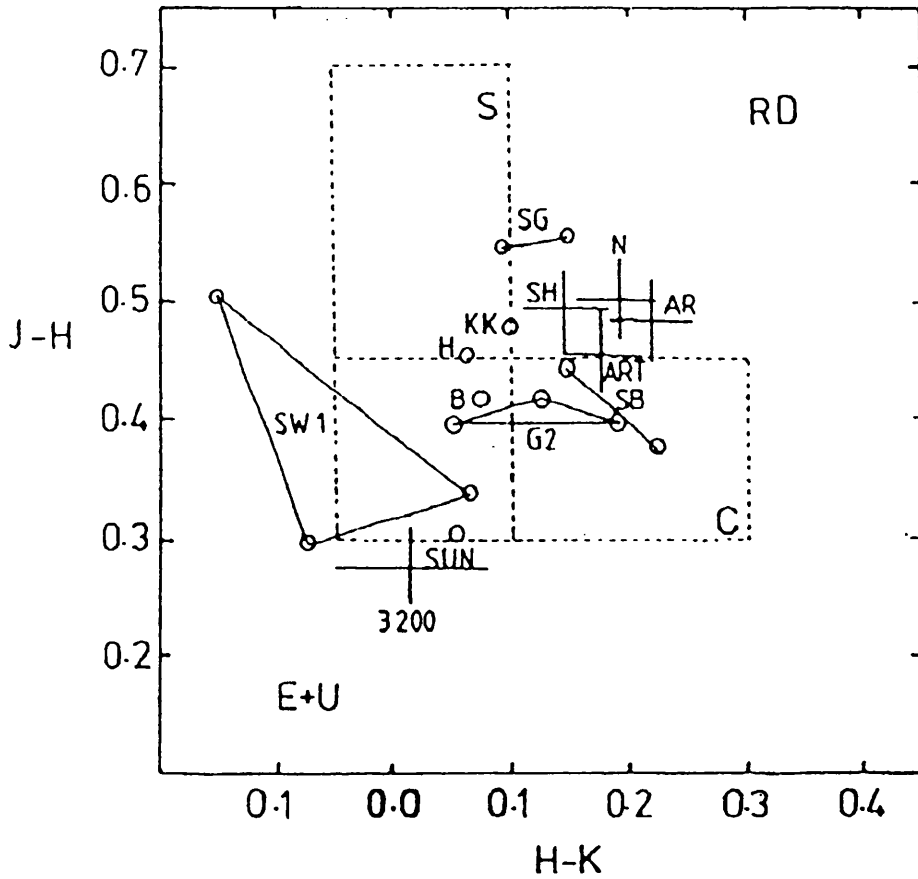


Fig.26 *J-H* versus *H-K* colours of Comets Arend-Rigaux, Neujmin 1, Shoemaker and the asteroid 3200 Phaethon (crosses) compared with colours of remote comets (Hartmann et al., 1982) and the S, C, E, U and RD asteroid domains.

SW-1: Schwassmann-Wachmann 1. G2: Gehrels 2.

S-G: Swift-Gehrels. H: Howell. B: Bowell.

SB: Slaughter-Burnham. KK: Kearns-Kwee.

AR: Arend-Rigaux. AR(T): Arend-Rigaux Tail.

It therefore

appeared that 3200 had no appreciable extension. Offsets (5 arcsec North-2 arcsec West), for Arend-Rigaux, were used with the J, H and K filters to determine the tail colours. J filter photometry, at the same offset position, was also undertaken for standard star GL347A. For GL347A the offset position was receiving $\approx 7\%$ of the central flux. This contamination made calculation of the exact amount of flux in the tail difficult. However tail colours could be calculated and infrared colours for all the comets are plotted in Fig.26.

The data for Arend-Rigaux has been averaged to one point. All three comets appear similar to a group of remote comets examined previously by Hartmann et al. (1982). However this region does not exclude comets which are non-remote and active. For example, J-H, H-K colours for Comet Halley, from April to December 1985 (Green et al., 1986) lie in this region also. It is interesting to note that P/Halley colours do not systematically change during the variations in heliocentric distances ($r > 1.42\text{AU}$) indicating that the scattering properties of the grain material are remaining constant. The resulting colours are close to those associated with C- and RD- type asteroids. RD-type material is common among the Trojan asteroids and it increases in incidence as we move from the asteroid belt to the outer solar system. This may indicate that the comets have surfaces and/or grain haloes containing low albedo carbonaceous material. There is a large colour difference between the comets and asteroid 3200 Phaethon. No significant difference between nuclear and tail colours exists for Arend-Rigaux.

5.3 Conclusions

The level of post-perihelion activity displayed by Arend-Rigaux was greater than expected for a transitional object. The dust tail axis is orientated away from the expected tail position and this suggests anisotropic emission. The contribution to the observed reflected light in a 7.8 arcsec beam, due to the nucleus is estimated at 59%. The contribution from the nucleus in a 6 arcsec aperture at thermal wavelengths appears to be closer to 100% since the observed spectrum is a good fit to an asteroid standard model and the dust grain temperatures would be rather high. The dust production rate is in the range of a few to 30kg s^{-1} . The observed effective nuclear radius is $(4.5 +0.2, -0.5)\text{km}$ and geometric albedo of 0.06 ± 0.03 at $1.25\mu\text{m}$. The red infrared colours indicate a somewhat lower optical albedo.

The infrared spectrum exhibited enhanced emission at $11.6\mu\text{m}$. An emission feature at $11\mu\text{m}$, attributed to a Si-O vibrational transition was observed for the C-type asteroid 19 Fortuna but at a much lower level than reported here (see Feirberg et al, 1983, Green et al., 1985b). No expected cometary species could produce the observed emission. Further observations are required to confirm the presence of this feature. P/Arend-Rigaux showed a prominent coma extension at visible wavelengths, but these same dust grains were inefficient at radiating at far infrared wavelengths. What type of grains would produce this effect? From the properties of grains we could say that the grains were extremely small (and therefore poor emitters) or that the grains were composed of pure silicate material which has a zero absorption coefficient. The latter would tie in with the

observed "silicate feature" but the expected temperatures would be very low for such a material.

Comet Neujmin 1 (also observed at post-perihelion) displayed some minor activity which could just be detected on the Schmidt plates and contributed 10% of the infrared flux in a 7.8 arcsec beam. All three comets studied (including Comet Shoemaker, which we may presume to be a fairly active comet) have colours similar to C or RD type asteroids suggesting dark, carbonaceous material. 3200 Phaethon had bluer colours and showed no cometary extension, in agreement with Cochran et al. (1985) who could not detect any cometary emissions during December 1984.

CHAPTER 6

CONCLUSIONS, SUGGESTIONS FOR FURTHER WORK,

APPENDICES AND REFERENCES.

6. Conclusions

Finson-Probstein analysis has been successfully applied to a range of P/Halley images. The results show, that the large dust-band structures, seen during February and March, were due to a series of outbursts, dating back to January, 1986. Most outbursts were of $2\pm 1/2$ days duration. A minority of outbursts were of ≈ 4 days duration. A 2.2day or 7.4day rotation/precession period, cannot be deduced from the UK Schmidt results.

P/Halley displayed an antitail and a sunward spike. The former consisted of large dust grains (up to $120\ \mu\text{m}$ in diameter, $\rho=1\text{gcm}^{-3}$) which had been emitted sometime prior to December 1985. The sunward spike could not be explained by Finson-Probstein theory and it was concluded that it was composed of grains which had high sunward ejection velocities and either grains of small radii ($<1\ \mu\text{m}$) and/or grains with very low densities ($<1\text{gcm}^{-3}$). In general the main tail was found to have grain diameters of submicron to micron sizes. The results show that large grains $>10\ \mu\text{m}$ assume eccentric orbits after ejection from the nucleus and thus contribute to the Zodiacal Cloud.

P/Crommelin, P/Arend-Rigaux and P/Giaccaobini-Zinner did not display such extended dust tails. Intensity plots of CCD and UK Schmidt images show that most image contours have a "swinging round" effect. For P/Arend-Rigaux this effect has been compared with the process of a nuclear "hot spot" situated on a rapidly rotating nucleus. Inner coma images of

P/Halley also show this effect, with the original "hot spot" area being at the precise subsolar point. However for Halley (and most probably for Crommelin and Giacobini-Zinner), a slow rotation period and a large image scale, point to radiation pressure effects being responsible for the contour shapes. Astrometric or near-nuclear images of P/Halley indicate parabolic hoods which represent the orbits of dust grains. The asymmetrical nature of these parabolas indicates a rotation period of at least a few days.

The method of using intensity profiles to prove the continuity of dust grain motion has proved unsuccessful. Images which show light scattered by dust grains and those which transmit radiation from gaseous species, have similar gradients and follow a $I \propto R^{-1}$ law. The method however can be used to show the change in physical nature of the comet.

The application of Mie theory to infrared spectra has shown that Halley's cometary grains, (of average temperature $T=290K$, $r=1.47AU$) could be composed of a composite material consisting of magnetite and olivine, representing absorbing and dielectric materials respectively. The average grain temperature was 60K higher than the expected black-body temperature at the same heliocentric distance, indicating once again the presence of small absorbing grains. Mass loss rates (between 2000 and 5000kgs⁻¹ for P/Halley) were in the range found by Green et al., (1986).

Optical and infrared observations of P/Neujmin 1 indicate that it could well be a transitional object between a decaying comet and an Earth crossing asteroid. Both P/Arend-Rigaux and P/Neujmin 1 possess an optically thin dust coma. Infrared observations therefore, revealed the thermal properties of the

nucleus and not the dust coma. The nucleus of P/Arend-Rigaux was found to be of radius $4.5 \pm_{0.5}^{0.2}$ km with a geometric albedo of 0.06 ± 0.03 at $1.25 \mu\text{m}$. Its infrared colours were close to RD- or C-type asteroids. Optical observations revealed an extended dust coma with anisotropic emission, clearly indicating that it could not be a transitional object. However P/Arend-Rigaux's dust grains must be small, to contribute to optical wavelengths whilst inefficiently emitting in the infrared. A pure silicate material could satisfy these conditions, although it could not produce such high thermal temperatures.

In summary, the physical nature of comets is very diverse. The short-period comets were considered unspectacular and Finson-Probstein theory could not be applied efficiently to such small dust tails. It is clear that grains with $F_{\text{rad}} < F_{\text{grav}}$ and $F_{\text{rad}} > F_{\text{grav}}$ exist in the dust tail of P/Halley, indicating a range of grain types, e.g. both magnetite and silicates. This conclusion agrees with Mie theory results when considering the chemical properties of the grains.

There is evidence to suggest that comets are related to other solar system phenomena e.g. P/Neujmin 1 with the Earth crossing asteroids and e.g. P/Halley, whose large grains contribute both to its associated meteor streams and to the Zodiacal Cloud.

Future Research

1. This thesis has only dealt with a small part of the complete Finson and Probst theory. Calculation of dust grain orbits, after ejection from a nucleus has led to the application of synchroes and syndynes to several cometary dust tails. The process could be taken a major step further to calculate the dust density distribution. Two methods can be used: 1) obtain the density for a tail composed of one particle size and then integrate over all particle sizes or 2) obtain the density distribution for a tail consisting of grains emitted at one time and then integrate over all emission times. Either procedure involves an assumed velocity distribution and emission rate N , to determine the number density along the line of sight from the Earth. Because the optical thickness of a dust tail is small, the number density (or surface density) is proportional to the observed light intensity. By varying the parameter N , theoretical densities maybe matched with observed intensities and so the true value of dust emission rate determined. For Comet Halley such a procedure would have to be done for each of the synchrone bands. The results could then be integrated to find the total mass production rate.

2. In Chapter 2, it has been stated that the dust grains in P/Halley's tail exist on both $F_{g_{rav}} > F_{rad}$ (elliptical and hyperbolic) and $F_{rad} > F_{g_{rav}}$ orbits. The latter type will be ejected onto convex hyperbolic orbits. The current computer programs, for some reason, will not calculate this type of orbit and so determine the true range of dust grain sizes. It may be, that further thought is required as to the mathematical nature of these convex orbits.

3. Many astrometric images were taken during 1986 to accurately determine the position of Halley for the Giotto probe. These images have been briefly discussed in Chapter 3. Sekanina and Larson (1984) have developed the concept of continuous ejection of dust from discrete emission sources on the rotating nucleus, to explain the evolution of spiral jets that unwind from the nucleus condensation into envelopes or halos. The boundaries of such envelopes, seen on these inner coma images, will be directly related to grain sizes, velocity distributions, the nuclear spin period and spin axis and the latitude and longitude of the emitting region together with the time of emission. By studying the changing shape of these parabolic hoods during several months, one may determine the precession period. Once this value is known (or assumed) a time variable function could be used in conjunction with Sekanina's and Larson's model to determine how the dust grain orbits vary, both with respect to the orbital period and the precession period.

4. Chapter 4 discusses Mie theory and its applications to infrared spectra. The type of grain material studied is severely restricted by the availability of physical constants supplied by laboratory results. In view of the Giotto dust experiments, which are still being analysed, there is a great need for more physical data on a whole range of suspected cometary dust constituents.

APPENDIX I

Properties of Orbits

The orbit of one body about another is classified by the value of the eccentricity e , so

for $0 < e < 1$ the orbit is an ellipse,

for $e = 1$ the orbit is a parabola

for $e > 1$ the orbit is a hyperbola

In the motion of one body around another, the energy conservation equation is,

$$C = \frac{1}{2} V^2 - \frac{\mu'}{r}$$

where $\mu' = G(m_1 + m_2)$. If V_1 and V_2 are the velocities of the masses m_1 and m_2 with respect to the centre of mass, taken to be at rest, the total energy of the system is given by,

$$E = \frac{1}{2} m_1 v_1^2 + \frac{1}{2} m_2 v_2^2 - \frac{Gm_1 m_2}{r}$$

where the sum of the first two terms is the kinetic energy while $-Gm_1 m_2 / r$ is the potential energy of the system. The

above equation may also be written,

$$E = \left(\frac{m_1 m_2}{m_1 + m_2} \right) \left(\frac{1}{2} V^2 - \frac{\mu'}{r} \right) = \left(\frac{m_1 m_2}{m_1 + m_2} \right) C$$

For a body orbiting the Sun $m_1 \ll m_2$ so that,

$$E = m_1 \left(\frac{1}{2} V^2 - \frac{\mu''}{r} \right) = m_1 C$$

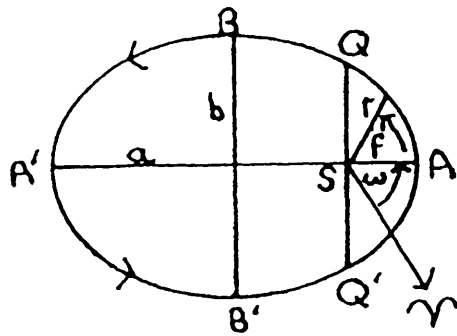
where $\mu'' = Gm_2$. The resulting orbit of the body can be classified according to the energy C , the velocity V being the deciding factor.

For an ellipse $V^2 = \mu''[(2/r) - (1/a)]$ hence $C = -\mu''/2a$.

For a parabola $V^2 = 2\mu''/r$ hence $C = 0$.

For a hyperbola $V^2 = \mu''[(2/r) + (1/a)]$ hence $C = \mu''/2a$

The elliptical orbit (taken from Roy, 1982)



Consider a body of mass m_1 orbiting the Sun of mass m_2 (clearly $m_1 < m_2$) such that the orbital and ecliptic plane coincide,

a = semimajor axis

b = semiminor axis

p = semilatus rectum = $a(1-e^2)$

$$p = \frac{h^2}{\mu''}$$

A = point of closest approach to the Sun (perihelion)

$$r = \frac{a(1-e^2)}{1 + e \cos f}$$

This is the polar equation of an ellipse.

T = orbital period \bar{n} = mean angular velocity

$$T = \frac{2\pi}{\bar{n}}$$

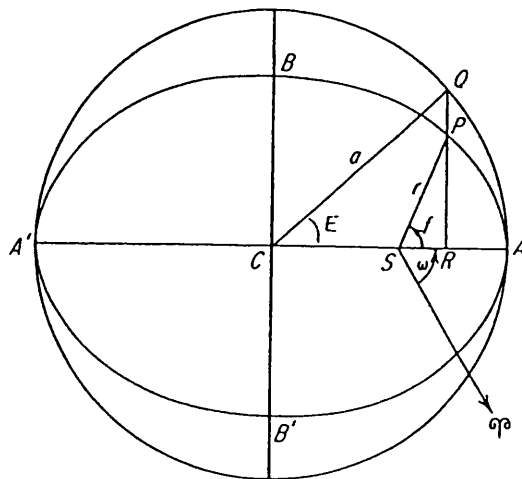
$$T = 2\pi(a^3/G(m_1 + m_2))^{1/2}$$

$h^2 = \mu'' a(1-e^2)$ where h is the angular momentum

$$\mu'' = G(m_1 + m_2)$$

$$f = \frac{h}{r^2}$$

The mean, eccentric and true anomalies



The radius vector turns through 2π radians in the orbital period T , so the mean angular velocity \bar{n} is given by,

$$\bar{n} = \frac{2\pi}{T}$$

If τ is the time of perihelion passage, the angle swept by a radius vector rotating about S with "mean" angular velocity \bar{n} in the time interval $(t-\tau)$ will be M , where

$$M = \bar{n}(t-\tau)$$

The mean anomaly M is defined in this way. If a circle is described on AA' as diameter, and the line through P on the ellipse, perpendicular to the major axis AA' , is produced to meet the circle in Q , the angle QCA , usually denoted by E and termed the eccentric anomaly is related to the true anomaly f ,

$$\text{by } r \cos f = a(\cos E - e) \text{ or}$$

$$r \sin f = a(1-e^2)^{1/2} \sin E \text{ or}$$

$$r = a(1 - e \cos E)$$

If the body of mass m_1 has its orbital plane in the ecliptic plane as in the diagram above then the true anomaly f is given by $f = (\theta - w)$.

From these equations the final expression becomes,

$$\tan\left(\frac{f}{2}\right) = \left(\frac{1+e}{1-e}\right)^{1/2} \tan\left(\frac{E}{2}\right)$$

E and M are related by Kepler's equation which is defined as

$$E - e \sin E = M = \bar{n}(t - \tau)$$

In the determination of orbits for Finson and Probst analysis M is usually given, e is known and the value of E is required. The procedure is to obtain an approximate value of E say E_0 , which nearly satisfies the equation e.g. $E_0 = M$. The true value of E is given by $E = E_0 + \Delta E_0$ so,

$$(E_0 + \Delta E_0) - e \sin(E_0 + \Delta E_0) = M$$

Expanding and neglecting any terms but zero and first order,

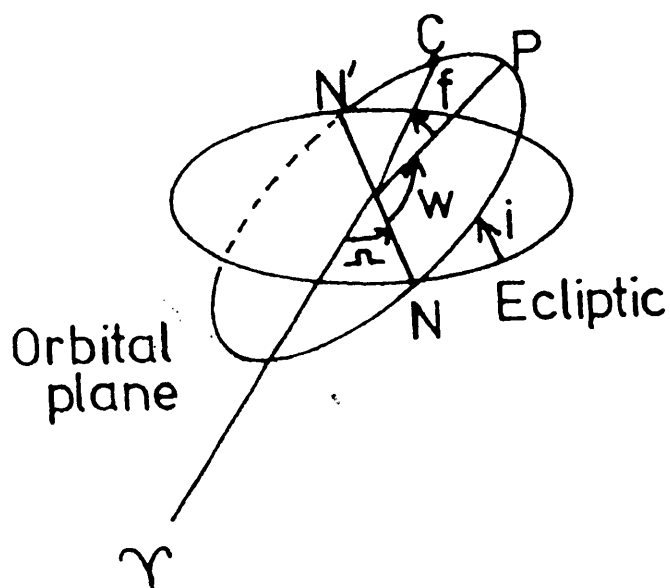
$$E_0 - e \sin E_0 + \Delta E_0 (1 - e \cos E_0) = M$$

or

$$\Delta E_0 = \frac{M - (E_0 - e \sin E_0)}{1 - e \cos E_0}$$

from which E_0 can be calculated. Then E_1 where $E_1 = E_0 + \Delta E_0$ is a more accurate value of E and the process can be repeated as often as is necessary (or until ΔE_0 becomes sufficiently small).

The Orbit In Space



Orbital parameters

e = eccentricity

a = semimajor axis

i = inclination of orbital plane to the ecliptic

Ω = longitude of the ascending node

w = argument of perihelion

T = perihelion date

f = F = true anomaly

Epoch = date for which the orbital elements are calculated

N = ascending node of the orbit

P = perihelion position

γ = vernal equinox reference direction

The Parabolic Orbit

$$r = \frac{p}{(1 + \cos f)}$$

$$p = 2q$$

$$h = 2\mu^* q$$

$$D = \tan\left(\frac{f}{2}\right)$$

$$\mu^* = \bar{n}^2 p^3$$

$$D + \frac{1}{3}D^3 = 2n(t - \tau)$$

The Hyperbolic Orbit

$$r = \frac{a(e^2 - 1)}{1 + e \cos \theta}$$

$$p = a(e^2 - 1)$$

$$h^2 = \mu^* a(e^2 - 1)$$

M = esinhF - F where F is analogous to E

$$M = n(t - \tau)$$

$$\tan\left(\frac{f}{2}\right) = \left(\frac{e+1}{e-1}\right)^{1/2} \tanh\left(\frac{E}{2}\right)$$

$$r = a(\operatorname{ecosh}E - 1)$$

APPENDIX II

Dust Particle Orbits

Dust particles released from a comet in an elliptical orbit may either move into elliptical orbits or hyperbolic orbits.

Ellipse - Ellipse case

Subscript c refers to the comet, subscript d to the emitted dust particle, and $\mu = F_{rad}/F_{grav}$. "e" denotes eccentricity, "a" the semimajor axis.

$$r_c = \frac{a_c (1 - e_c^2)}{(1 + e_c \cos f_c)} \quad r_d = \frac{a_d (1 - e_d^2)}{(1 + e_d \cos(f_d - \alpha_d))} \quad (1)$$

where f_d is the particle's true anomaly with reference to the comet's orbit and α_d is the particle's true anomaly with reference to its own orbit. The particle reaches its own perihelion at time t_{0d} .

At the point of release $r_c = r_d$ and $f_c = f_d$ (2) and the relative velocity is zero, so, using

$$\frac{dr}{dt} = \frac{dr}{df} \times \frac{df}{dt} \text{ and } \frac{df}{dt} = \frac{h}{r^2} \text{ (App. I) we have,}$$

$$\frac{dr_c}{dt} = \left(\frac{GM}{a_c (1 - e_c^2)} \right)^{1/2} e_c \sin f_c \quad \frac{dr_d}{dt} = \left(\frac{\mu GM}{a_d (1 - e_d^2)} \right)^{1/2} e_d \sin(f - \alpha) \quad (3)$$

$$\frac{df_c}{dt} = \frac{(GM a_c (1 - e_c^2))^{1/2}}{r_c^2} \quad \frac{df_d}{dt} = \frac{(\mu GM a_d (1 - e_d^2))^{1/2}}{r_d^2} \quad (4)$$

$$\text{from (4) and (2) } a_c (1 - e_c^2) = \mu a_d (1 - e_d^2) \quad (5)$$

$$\text{from (3) and (2) } \frac{e_c \sin f}{(a_c (1 - e_c^2))^{1/2}} = \frac{\mu^{1/2} e_d \sin(f - \alpha)}{(a_d (1 - e_d^2))^{1/2}}$$

$$\text{but } \frac{(a_d (1 - e_d^2))^{1/2}}{(a_c (1 - e_c^2))^{1/2}} = \frac{1}{\mu^{1/2}}$$

therefore,

$$\sin(f-\alpha) = \frac{e_c \sin f}{\mu e_d} \quad \text{and} \quad \alpha = f - \sin^{-1} \left(\frac{e_c \sin f}{\mu e_d} \right) \quad (6)$$

$$\text{From (1)} \quad r_c = \frac{a_d (1-e_d^2)}{(1 + e_d \cos(f-\alpha))} \quad r_c = \frac{a_c (1-e_c^2)}{\mu(1 + e_d \cos(f-\alpha))}$$

Therefore

$$e_d \cos(f-\alpha) = \frac{a_c (1-e_c^2)}{\mu r_c} - 1$$

and so

$$e_d^2 (1 - \sin^2(f-\alpha)) = \left(\frac{a_c (1-e_c^2)}{\mu r_c} - 1 \right)^2$$

and from (6)

$$e_d^2 \left(1 - \frac{e_c^2 \sin^2 f}{\mu^2 e_d^2} \right) = \left(\frac{a_c (1-e_c^2)}{\mu r_c} - 1 \right)^2$$

$$e_d^2 = \left(\frac{a_c (1-e_c^2)}{\mu r_c} - 1 \right)^2 + \frac{e_c^2 \sin^2 f}{\mu^2}$$

From (1) and using $\cos^2 f = 1 - \sin^2 f$ the last equation can be rearranged to give,

$$e_d^2 = 1 + \frac{2a_c (1-e_c^2)(1-\mu)}{\mu^2 r_c} - \frac{(1-e_c^2)}{\mu^2} \quad (7)$$

(7) into (5) gives

$$a_c (1-e_c^2) = \mu a_d \left(1 - \frac{2a_c (1-e_c^2)(1-\mu)}{\mu^2 r_c} + \frac{(1-e_c^2)}{\mu^2} - 1 \right)$$

or

$$a_d = \frac{-\mu r_c}{(2(1-\mu) - r_c/a_c)}$$

From App. I $\tan\left(\frac{f}{2}\right) = \left(\frac{1+e}{1-e}\right)^{1/2} \tan\left(\frac{E}{2}\right)$ (8)

or, $E - e \sin E = n(t_d - \tau)$ (9)

rearranging (8)

$$E(t_c - \tau) = 2 \tan^{-1} \left[\left(\frac{1-e_d}{1+e_d} \right)^{1/2} \tan \left(\frac{f_c(t_c - \tau) - \alpha_d}{2} \right) \right]$$

substituting for n and expanding (9)

$$t_o_d = (t_c - \tau) - \left(\frac{-a_d^3}{\mu GM} \right)^{1/2} \left[E(t_c - \tau) - e_d \sin E(t_c - \tau) \right]$$

Ellipse- Hyperbola

$$r_c = \frac{a_c (1 - e_c^2)}{1 + e_c \cos f_c} \quad r_d = \frac{(e_d^2 - 1)}{1 + e_d \cos(f_d - \alpha)}$$

Using the same release conditions and procedure as above,

$$\alpha = f_d - \sin^{-1} \left(\frac{e_c \sin f_c}{\mu e_d} \right)$$

$$e_d^2 = 1 + \frac{2a_c (1 - e_c^2) (1 - \mu) - (1 - e_c^2)}{\mu^2 r_c} - \frac{(1 - e_c^2)}{\mu^2}$$

$$a_d = \frac{\mu r_c}{(2(1 - \mu) - r_c/a_c)}$$

$$t_{o_d} = (t_c - \tau) - \left(\frac{a_d^3}{\mu GM} \right)^{1/2} [e_d \sinh F - F]$$

(Proofs maybe found in any book on conic sections)

Transformation to Sky Plane Co-ordinates

If $L = 0$ then $L_o = 0$

So $\frac{\xi_e \xi_T}{\Delta} = \frac{-\eta_e \eta_T}{\Delta}$ and $\xi_e \xi_T = -\eta_e \eta_T \dots 1)$

So,

$$M_o = \frac{1}{\Delta} \left\{ (\eta_e^2 + \zeta_e^2)^{1/2} \xi_T - \frac{\xi_e \eta_e \eta_T}{(\eta_e^2 + \zeta_e^2)^{1/2}} \right\}$$

and $\frac{1}{\Delta} = \frac{\Delta}{\Delta^2 - \xi_e \xi_T - \eta_e \eta_T}$ by 1) above

$$\text{therefore } M_T = \frac{\Delta}{(\Delta^2 - \xi_e \xi_T - \eta_e \eta_T)} \left\{ (\eta_e^2 + \zeta_e^2)^{1/2} \xi_T - \frac{\xi_T \eta_e \eta_T}{(\eta_e^2 + \zeta_e^2)^{1/2}} \right\}$$

(proven)

again, $N_o = \frac{\zeta_e \eta_T}{(\eta_e^2 + \zeta_e^2)^{1/2}}$ hence, $N_T = \frac{\zeta_e \eta_T}{(\eta_e^2 + \zeta_e^2)^{1/2}} \cdot \frac{\Delta^2}{(\Delta^2 - \xi_e \xi_T - \eta_e \eta_T)}$

(proven)

Appendix III

Mass loss rates (taken from Ney, 1982)

$(\lambda F_{\lambda})_{\max}$ is measured in a diaphragm of radius δ and is determined by the mass, M of the grains within this observed geometry. The infrared luminosity is

$$L_{IR} = 4\pi\Delta^2 [1.35(\lambda F_{\lambda})_{\max}] = 4\pi Na^2 Q_a \sigma T^4$$

where Δ = Earth-comet distance

N = total number of grains of radius a

Q_a = scattering emission efficiency

$Q_a = 0.3a$ for a silicate material (a in μm)

T = grain temperature

M = grain mass = $4/3N\pi\rho a^3$

ρ = grain bulk density

giving,

$$M = 1.7 \times 10^{35} \frac{(\lambda F_{\lambda})_{\max} \Delta^2}{T^4}$$

Δ = Earth-Comet distance, $(\lambda F_{\lambda})_{\max}$ is in Wcm^{-2} , M is in grams. The expression is independent of particle size. The mass is then divided by the grain residence time i.e. the time taken for a grain to travel across the coma radius, represented by the diaphragm δ . This time is found from the grain ejection velocity where,

$$v_{\text{ejection}} = 0.5(T_{\text{BB}}/300)^{1/2} \text{ kms}^{-1},$$

where T_{BB} is the blackbody temperature at the comet-Sun distance (Finson and Probst, 1968).

Dust Albedo (Hanner et al. 1981, Divine et al. 1986)

The albedo A , of the dust grains maybe expressed as

$$A = \frac{Q_{\text{sca}}}{Q_{\text{ext}}} \quad \text{or} \quad \frac{Q_{\text{sca}}}{Q_{\text{abs}}} \quad \text{or} \quad A = \frac{(\lambda F_{\lambda \max})_{\text{VIS}}}{(\lambda F_{\lambda \max})_{\text{IR}}}$$

and includes scattering radiation from reflection, refraction

and diffraction (the latter being important for rough or irregular particles). This albedo is sometimes referred to as the mean Bond Albedo, although the definition of a true Bond Albedo does not involve diffraction and is therefore not applicable for cometary dust.

A Geometric Albedo A_p is defined as,

$$A_p = \frac{\text{Energy scattered by a particle at } 180^\circ}{\text{Energy scattered by a white Lambert Disk}}$$

180° represents full phase or backward scattering and the Lambert Disk is taken to have the same geometric cross-section G as the grain or

$$A_p = \frac{I_o \sigma(180^\circ)}{I_o G/\pi} = \frac{\pi}{G} \sigma(180^\circ) = p = \pi A Q_{ext} \sigma(180^\circ) \dots (1)$$

(where G/π is equivalent to $\sigma(180^\circ)$ from Lambert's Law)

or as observations do not often occur at 180° phase angle, we redefine the geometric albedo as,

$$A_p(\theta) = \frac{\pi \sigma(\theta)}{G} = \pi A Q_{ext} \sigma(\theta) = p \left(\frac{I_s}{I_\pi} \right) \dots (2)$$

Note

1. $A_p = p$ for $\theta = 180^\circ$.
2. The relation between albedo and geometric albedo can be found from equation 2.

References

- A'Hearn, M.F., 1985. In "Asteroids, Comets and Meteors", Proc. Uppsala University Conf., June 1985, 187.
- A'Hearn, M.F., Campins, H., McFadden, L. + Millis, R., 1984. Bull.Am.Astr.Soc., 16, 1027.
- Bailey, M.E., Clube, S.V.M. + Napier, W.M., 1985. Vistas In Astronomy, 29, 53.
- Barbieri, C., Iijima, T. + Sabbadin, F., 1985. IAUC No.4138.
- Barker, E., 1984. IAU Circular. No. C3997.
- Baum, W.A. + Kreidl, T.J., 1985. In "Comets, Asteroids and Meteors II", Proc. Astronomical Observatory of Uppsala. 397.
- Belton, M., Spinrad, H., Wehinger, P. + Wyckoff, S., 1985. IAU Circular. No. C4029.
- Berg, O.E. + Grun, E., 1973. Space Res., 13, 1047.
- Bertele, T., 1986. IAUC No. 4189.
- Birkett, C.M., Green, S.F., Longmore, A. + Zarnecki, Z., 1985. IAUC No.4025.
- Brandt, J.C. + Chapman, R.D., 1982. In "Introduction to Comets" (Cambridge University Press), 93.
- Brooke, T.Y., Geballe, T.R., Knacke, R., Noll, K.S. + Tokunaga, A.T., 1985. IAUC No.4151.
- Brooke, T.Y. + Knacke, R.F., 1986. Icarus, 67, 80.
- Burns, J.A., Lamy, P.L. + Soter, S., 1979. Icarus, 40, 1.
- Campins, H., Gradie, J., Lebofsky, M. and Rieke, G. 1981. In "Modern Observational Techniques for Comets" (Pasadena: Jet Propulsion Lab.), 83.
- Campins, H. + Hanner, M.S., 1982. In "Comets", ed. L.L.Wilkening, (University of Arizona, Press.), 341.
- Cavagna, M., 1985. IAUC No.1985.
- Cochran, W.D., Cochran, A.L. + Barker, E.S., 1985. In

"Asteroids, Comets and Meteors", Proc. Uppsala University Conf., June 1985, 181.

Cochran, A.L. + Barker, E., 1985. IAUC No.4099.

Cosmovici, C.B., Mack, P., Craubner, H. + Schwarz, G., 1986. 20th ESLAB Symposium on "The Exploration of Halley's Comet" ESA SP-250, 2, 151.

Davies, J.K., Green, S.F., Stewart, B.C., Meadows, A.J. + Aumann, H.H., 1984. Nature, 309, 315.

Degewij, J. + Tedesco, E.F., 1982. In "Comets" ed. L.L.Wilkening, (University of Arizona, Press), 665.

Delsemme, A.H. + Swings, P., 1952. Ann.Astrophys. 15, 1.

Delsemme, A.H., 1976. In "Interplanetary Dust and the Zodiacal Light" eds. H.Elsasser + H.Fechtig (Berlin:Springer-Verlag), 481.

Dermott, S.F., Nicholson, P.D., Burns, J.A. + Houck, J.R., 1984. Nature, 312, 505.

Divine, N., Fechtig, H., Gombosi, T.I., Hanner, M.S., Keller, H.U., Larson, S.M., Mendis, D.A., Newburn, R.L., Heinhard, R., Sekanina, Z. + Yeomans, D.K., 1986. Space.Sci.Rev., 43, 1.

Djorgovski, S., Spinrad, H., Will, G. + Belton, M.J.S., 1984. IAUC No.3937.

Dohnanyi, J.S., 1976. In "Lecture Notes in Physics" eds. H.Elsasser + H.Fechtig (Berlin:Springer Verlag), 48, 187.

Drechsel, H. 1985. Preliminary result, IHW mailing network, No.2319.

Eaton, N., 1984. Vistas Astr., 27, 111.

Eaton, N., Davies, J.K. + Green, S.F., 1984. Mon.Not.R.Astr.Soc., 211, 15P.

Eaton, N. + Zarnecki, J.C., 1985. Mon.Not.R.Astr.Soc., 217, 659.

Emerson, G., 1985. IAUC No.4156.

Everhart, E. 1972. Astrophys. Lett. 10, 131.

Fairberg, M.A., Witterborn, F.C. + Lebofsky, L.A., 1983. Icarus, 56, 393.

Feldman, P.D., Weaver, H.A., Woods, T.N., A'Hearn, M.F., McFadden, L.A. + Festou, M.C., 1986. Bull. Amer.Ast.Soc., 18, 795.

Festou, M., 1984. IHW Newsletter, No.3, 4.

Festou, M., 1985a. Preliminary result IHW mailing network, No.2523.

Festou, M., 1985b. Preliminary result IHW mailing network, No2524.

Festou, M., Feldman, P.D., A'Hearn, M.F., Arpigny, C., Cosmovici, C.B., Danks, A.C., McFadden, L.A., Gilmozzi, R., Patriarchi, P., Tozzi, G.P., Wallis, M.K., Weaver, H.A., 1986. Nature, 321, 361.

Finson, M.L. + Probststein, R.F., 1968. Astrophys. J. 154, 327.

Flandern, van, T.C., 1978. Icarus, 36, 51.

Fraundorf, P., Brownlee, D.E. + Walker, R.M., 1982. In "Comets" ed. L.Wilkening (University of Arizona Press).

Gehrz, R.D. + Ney, E.P., 1986. 20th ESLAB Symposium on "The Exploration of Halley's Comet" ESA SP-250, 2, 101.

Gibson, J., 1984. IAU Circular. No. C3972.

Giese, R.H., Weiss, K., Zerull, R.H. + Ono, T., 1978. Astron.Astrophys., 65, 265.

Gilmore, A.C. + Kilmartin, P.M., 1984. IAU Circ. No. C3920.

Green, S.F., Meadows, A.J. + Davies, J.K., 1985a. Mon.Not.R.Astr.Soc., 214, 29P.

Green, S.F., Eaton, N., Aitken, D.K., Roche, P.F. + Meadows, A.J., 1985b. Icarus, 62, 282.

Green, S.F., McDonnell, J.A.M., Parkiewicz, G.S.A., Zarnecki, J.C., 1986. 20th ESLAB Symposium on "The Exploration of Halley's Comet" ESA SP-250, 2, 81.

Halley, E., 1704-5. In "Astronomiae Cometicae Synopsis" Phil.Trans.Roy.Soc., 24, 1882.

Hammel, H. + Cruikshank, D.P., 1985. IAUC No.4094.

Hanner, M.S., 1980. In "Solid Particles in the Solar System" eds. I.Halliday, + B.A.McIntosh, IAU Symp. 90. Reidel, Dordrecht, P223.

Hanner, M.S., 1981. Icarus. 47, 342.

Hanner, M.S., Giese, R.H., Weiss, K. + Zerull, R., 1981. Astron.Astrophys. 104, 42.

Hanner, M.S., 1983. Hungarian Acad. Sciences, 2, 1.

Hanner, M.S., 1984. Adv.Space Res., 4, 189.

Hanner, M.S., Tokunaga, A.T., Veeder, G.J. + A'Hearn, M.F., 1984. Astr. J., 89, 162.

Hanner, M.S., 1985. Adv.Space Res., 5, No.12, 325.

Hartmann, W.K. 1985. In "Asteroids, Comets and Meteors", Proc. Uppsala University Conf., June 1985, 191.

Hartmann, W.K., Cruikshank, D.P. + Degewij, J., 1982. Icarus, 52, 377.

Hayward, T.L., Gehrz, R.D. + Grasdalen, G.L., 1987. Nature, 326, 55.

Horanyi, M. + Mendis, D.A., 1985. Astrophys. J., 294, 355.

Huffman, D.R. + Stapp, J.L., 1973. In "Interstellar Dust and Related Topics", eds. J.M.Greenberg + H.C.van de Hulst, IAU Symp. 52, Reidel, Dordrecht, 297.

Hughes, D.W., 1982. In "Proc. Workshop on Interstellar Comets", Occ.Rep.R.Obs.Edinb., 9.

Hughes, D.W., 1984. J.Brit.Inter.Soc. 37, 3.

- Hulst, van de, H.C., 1957. In "Light Scattering by Small Particles", (John Wiley, New York).
- Itoh, T., 1985. IAUC No. 4155.
- Jacchia, L.G., Koppal, Z. + Millman, P.M., 1980. *Astroph.J.*, 111, 104.
- Jewitt, D.C. + Danielson, G.E., 1982. *IHW Newsletter*, No.2, 2.
- Jewitt, D. + Meech, K.J., 1985. *Icarus*, 64, 329.
- Jewitt, D., Meech, K. + Richer, G., 1985. IAUC No.4148.
- Jones, D.R.L., 1976. Thesis. "Formation and Motion of Cometary Tails".
- Julian, W.H., 1987. *Nature*, 326, 57.
- Kaminski, C. + Griep, D., 1985. IAUC No. 4154.
- Kaneda, E., Ashihara, O., Shimizu, M., Takagi, M. + Hirao, K., 1986. *Nature*, 321, 297.
- Keller, H.U., Arpigny, C., Barbieri, C., Bonnet, R.M., Cazes, S., Coradini, M., Cosmovici, C.B., Delamere, W.A., Huebner, W.F., Hughes, D.W., Jamar, C., Malaise, D., Reitsema, H.J., Schmidt, H.U., Schmidt, W.K.H., Seige, P., Whipple, F.L. + Wihelm, K., 1986. *Nature*, 321, 320.
- Kissel, J., Sagdeev, R.Z., Bertaux, J.L., Angarov, V.N., Audouze, J., Blamont, J.E., Buchler, K., Evlanov, E.N., Fechtig, H., Fomenkova, M.N., Hoerner, von H., Inogamov, N.A., Khromov, V.N., Knabe, W., Krueger, F.R., Langevin, Y., Leonas, V.B., Levasseur-Regourd, A.C., Managadze, G.G., Podkolzin, S.N., Shapiro, V.D., Tabaldyev, S.R. + Zubkov, B.V., 1986. *Nature*, 321, 280.
- Koutchmy, S. + Lecacheux, J., 1985. IAUC No.4115.
- Krankowsky, D., Lamerzahl, P, Herrwerth, I., Woweries, J., Eberhardt, P., Dolder, U., Herrmann, U., Schulte, W., Berthelier, J.J., Illiano, J.M., Hodges, R.R. + Hoffman, J.H.,

1986. *Nature*, 321, 326.

Kratschmer, W. + Huffman, D.R., 1979. *Astrophys. Space Sci.*, 61, 195.

Kratschmer, W., 1980. In "Solid Particles in the Solar System" Eds. I.Halliday, B.A.McIntosh, IAU Symp. 90, Reidel, Dordrecht.

Kresak, L., 1980a. *Moon. Plan.*, 22, 83.

Kresak, L., 1980b. In "Solid Particles in the Solar System" eds. I.Halliday + B.A.McIntosh (Dordrecht, Holland:D. Reidel Publ.. Co.), 211.

Labs, D. + Neckel, H., 1970. *Sol.Phys.*, 15, 79.

Landgraf, W., 1985. IAUC No.4115.

Larson, S., 1984. IAU Circular No. 3921.

Larson, S., 1985. IAUC No.4125.

Larson, S. + Levy, D., 1986. IAUC No. 4159.

Lecacheux, J., Fevre, le, O., Baudrand, J., Lemonnier, J.P. + Mathez, G., 1984a. IAUC No.3928.

Lecacheux, J., Fevre, le, O., Baudrand, J., Lemonnier, J.P. + Mathez, G., 1984b. IAUC No.3934.

Leibowitz, E.M. + Brosch, N., 1986. *Icarus*, 68, 418.

Lyttleton, R.A., 1953. In "The Comets and their Origin", Cambridge;Cambridge University Press.

Maas, R.W., Ney, E.P. + Woolf, N.F. 1970. *Astrophys.J.*, 160, L101.

Marsden, B.G., 1970. *Astron.J.* 75, 206.

Marsden, B.G., 1971. In "Physical Studies of Minor Planets", ed. T.Gehrels (Washington: NASA SP-267), 413.

Marsden, B.G., 1972. In "The Motion, Evolution of Orbits, and Origins of Comets" eds. G.A.Chebotarev, E.I.Kazimirchak-Polonskaya, and B.G.Marsden (Dordrecht,

Holland: D.Reidel), 135.

Meech, K.J. + Jewitt, D., 1986. *Icarus*, 66, 561.

Mendis, D.A., Houppis, H.L.F. + Marconi, M.L., 1985. *Fundam.Cosmic Phys.*, 12, Nos1-4, 1.

Millis, R.L. + Schleicher, D.G., 1986. *Nature*, 324, 646.

Morrison, D. + Lebofsky, L.A., 1979. In "Asteroids" ed. T.Gehrels, (University of Arizona Press), 184.

Mumma, M.J., Weaver, H.A., Larson, H.P. Davis, D.S. + Williams, M., 1985. IAUC No.4154.

McDonnell, J.A.M., Alexander, W.M., Burton, W.M., Bussoletti, E., Clark, D.H., Grard, R.J.L., Grun, E., Hanner, M.S., Hughes, D.W., Igenbergs, E., Kuczera, H., Lindblad, B.A., Mandeville, J.C., Minafra, A., Schwehm, G.H., .Sekanina, Z., Wallis, M.K., Zarnecki, J.C., Chakaveh, S.C., Evans, G.C., Evans, S.T., Firth, J.G., Littler, A.N., Massonne, L., Olearczyk, R.E., Pankiewicz, G.S., Stevenson, T.J. + Turner, R.F. 1986. *Nature*, 321, 338.

McCarthy, P.J., Strauss, M. + Spinrad, H., 1985. IAUC No.4104.

McFadden, L.A., A'Hearn, M.F., Feldman, P.D. + Butterworth, P., *Bull.Amer.Ast.Soc.*, 18, 795.

McNaught, R.H., 1984. IAU Circular. No. C4010.

Ney, E.P., 1974. *Astrophys.J.* 189, L141.

Ney, E.P., 1982. In "Comets" ed. L.LWilkening, (University of Arizona, Press), 323.

Ney, E.P. + Knutson, A.G., 1986. IAUC No. 4178.

Oort, J.H., 1950. *Bull.Astron.Inst.Neth.* 11, 91.

Ovenden, M.W., 1975. *Vistas in Astronomy*, 18, 473.

Oyama, K., Hirao, K., Hirano, T., Yumoto, K. + Saito, T., 1986. *Nature*, 321, 310.

Ozeki, T. 1986. IHW Newsletter No.8.

Price, S.D. Murdock, T.L. + Marcotte, L.P., 1980. *Astron.J.*, 85, 765.

Rees, D. + Wallis, M.K., 1985. IAUC No.4103.

Romanishin, W. + Sitko, M., 1984. IAU Circular No. 3927.

Roy, A.E., 1982. In "Orbital Motion" (Adam Hilger Ltd), 69.

Sagdeev, R.Z., Blamont, J., Galeev, A.A., Moroz, V.I., Shapiro, V.D., Shevchenko, V.I. + Szego, K. 1986. *Nature*. 321, 259.

Sandford, S.A., 1986. *Icarus*, 68, 377.

Schleicher, D.G., 1985. *Bull.Amer.Ast.Soc.* 17, 686.

Sekanina, Z., 1974. *Sky and Telescope*, 47, 374.

Sekanina, Z., 1976a. In "The Study of Comets" eds. B.Donn, H.Mumma, W.Jackson, M.A'Hearn, + R.Harrington, (NASA SP-393, Washington), 537.

Sekanina, Z., 1976b. In "Interplanetary Dust and the Zodiacal Light" eds. H.Elsasser + H.Fechtig (Berlin:Springer-Verlag), 434.

Sekanina, Z., 1979. In "Comet Halley Micrometeoroid Hazard" ESA SP-153, 25.

Sekanina, Z., 1981. *Astron. J.*, 86, 1741.

Sekanina, Z., 1985, *Astron.J.*, 90, 827.

Sekanina, Z., 1986a. IAUC No. 4187.

Sekanina, Z., 1986b. 20th ESLAB Symposium on "The Exploration of Halley's Comet" SP-250, 2, 177.

Sekanina, Z., 1986c. 20th ESLAB Symposium on "The Exploration of Halley's Comet" SP-250, 2, 131.

Sekanina, Z., 1987. *Nature*, 325, 326.

Sekanina, Z. + Schuster, H.E., 1978a. *Astron.Astrophys.*, 65, 29.

Sekanina, Z. + Schuster, H.E., 1978b. *Astron.Astrophys.*, 68,

429.

Sekanina, Z. + Farrell, J.A., 1980. *Astron. J.*, 85, 1538.

Sekanina, Z. + Larson, S.M., 1984. *Astron.J.*, 89, 1408.

Sekanina, Z. + Larson, S.M., 1986. *Astron.J.*, 92, 462.

Shoemaker, E.M., Williams, J.G., Helin, E.F. and Wolfe, R.F. 1979. In "Asteroids" ed. T.Gehrels (Tucson: Univ. of Arizona Press), 253.

Shoemaker, E. + Shoemaker, C., 1984. IAU Circular. No. C4004.

Smith, B.A., Larson, S.M., Szego, K. + Sagdeev, R.Z., 1987. *Nature*, 326, 573.

Smirnov, V., Vaisberg, O. + Anisimov, S., 1986. In the "Exploration of Halley's Comet" Proc. 20th ESLAB Symposium, ESA SP-250, 2, 195.

Spinrad, H., Wehinger, P., Wyckoff, S., 1984a. IAU Circular No. 3914.

Spinrad, H., Djorgovski, S. + Belton, M.J.S., 1984b. IAU Circular No.3996.

Storrs, A.D., Tokunaga, A.T., Christian, C.A. + Heasley, J.N., 1986. *Icarus*, 66, 143.

Sykes, M.K., Lebofsky, L.A., Hunter, D.M. + Low, F., 1986. *Science*, 232, 1115.

Telesco, C.M., Decher, R., Baugher, C., Campins, H., Mozurkewich, D., Thronson, H.A., Cruikshank, D.P., Hammel, H.B., Larson, S. + Sekanina, Z., 1986. *Astrophys.J.*, 310, L61.

Thomas, A.J., Hyland, A.R. + Robinson, G., 1973. *Mon.Not.R.Astron.Soc.*, 165, 201.

Tokunaga, A.T. + Hanner, M.S., 1985. *Astr. J.*, 296, L13.

Tokunaga, A.T., Golisch, W.F., Griep, D.M., Kaminski, C.D. + Hanner, M.S., 1986. *Astron.J.* 92, 1183.

Traub, W.A. + Steir, T.M., 1976. *Appl. Opt.*, 15, 373.

Vaisberg, O.L., Smirnov, V.N., Gorn, L.S., Iovlev, M.V.,
Balikchin, M.A., Klimov, S.I., Savin, S.P., Shapiro, V.D. +
Shevchenko, V.I. 1986. Nature. 321, 274.

Vsekhsvyatskii, S.K., 1964. In "The Physical Characteristics
of Comets" NASA TTF80 Israel Program for Scientific
Translations, Washington DC.

Vsekhsvyatskii, S.K., 1977. In "Comets, Asteroids and
Meteorites: Interrelations, Evolution and Origins" ed.
A.H.Delsemme, (Toledo:University of Toledo Press), 469.

Walker, R.G., Aumann, H.H., Davies, J.K., Green, S.F., de
Jong, T., Houck, J.R. + Soifer, B.T., 1984. Astrophys.J., 278,
L11.

Wallis, M. + Gilmozzi, R., 1985. IAUC No. 4149.

Wallis, M.K., Meredith, N., Rees, D., Williams, I.P., Andrews,
P.J. + Williams, G., 1987. In Preptn.

Wasson, J.T. + Wetherill, G.W., 1979. In "Asteroids" ed. T.
Gehrels (University of Arizona Press) 926.

Weg, van de, R.L.W., 1986. Zenit, 13, 358.

West, R.M., 1986. IAUC No.4196.

Whipple, F.L., 1950. Astrophys.J. 111, 375.

Whipple, F.L., 1955. Astrophys.J. 121, 750.

Whipple, F.L., 1980. IAUC No.3459.

Wickramasinghe, P. + Allen, D., 1986. IAUC No.4205.

Wilkening, L.L., 1979. In "Asteroids" ed. T.Gehrels
(University of Arizona Press), 61.

Williams, I.P., Andrews, P.J., Fitzsimmons, A. + Williams,
G.P., 1987. Mon.Not.R.Astr.Soc., 226, 1P.

Wisdom, J., 1985. Icarus, 66, 272.

Woerkom, van A.A.J., 1948. BullAstron.Inst.Neth. 10, 445.

Wood, J.A., 1979. In "The Solar System" ed. A.L.McAlester

(Prentice-Hall, Inc.) 29.

Wyckoff, S., 1982. In "Comets" ed. L.L.Wilkening, (University of Arizona, Press), 3.

Wyckoff, S. + Wehinger, P.A., 1985. IAUC No.4125.

Wyckoff, S., Wagner, M., Wehinger, P.A., Schleicher, D.G. + Festou, M.C., 1985. Nature, 316, 241.

Yamamoto, T., 1982. Astron. and Astrophy. 109, 326.

Zarnecki, J.C., Eaton, N., McDonnell, J.A.M., Meadows, A.J.,

Carey, W.C. + MacDonald, G.H., 1984. Adv.Space Res. 9, 205.

Zook, H.A. + Berg, O.E., 1975. Plan.Space Sci., 23, 183.

Optical and Infrared Observations of Cometary Dust

C.M.Birkett

Abstract

In 1968, Finson and Probst outlined a theory which could be used to analyse cometary dust tails. This theory is applied to a series of P/Halley images, obtained using the UK Schmidt Telescope. The theory is successful and shows that P/Halley underwent a series of major outbursts during early 1986. The duration of the outbursts is approximately 2 days. This value coincides with the 2.2day nuclear rotation period, estimated by other observers. The size of the dust grains varies from submicron to several hundred microns and their calculated orbital parameters indicate that a considerable fraction of the larger grains contribute to the Zodiacal Dust Cloud.

A range of CCD and UK Schmidt images reveal dust features in the comae of comets P/Crommelin, P/Giacobini-Zinner and P/Halley. Intensity contours for many images exhibited a "swinging round" effect i.e. for each image there was a systematic change in the photometric axis from the central condensation outwards. This was attributed to radiation pressure effects. Astrometric images of P/Halley show sharp parabolic hoods. These hoods are discussed with reference to near-nuclear dust grain orbits. Preliminary results indicate that the rotation period of Halley is at least a few days.

Mie (1908), developed a method by which the general properties of scattering and emission by dust grains, can be used to model cometary thermal spectra. Such a method is applied to several P/Halley spectra, taken during April, 1986. The results indicate that the dust grains could be composed of both an absorbing (e.g. magnetite) and a dielectric (e.g. silicate) material.

The interrelations between decaying comets and Earth-crossing asteroids are discussed. Optical and infrared observations indicate that comet P/Neujmin 1 may be a transitional object. P/Arend-Rigaux however, is still very active, displaying a large dust coma, with anisotropic emission.

Optical and Infrared Observations of Cometary Dust

C.M. Birkett

Abstract

In 1968, Finson and Probst outlined a theory which could be used to analyse cometary dust tails. This theory is applied to a series of P/Halley images, obtained using the UK Schmidt Telescope. The application of the theory is successful and shows that P/Halley underwent a series of major outbursts during early 1986. The duration of the outbursts is approximately 2 days. This value coincides with the 2.2 day nuclear rotation period, estimated by other observers. The size of the dust grains varies from submicron to several hundred microns and their calculated orbital parameters indicate that a considerable fraction of the larger grains contribute to the Zodiacal Dust Cloud.

A range of CCD and UK Schmidt images reveal dust features in the comae of comets P/Crommelin, P/Giacobini-Zinner and P/Halley. Intensity contours for many images exhibited a "swinging round" effect i.e. for each image there was a systematic change in the photometric axis from the central condensation outwards. This was attributed to radiation pressure effects. Astrometric images of P/Halley show sharp parabolic hoods. These hoods are discussed with reference to near-nuclear dust grain orbits. Preliminary results indicate that the rotation period of Halley is at least a few days.

Mie (1908), developed a method by which the general properties of scattering and emission by dust grains, can be used to model cometary thermal spectra. Such a method is applied to several P/Halley spectra, taken during April, 1986. The results indicate that the dust grains could be composed of both an absorbing (e.g. magnetite) and a dielectric (e.g. silicate) material.

The interrelations between decaying comets and Earth-crossing asteroids are discussed. Optical and infrared observations indicate that comet P/Neujmin 1 may be a transitional object. P/Arend-Rigaux however, is still very active, displaying a large dust coma, with anisotropic emission.